



**HAL**  
open science

## Development of high sensitivity gamma and beta sensors for in situ diffusion tests in the mudstone in France

Zhenhua Lin

► **To cite this version:**

Zhenhua Lin. Development of high sensitivity gamma and beta sensors for in situ diffusion tests in the mudstone in France. Theoretical and/or physical chemistry. Université de Lyon, 2017. English. NNT : 2017LYSE1024 . tel-01528825

**HAL Id: tel-01528825**

**<https://theses.hal.science/tel-01528825>**

Submitted on 29 May 2017

**HAL** is a multi-disciplinary open access archive for the deposit and dissemination of scientific research documents, whether they are published or not. The documents may come from teaching and research institutions in France or abroad, or from public or private research centers.

L'archive ouverte pluridisciplinaire **HAL**, est destinée au dépôt et à la diffusion de documents scientifiques de niveau recherche, publiés ou non, émanant des établissements d'enseignement et de recherche français ou étrangers, des laboratoires publics ou privés.



N°d'ordre NNT : 2017LYSE1024

## **THESE de DOCTORAT DE L'UNIVERSITE DE LYON**

opérée au sein de  
**l'Université Claude Bernard Lyon 1**

**Ecole Doctorale N° 206**  
**(Ecole Doctorale de Chimie de Lyon)**

**Spécialité de doctorat :**  
**Discipline : Physique Chimie**

Soutenue publiquement/à huis clos le 13/02/2017, par :

# **Zhenhua Lin**

---

## **Development of high sensitivity gamma and beta sensors for in situ diffusion tests in the mudstone in France**

---

Devant le jury composé de :

Pancze, gerard  
Hartnack, Christoph  
Sunghee, Jung  
BLANCHIN, Marie-Genevieve  
Vinsot, Agnès  
Blin, Virginie  
Tillement, Olivier  
Brisset, Patrick  
Hautefeuille, Benoit

Pr Université Lyon 1  
Pr Mines Nantes  
Dr KAERI, South Korea  
Pr Université lyon 1  
Dr ingénieur ANDRA  
Ingénieur de recherche CEA  
Pr Université lyon 1  
Dr Ingénieur de recherche AIEA  
Dr CEO AXINT

Président  
Rapporteur  
Rapporteur  
Examinatrice  
Examinatrice  
Examinatrice  
Directeur de thèse  
Examineur  
Examineur invité

## **Remerciements:**

Je remercie tout d'abord L'AXINT et tous ses responsables, à tous les niveaux, de m'avoir accueilli au sein de son équipe de recherche, en tant qu'un poste d'Ingénieur de Recherche.

Je tiens à remercier mon directeur et mon encadrant de la thèse, Monsieur Olivier Tillement et Benoît Hautefeuille (CEO AXINT), pour la confiance qu'il m'a accordée en acceptant d'encadrer ce travail doctorant entre ILM FENNEC laboratoire et la société AXINT. Au cours de cette thèse, je me suis sentie complètement intégrée à l'équipe AXINT. Merci à hautefeuille pour nos nombreuses discussions enrichissantes en physique des particules ionisantes, et m'a formé des compétences en électronique également avec Philippe Anfre au début. Merci à Guillaume Burato pour m'avoir tout appris en informatique et programmation système embarqué, pour son aide précieuse dans la compréhension du code source Labview et Microchip MPLABX.

Je merci tout particulièrement à Mattéo Martini, pour sa relecture méticuleuse et son efficacité surtout pour avoir corrigé le trop nombreux fautes d'anglais.

Et aussi particulièrement à Marie-Genevieve Blanchin et Benoit Hautefeuille, pour sa relecture et ses conseils toujours très pertinents tout au long de ma rédaction de la thèse.

Mes remerciements vont également à monsieur Patrick Brisset, madame Agnès Vinsot, Virginie Blin, Marie-Genevieve Blanchin pour avoir accepté de participer à ce jury de thèse. Je suis infiniment gré à monsieur Sung-Hee Jung et Christophe Hartnack de s'être rendu disponible pour la pré-soutenance, de m'avoir prodigué maints conseils et d'avoir accepté la fonction de rapporteur.

Merci également à mes parents qui, même de très loin, m'ont encouragée et soutenue de leur grand amour, pour l'accomplissement de ce mémoire.

J'aimerais adresser toute ma gratitude aux membres du laboratoire (FENENC) pour leur soutien et leur enthousiasme et surtout pour goûter toutes les nouvelles recettes de gâteaux.

**CHAPTER 1 THE ART OF TRACERS IN THE CONTEXT OF NUCLEAR WASTE MANAGEMENT 17**

**1.1 Global context.....17**

**1.2 Classification of radioactive waste in France.....18**

**1.3 ANDRA: Underground Research Laboratory (URL).....22**

**1.4 Art of tracers.....27**

1.4.1 Generalities .....27

1.4.2 Radiotracers .....29

1.4.3 The half-life and types of radiotracers .....29

1.4.4  $\gamma$ -rays interactions in the matter: .....32

1.4.5 The injections of radiotracers in the DRN experiments .....36

1.4.5.1 Mineralogy composition and structure of the COX clay: .....36

1.4.5.2 The diffusion properties of neutral, anionic and cationic radiotracers .....42

1.4.5.3 The mobility of radioactive substance and candidate tracer for non-mobility radionuclide ..45

**1.5 Conclusion.....50**

**CHAPTER 2 GENERAL METHODS, THEORY AND TECHNICAL ASPECTS ..... 51**

**2.1 Introduction:.....51**

**2.2 The technology behind sensors.....52**

2.2.1 Principles of the scintillator detection.....52

2.2.2 The criteria for the selection of scintillators.....54

2.2.3 Photon sensors .....56

2.2.3.1 Photomultiplier (PMT).....56

2.2.3.2 Photo diode.....57

2.2.3.3 Silicon PhotoMultiplier (SiPM) .....59

2.2.4 Electronic signal processing.....62

2.2.4.1 Preamplification .....62

2.2.4.2 Pulse shaping.....64

2.2.4.3 General view of AXINT analog electronic design .....66

2.2.5 Discrimination.....68

2.2.6 Analog to Digital Conversion (ADC) for multi-channel analyzer (MCA) .....71

2.2.7	Digital signal procession and communication protocols.....	75
	Microcontroller: dspic33EP512MC806.....	75
2.2.8	Friendly interpretation interface: Labview.....	80
<b>2.3</b>	<b>Statistics for data analysis.....</b>	<b>81</b>
<b>2.4</b>	<b>The radiotracers simulation tools .....</b>	<b>90</b>
2.4.1	How to simulate radiation phenomenon?.....	90
2.4.1.1	Introduction Monte Carlo (Monte Carlo N-Particle Transport Code).....	90
2.4.1.2	MCNP simulation process .....	91
2.4.1.3	Structure of the MCNP Input File .....	92
2.4.2	Development of CAD or CFD auto-conversion algorithm .....	99
2.4.2.1	Introduction.....	100
2.4.2.2	CAD auto conversion algorithm.....	106
2.4.2.3	CFD auto conversion algorithm.....	113
<b>CHAPTER 3: THE IN SITU TRACERS DIFFUSION STUDIES .....</b>		<b>117</b>
<b>3.1</b>	<b>Introduction .....</b>	<b>117</b>
<b>3.2</b>	<b>Calculation of dimensional design in DRN experience via CFD and MCNP simulations.....</b>	<b>118</b>
3.2.1	Introduction.....	118
3.2.1	CFD Simulations for geometry profile data and for parameter setting data.....	119
3.2.2	Introduction to CFD simulations in 2D and 3D .....	124
3.2.3	The MCNP simulation of gamma sensors response under different radiotracers distribution ...	128
3.2.4	Conclusion .....	135
<b>3.3</b>	<b>Validation of high sensitivity gamma and beta sensors for the tracers injection of <sup>22</sup>Na, <sup>241</sup>Am and <sup>36</sup>Cl.....</b>	<b>138</b>
3.3.1	In situ Beta detection sensor system .....	139
3.3.1.1	Beta sensors design and performance.....	139
3.3.1.2	Beta simulation studies.....	151
3.3.2	In situ Gamma detection sensor system .....	155
3.3.2.1	Gamma sensor design and performance.....	155
3.3.2.2	Gamma simulation studies:.....	168
3.3.3	Conclusion .....	175

GENERAL CONCLUSION.....	177
BIBLIOGRAPHY .....	178
ANNEX .....	185

## Lists of Abbreviations:

ANDRA: The French National Radioactive- Waste Management Agency	ADC: Analog to digital circuit
LLW-LL: Low-level long-lived waste	SPI: Serial Peripheral Interface
ILW-LL: Intermediate-level long-lived waste	CAN: Controller Area Network
HLW: high-level waste	MCNP: Monte Carlo N-Particle- Transport Code
CIGEO: Centre Industriel de Stockage Géologique	MCA: Multi-Channel analyser
URL: underground research laboratory	CSG: Constructive Solid Geometry
COX: Callovian-Oxfordian mudstone	UM: Unstructured Mesh
DRN: Diffusion of RadioNuclide	CFD: Computational fluid dynamics
L.D: limits of detection	CAD: Computer-aided design
HTO: Tritiated water	STL: Stereo lithography
BGO: Bismuth germinate $\text{Bi}_4\text{Ge}_3\text{O}_{12}$	FOSs: Fiber-optic sensors
NaI(Tl): Sodium Iodide doped Thallium	SNR: Signal to noise ratio
CsI(Tl): Cesium Iodide doped Thallium	CPS: Counts per second
YSO: Yttrium Orthosilicate	CPM: Counts per minute
PMT: Photomultiplier	LLD: Low level discrimination
SiPM: Silicon photomultipliers	MDA: Minimum detection activity
DSP: Digital Signal Processing	CEA: Commissariat à l'énergie atomique et aux énergies alternative
HV: High voltage	
SCA: Single channel analyzer	

## List of Figures:

Figure 1: General layout of CIGEO facilities.....	22
Figure 2: General view of the Meuse Haute Marne Underground research laboratory....	23
Figure 3 : Tracer methodology and interdisciplinary aspects.....	28
Figure 4: Dependences of photon mass attenuation coefficients ( $\text{cm}^2/\text{g}$ ) in BGO crystal on photon energy (XCOM, s.d.) .....	33
Figure 5: Energy histogram for $^{137}\text{Cs}$ .....	34
Figure 6: Compton scattering diagram .....	35
Figure 7: Composition of COX clay.....	37
Figure 8: Basic component of clay minerals.....	38
Figure 9: Structure of kaolinite.....	39
Figure 10: Structure of illite muscovite .....	40
Figure 11: Structure of illite smectite .....	41
Figure 12: Structure of chlorite.....	42
Figure 13: A surface complex formed between $\text{Na}^+$ and a charged surface site on montmorillonite.....	44
Figure 14: Inside view of surface charge and interlayer for clay mineral (COX) .....	45
Figure 15: Decay scheme for $^{22}\text{Na}$ .....	47
Figure 16: Decay schema for $^{36}\text{Cl}$ .....	47
Figure 17: General scheme of implementation of DRN test drilling NED.....	49
Figure 18: Overview of radiation detection process .....	51
Figure 19: Working scheme for a scintillation detector.....	53
Figure 20: Energy band structure in an inorganic scintillator.....	53
Figure 21: Wavelength stokes shift.....	54
Figure 22: Working principle for a typical PMT .....	57
Figure 23: Geiger mode avalanche photodiodes.....	59
Figure 24: Sensl Silicon photomultiplier schema and sensl C-series product view .....	61
Figure 25: Pulses shape comparison for various SiPM connections .....	61
Figure 26: Basic principle of a charge sensitive preamplifier .....	63

Figure 27: Output voltage pulse shapes view for a simple charge sensitive preamplifier	63
Figure 28: Schema of an AC coupled resistive feedback charge sensitive preamplifier..	64
Figure 29: Output voltage pulse shapes view for a resistive feedback charge sensitive preamplifier.....	64
Figure 30: Functionality of shaper system.....	65
Figure 31: Simple CR-RC shaper schema and its response to preamplifier output.....	66
Figure 32: Schema of preamplifier circuit and CR shaper .....	67
Figure 33: Schema of amplifier circuit .....	67
Figure 34: Schema of peak detector circuit .....	67
Figure 35: Pulse discrimination by a two-level discriminator .....	68
Figure 36: Block diagram for a simple single channel analyzer (SCA) .....	69
Figure 37: Electronic schema of a LLD system.....	70
Figure 38: Electronic scheme of a comparator and of a monostable.....	71
Figure 39: Representation of an ADC module .....	72
Figure 40: Block diagram of a multi-channel analyzer (MCA) designed for pulse height analysis.....	74
Figure 41: MCA channel histogram of $^{22}\text{Na}$ as measured by AXINT sensors.....	74
Figure 42: MCA energy histogram of $^{22}\text{Na}$ as measured by AXINT sensors .....	75
Figure 43: Configured pin of dsPIC33EP512MC806.....	76
Figure 44: Electronic schema view of CAN transceiver connections .....	77
Figure 45: General schematic of CAN network .....	78
Figure 46: Electronic view of switch transistor .....	79
Figure 47: LabVIEW Windows: Front Panel and Block Diagram .....	81
Figure 48: Example of Gaussian frequency distribution .....	83
Figure 49: Distribution expected for the net counts $N_S$ in absence of statistical fluctuations.....	86
Figure 50: Probability distribution expected for the net counts $N_S$ in case of no real activity.....	87
Figure 51: Probability distribution expected for the net counts $N_S$ in case of real activity .....	88

Figure 52: Random history of a neutron incident on a slab of material that can undergo fission.....	92
Figure 53: Sample 3D geometry view for determination of NaI detection efficiency by MCNP simulations.....	93
Figure 54: CSG methodology for MCNP6.....	94
Figure 55: MCNP surfaces block sample code.....	95
Figure 56: Cell cards specification for MCNP sample code.....	96
Figure 57: Material specification for MCNP sample code.....	97
Figure 58: Mode specification for MCNP sample code.....	97
Figure 59: Source specification for MCNP sample code.....	98
Figure 60: Tally specification for MCNP sample code.....	98
Figure 61: MCNP sample codes.....	99
Figure 62: Activity distribution of radiotracers modeled by CEA/L3MR.....	101
Figure 63: Hybrid geometry construction.....	102
Figure 64: Basic mesh elements and construction of 3D meshes via Abaqus/CAE.....	103
Figure 65: Sample input part file of Abaqus/CAE used for MCNP6 unstructured mesh.....	104
Figure 66: Two instance construction for Abaqus/CAE sample file.....	104
Figure 67: Assembly example for Abaqus/CAE sample file.....	105
Figure 68: Example of material and density for Abaqus/CAE sample file.....	105
Figure 69: Abaqus/CAE sample file.....	106
Figure 70: The process of CAD conversion.....	107
Figure 71: Example of STL file structure for one triangle facets.....	108
Figure 72: Example of STL file content.....	109
Figure 73: Generation of tetrahedral meshes from TetGen software.....	110
Figure 74: Node and element output files created by TetGen software.....	110
Figure 75: Labview development from 3D meshes to MCNP6 code.....	111
Figure 76: General source code view of Labview to adapt a MCNP6 source code.....	112
Figure 77: Raw data of CFD file.....	113
Figure 78: View of CFD list nodes.....	114

Figure 79: Supplementary imported CAD unstructured meshes view .....	115
Figure 80: Combination of CFD reformulated data with CAD data .....	116
Figure 81: <sup>22</sup> Na and HTO modeling scenario in DRN1202 drilling for dimensional calculations .....	120
Figure 82: <sup>36</sup> Cl and HTO modeling scenario in DRN1203 drilling for dimensional calculations .....	121
Figure 83: Simulation of HTO concentration cartography .....	125
Figure 84: HTO (left) and <sup>22</sup> Na concentration profile with different year's evolution ..	125
Figure 85: 3D mesh simulations used for <sup>22</sup> Na injection tests.....	126
Figure 86 : Sum of 4 crystals count rate on each axis (Top part), each crystal count rate on each axis (Bottom part) (S1: Reference simulation).....	130
Figure 87: Sum of 4 crystals count rate on each axis (Simulation S2).....	130
Figure 88: Each crystal count rate on each axis (Simulation S3) .....	131
Figure 89: Sum of 4 crystals count rate on each axis (Simulation S4).....	131
Figure 90: Sum of 4 crystals count rate on each axis (Simulation S5).....	132
Figure 91: Sum of 4 crystals count rate on each axis (Simulation S6).....	133
Figure 92: Evolution of the count rate according to the axis Y with different diffusion coefficient .....	134
Figure 93: Evolution of the count rate according to different axis Y and Z with different anisotropy.....	134
Figure 94: Considered geometries for the injection of <sup>22</sup> Na and <sup>36</sup> Cl in situ test .....	137
Figure 95: Main component of the beta sensor (top) and the complete design of the beta sensor with its mechanical part (bottom) .....	140
Figure 96: Crystal design for Beta sensors (Beta 2 left, Beta 1 right).....	141
Figure 97: Experimental measurement setup for calibration of <sup>36</sup> Cl solution .....	142
Figure 98: Calibration curves of beta detection sensors including background noise counts .....	145
Figure 99 : Calibration curves of beta detection sensors after subtraction of background counts .....	146

Figure 100: Comparisons of SNR for beta sensors in response of standard $^{36}\text{Cl}$ solution .....	146
Figure 101 : Noise measurements using beta 2 sensor in the argillite milieu.....	148
Figure 102 : Comparison of net counts CPM as a function of volume activity for beta sensors.....	149
Figure 103: Scheme of geometry used for MCNP simulation.....	151
Figure 104 : Variations of detected activity (in count per second) and of detection efficiency in response to different volume of $^{36}\text{Cl}$ solution.....	152
Figure 105: Variations of signal to noise ratio (SNR) and detection efficiency depending on crystal thickness .....	154
Figure 106: Comparison of energy resolution obtained from $^{239}\text{Pu}$ sample .....	155
Figure 107: 3D view of gamma sensor design (Top part), view of experimental sensors design (Bottom part) .....	156
Figure 108: View of different host rock sample thickness and of gamma experimental setup with $^{241}\text{Am}$ @ 1MBq .....	157
Figure 109: Linear transmission curve of measurements .....	159
Figure 110: Source position in calibration of gamma crystal .....	160
Figure 111 : Energy histogram for 4 gamma crystals.....	160
Figure 112 : Energy histogram Gaussian fit for crystal ID51 .....	161
Figure 113: Calibrated sensors'background counts .....	162
Figure 114: Interface to detect on line sensors and select the radioactivity source to be calibrated.....	163
Figure 115: Interface to get sensor energy histograms .....	163
Figure 116: Interface refined gain to adjust Gaussian center at channel 1500 .....	164
Figure 117: Interface to show the Gaussien fitting parameters and calibration results .	164
Figure 118: AXINT real-time monitoring system .....	165
Figure 119: DRN1203: In situ experimental setup.....	166
Figure 120 : Energy histogram for crystal ID51 with 2 different activities.....	167
Figure 121 : Linear fit of different source activities to validate the calibration of $^{22}\text{Na}$ .	168

Figure 122: Simulation geometry view at $px=0$ in study of the stopping power of host rock at low energy for $^{241}\text{Am}$ .....	169
Figure 123 : Linear fit of simulation MCNP results with small variations of source position.....	171
Figure 124 : Linear fit of simulation MCNP results with small variations of $\text{SiO}_2$ thickness.....	172
Figure 125: Detection of $^{22}\text{Na}$ in host rock milieu.....	174
Figure 126: Detection of $^{22}\text{Na}$ via measurements and simulations and with its detection limits after 150 minutes accumulation.....	175

## List of tables:

Table 1: Classification of radioactive waste and status in France .....	19
Table 2: Summary of diffusion coefficients obtained with COX clay .....	24
Table 3: Mineralogical composition of the COX .....	38
Table 4: Classification and properties of COX clay groups .....	39
Table 5: Lists of actinide candidates and arguments for radionuclide injection in situ diffusion test.....	48
Table 6: Principal tests in NED gallery .....	49
Table 7: Density, light yield and decay time of some commonly used inorganic scintillators.....	55
Table 8: Pin function descriptions .....	73
Table 9: MCNP surface cards used for sample codes.....	94
Table 10: Essential information requirements for MCNP data cards.....	96
Table 11: Source specification in MCNP data cards .....	98
Table 12: Tally specification in MCNP data cards.....	98
Table 13: Parameter setting in 3D simulations for $^{22}\text{Na}$ .....	127
Table 14: Proposition for $^{22}\text{Na}$ and $^{36}\text{Cl}$ dimensional design.....	136
Table 15: Measurements using beta 1 with standard solution .....	144
Table 16 : The determination of two unknown solutions .....	147
Table 17: Calculation of sigma and detection limits in 2 methodologies.....	150
Table 18: Determination of noise sigma and D.L @1h and @24h.....	151
Table 19 : The variations in CPS of signal to noise ratio under different crystal length	153
Table 20: Study of host rock stopping power property of $^{241}\text{Am}$ .....	158
Table 26 : Calibrations of 4 gamma crystals .....	162
Table 27 : Counts response to 2 different activities.....	167
Table 23: List of MCNP host rock elements .....	169
Table 24 : Influence of source position incertitude to the study of rocks attenuation coefficient .....	171

Table 25 : Influence of incertitude of source position in determination of host rock attenuation coefficient property .....	171
Table 26: The influence of SiO <sub>2</sub> thickness for determination of host rock attenuation coefficient property .....	172
Table 27: Comparison of host rock attenuation coefficient property via simulation and measurements .....	173
Table 28: Simulation and measurement results in study of <sup>22</sup> Na.....	175

## Abstract

In the context of nuclear waste management in France, Andra (Agence National pour la gestion des Déchets RAdioactive) was established to manage all the radioactive waste produced on French Territory. Andra has been assigned the task to demonstrate the feasibility of a radioactive waste disposal facility at a depth of 490 m within the Callovian-Oxfordian (COX) mudstone. For this objective, an underground research laboratory (URL) has been build. The present work is the continuation of former diffusion studies that have been held at Andra underground laboratory (S. Dewonck, 2007).

I worked for AXINT company which is specialized in radiation detection technology. A cooperation has been established between AXINT and Andra for the research of radionuclide diffusion tests, and this gave rise to my PhD research works. A new in situ experiment was considered by Andra for the study of the radionuclide migration. Compared to previous experiments, this new in situ diffusion test required longer distance (hundreds of mm), longer time-scale (over 10 years), and real time in situ monitoring of radionuclides migration. To fulfill these conditions, the work was organized as following:

1. Conception and dimensional design of the Diffusion of Radio Nuclide (DRN) experiments in solving emission of beta and gamma radiations
2. Development of corresponding beta and gamma monitoring systems by means of sensors located in peripheral boreholes

In the first part of my work, I developed the Monte Carlo N-Particle transport (MCNP6) code that was used for the parameters optimization of DRN designs. For that purpose, I developed a general auto conversion algorithm that allows the user to convert both Computer-aided design (CAD) data, Computational fluid dynamics (CFD) data and mixed CAD and CFD data into MCNP6 geometry description code. Then, a better improvement of sensors design had been made and validated through additional MCNP simulations.

In the second part, AXINT developed the first prototype of beta and gamma in situ monitoring sensor systems. I participated to the project after a deep understanding of radioactive sensors development, that included technologies on electronic design of circuit, digital signal process, acquisition system and data treatment. After that I developed the microcontroller unit (MCU) program and software for the prototype sensors, and both beta and gamma sensors were fabricated. The beta sensors were calibrated with solution  $^{36}\text{Cl}$  in term of sensitivity and limits of detection (L.D). For gamma sensors, various experimental setups have been developed for measurements such as the sensor calibration with different activity sources ( $^{22}\text{Na}$  and  $^{241}\text{Am}$ ), the determination of host rock stopping power of  $^{241}\text{Am}$ . After all these feedback measurements information acquired with the first prototype sensors, we have designed an optimized version to be used for the DRN experiment.

# CHAPTER 1 The art of tracers in the context of nuclear waste management

## 1.1 Global context

The application of nuclear science emerged at the end of the 19th century. This included discovery of X-rays by Wilhelm Roentgen in 1895, radioactivity emitted by uranium salt by Henri Becquerel in 1896 and electron by J. J. Thompson in 1897 (Jain, 2009). Up to date, nuclear science has led to wide scale applications in research, medicine, industry and in the generation of electricity by nuclear fission. It is well known that most of the radioactive waste in France is generated as a result of electricity production. In France, by 2011 there were 58 electronuclear reactors (operated by EDF, the French utility), meaning 129 GW of installed power. In 2014, they generated 415.9 TWh of net electricity, representing 77% of the total electricity production (Andra-ASN-CEA-IRSN, 2016). Waste from the nuclear power industry accounted for 59% of the total inventory of 31 December 2010, while the remainder came from research (26%), defense (11%), industrial nuclear applications (3%) and medical applications (1%) (News, 2012). France had an inventory of radioactive wastes at some 1.32 million cubic meters in 2010. Assuming that France's current fleet of nuclear power reactors are granted for 50-year operating lives and that all used fuel is reprocessed, Andra predicts that the national radioactive waste inventory will increase to 1.9 million m<sup>3</sup> by 2020 (News, 2012).

The French National Radioactive Waste Management Agency (Andra), created by the Act of Parliament of 30 December 1991, is responsible for managing all the radioactive waste produced on French Territory. It is supervised by the French Ministries of Industry, Research and the Environment (Radioactifs, 2006). The missions of the

National radioactive waste management Agency are defined in article L.542-12 of the Environment Code. In particular, Andra is responsible for (SITE, 2009):

- Producing and publishing the inventory and the locations of radioactive materials and waste in France.
- Steering research and studies on storage and deep geological disposal.
- Designing, installing and managing storage facilities or disposal facilities for radioactive waste taking account of long term prospects for production and management of this waste and to carry out all the studies necessary for this purpose.
- Radioactive waste management and remediation of orphan radioactively polluted sites.
- Providing the public with information about the management of radioactive waste.

## 1.2 Classification of radioactive waste in France

Radioactive waste can be defined as any material that is radioactive for which no further use is envisaged. The objective of radioactive waste management is to deal with radioactive waste in a manner that protects human health and the environment now and in the future without imposing undue burdens on future generations. To meet the requirements for its safe management, waste classification considers four categories according to activity level. Then each waste category is subdivided according to half-lives of the radionuclides it contains (Table 1) (Andra-ASN-CEA-IRSN, 2016).

Half-life Activity	Very short lifetime Half-life < 100 days	Short lifetime Half-life ≤ 31 years <sup>(1)</sup>	Long lifetime Half-life > 31 years <sup>(1)</sup>
Very low level	Stored to allow radioactive decay on the production site then disposed of adopting conventional solutions.	Surface disposal facility (Very-low-level waste disposal facility in north-eastern France (Aube))	
Low level		Surface disposal facility (Low- and intermediate-level waste disposal facility in north-eastern France (Aube)) <sup>(2)</sup>	Near-surface disposal facility <sup>(3)</sup> studied in accordance with Article 4 of the Planning Act of 28 June 2006 on the sustainable management of radioactive materials and waste.
Intermediate level			Deep disposal facility <sup>(4)</sup> studied in accordance with Article 3 of the Planning Act of 28 June 2006 on the sustainable management of radioactive materials and waste.
High level		Deep disposal facility <sup>(4)</sup> studied in accordance with Article 3 of the Planning Act of 28 June 2006 on the sustainable management of radioactive materials and waste.	

Table 1: Classification of radioactive waste and status in France

(Andra-ASN-CEA-IRSN, 2016)

**Very-low-level waste** mostly comes from dismantling of nuclear facilities and conventional industrial plants in various sectors (chemicals, metallurgy, energy production, etc.) which used naturally radioactive materials. It also originates from clean-up and rehabilitation operations on sites which were formerly polluted by radioactivity. Around 50% of this waste is “common industrial waste” (scrap metal and plastics), 40% is inert waste (concrete, bricks, earth, rubble, etc.) and 10% is “special waste” made of materials such as sludge and, in some cases, pulverulent waste (ashes, etc.). Very-low-level waste has a radioactivity level close to that of naturally occurring radioactivity (between 1 and 100 Bq/g). It contains short-lived and/or long-lived radionuclides. This waste is managed at the Andra CSTFA disposal facility located in the Aube district.

**Low-level long-lived waste** is mainly “radium-bearing” waste and waste termed “graphite” because it contains this element, a very pure form of carbon. Radium-bearing waste comes from processing of various minerals used, for example, in fine metallurgy. Graphite waste was generated during dismantling of first generation nuclear reactors (graphite-moderated gas-cooled reactors), which have now been decommissioned. There

are other sources of LLW-LL, such as old radioactive objects (radium fountains...), sealed sources (lightning conductors, <sup>241</sup>Am smoke detectors, etc.). There is also some bituminized waste in this category. In most cases, production has either ceased or must cease shortly. LLW-LL contains, mostly, long-lived radionuclides. Disposal for this type of waste is currently under study.

**Low and intermediate level short-lived waste** mostly comes from the nuclear power industry and the activities of the French atomic and alternative energy commission (CEA). It also includes waste from hospitals, research and university laboratories. It may also result from clean-up and dismantling operations. It essentially includes waste related to maintenance (clothes, tools, gloves, filters, etc.) and to the operation of nuclear facilities, such as treatment of gaseous and liquid effluents. This waste contains short-lived radionuclides, such as cobalt-60 and caesium-137, and may also contain strictly limited amounts of long-lived radionuclides. This waste is managed at the Andra CSFMA waste disposal facility located in the Aube district.

The fuel used to operate current nuclear reactors is composed of a uranium assembly sometimes with plutonium. Over time, this fuel becomes less efficient. It then needs recycling, usually in the AREVA plant (La Hague). The metal structures surrounding this fuel are cut into small sections in order to later separate the uranium and plutonium from non-reusable residues. **Intermediate-level long-lived waste (ILW-LL)** is mostly composed of these metal structures (cladding, hulls and end caps). It also comes from residues (waste from effluent treatment, equipment, etc.) originating from the operation and maintenance of nuclear facilities. Disposal for this type of waste is currently under study.

During recycling, spent nuclear fuel is immersed in a chemical solution which enables the uranium and plutonium to be separated from the non-reusable residues. These highly radioactive residues make up **high-level waste (HLW)**. It represents 3 to 5% of the spent fuel and is composed of fission products (caesium-134 and -137 and strontium-90), activation products (cobalt-60) and minor actinides (curium-244 and americium-241).

Because of its high radioactivity, some of this waste gives off heat. Disposal for this type of waste is currently under study.

As illustrated in Table 1, Disposal of low and intermediate level radioactive wastes can be implemented on surface, but some intermediate level or high level that contains long lived radioactivity requires disposal at greater depths. In France, a 500-meter deep disposal concept in the Centre Industriel de stockade GEOlogique (CIGEO) has been designed by Andra (Figure 1).

Zone 1: This zone will be used to receive, inspect and prepare waste packages before transfer to the underground facility.

Zone 2: In this zone, waste packages will be transported to underground facility (zone 3) through ramps.

Zone3: This will be the zone for deep disposal of High Level waste and long lived Intermediate Level waste

Zone4: Various shafts will connect the underground facility to the surface work zone. They will be used to transport personnel, materials and equipment up and down.

Zone5: This zone will be used in particular as a base for excavating and building the underground structures.

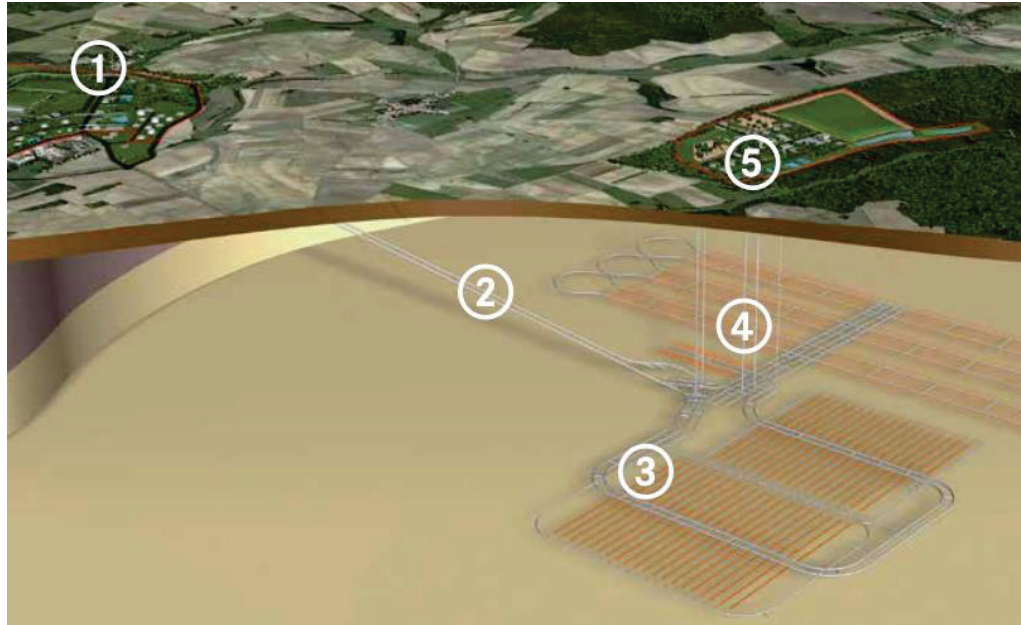


Figure 1: General layout of CIGEO facilities

### 1.3 ANDRA: Underground Research Laboratory (URL)

#### ***Meuse/Haute-Marne Underground Research Laboratory:***

Deep geological disposal of High Level waste and long lived Intermediate Level Waste are today Andra's major project. Argillaceous media are being considered in numerous countries as potential host rocks for the geological disposal of radioactive waste (Norris S. , 2014). Argillaceous media present as the geological barrier or as part of the engineered barrier have a number of favorable generic properties, for example, homogeneity, low groundwater flow, chemical buffering, propensity for plastic deformation and self-sealing of fractures by swelling, and marked capacity to chemically and physically retard the migration of radionuclides (Norris, 2014). In France, an

underground research laboratory (URL) has been built by Andra to investigate the feasibility of a radioactive waste disposal facility at a depth of 490 m within the Callovian-Oxfordian (COX) mudstone. The underground installations consist of two shafts and drift networks (J. Delay, 2010) (Figure 2). The main shaft, 5 meters in diameter after lining, allows access to a 445 meter deep drift network and to the 490 meter deep main drift network. The auxiliary shaft, 4 meters in diameter after lining, is also connected to the URL main level.

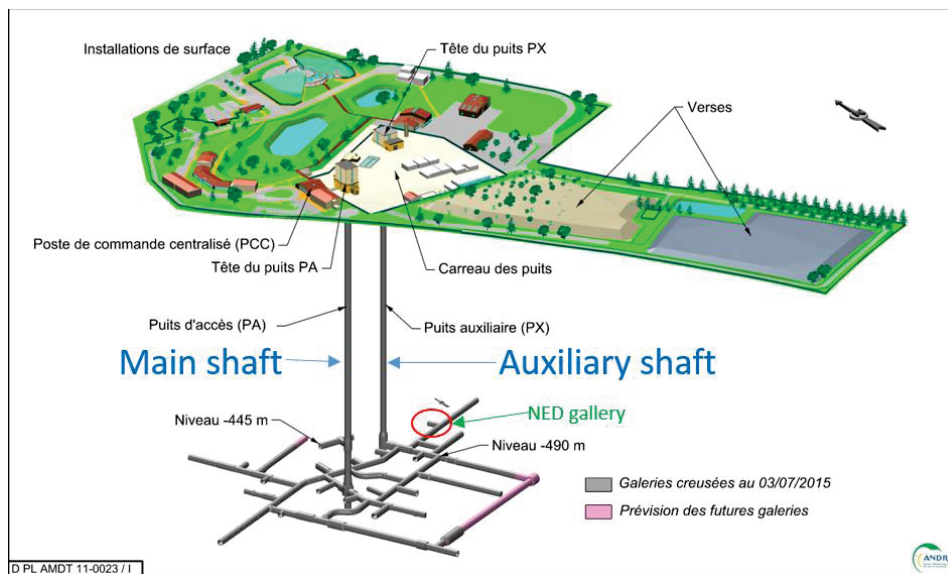


Figure 2: General view of the Meuse Haute Marne Underground research laboratory  
(J. Delay, 2010)

The URL research comprising the characterization of the confining properties of the argillaceous rock through in situ hydrogeological tests, chemical measurements and diffusion experiments (Delay, 2006) led to the publication of the dossier in which Andra demonstrated the basic feasibility of a deep geological repository for HL and IL-LL waste. Our work focus on the investigation and quantification of the radionuclide diffusion through the Callovian-Oxfordian rock, one of the most important parameters for Performance Assessment (PA) calculations of clay barriers. Different diffusion experiences were applied at a laboratory scale to analyze the diffusion behavior of a wide

range of Radionuclides (RN). For example, the effective diffusion coefficient had been measured (Table 2) in the research work of Garcia-Gutierrez (M. García-Gutiérrez, 2009). The ranges of variations of diffusion coefficient were taken into account by bedding anisotropy and mudstone layer impact. The first three listed radio tracers in Table 2 were identified as the quickest neutral, anionic, cationic species respectively.

Tracer	D (m <sup>2</sup> /s)
HTO	$D_e = (3.0 \pm 1.2) \cdot 10^{-11}$
<sup>36</sup> Cl <sup>-</sup>	$D_e = (6.6 \pm 2.2) \cdot 10^{-12}$
<sup>22</sup> Na <sup>+</sup>	$D_e = (4.4 \pm 1.6) \cdot 10^{-11}$
<sup>75</sup> Se	$D_a = (1.1 \pm 0.3) \cdot 10^{-12}$
<sup>85</sup> Sr	$D_a = (7.2 \pm 0.6) \cdot 10^{-12}$
<sup>137</sup> Cs	$D_a = (1.6 \pm 0.6) \cdot 10^{-13}$
<sup>60</sup> Co	$D_a = (1.5 \pm 0.4) \cdot 10^{-13}$
<sup>152</sup> Eu	$D_a = (4.6 \pm 1.8) \cdot 10^{-15}$

Table 2: Summary of diffusion coefficients obtained with COX clay  
(M. García-Gutiérrez, 2009).

On the other hand, seven in situ diffusion tests based on injection of radiotracers have been previously carried out on site at three different location. (Dewonck et al., 2009)

#### **Previous in situ diffusion tests (DIR) in the ANDRA's URL:**

The design of these tests was based on experiments performed in the Swiss Mont Terri URL in Opalinus Clay rock (Wersin, 2008) (Palut, 2003) (Wersin., 2004). At the bottom of vertical downward boreholes, synthetic water circulated in contact with the rock. Tracers were added to the synthetic water when stable chemical and hydrostatic state had been reached. The tracers injected were radioactive (Tritiated water (HTO), <sup>125</sup>I, <sup>36</sup>Cl, <sup>22</sup>Na, <sup>85</sup>Sr, <sup>134</sup>Cs) and were representative of the chemical and physical behaviors of the different radionuclides in the waste. A circulation pump was maintaining a

homogeneous concentration of the tracers in the test interval. Tracer contents in the circulating fluid were regularly measured by water sampling and analyzing. The decrease in activity was monitored over time and at the end of the experiment, the rock around the injection chamber where tracers diffused, was retrieved by over-coring to analyze tracers' concentration profiles within the rock. Since 2004, similar in situ experiments were also performed at Mont Terri and modelled by several teams (Wersin, 2008) (Yi, 2012) (Gimmi, 2014). Finally, the first set of in situ diffusion tests of COX had given following results (S. Dewonck, 2007):

1. Compared to tritiated water, which is considered as a reference, the relative activity of anionic species decreases more slowly. At the opposite, the relative activity of cationic species decreases faster than that of tritiated water.
2. For each tracer injected, no significant difference of diffusion behavior between different types of mineralogy related to geological layer were observed.
3. It is imperative to take into account a drilling disturbed zone around the borehole of 2-3 cm thickness with a higher porosity than the bulk rock. Beyond 3 cm around the wall of the borehole, the diffusion parameters obtained are consistent with those obtained from drill core samples and are representative of the undisturbed rock.

#### **Previous in situ diffusion tests (DIR) in the ANDRA's URL:**

The design of these tests was based on experiments performed in the Swiss Mont Terri URL in Opalinus Clay rock (Wersin, 2008) (Palut, 2003) (Wersin., 2004). At the bottom of vertical downward boreholes, synthetic water circulated in contact with the rock. Tracers were added to the synthetic water when stable chemical and hydrostatic state had been reached. The tracers injected were radioactive (Tritiated water (HTO),  $^{125}\text{I}$ ,  $^{36}\text{Cl}$ ,  $^{22}\text{Na}$ ,  $^{85}\text{Sr}$ ,  $^{134}\text{Cs}$ ) and were representative of the chemical and physical behaviors of the different radionuclides in the waste. A circulation pump was maintaining a

homogeneous concentration of the tracers in the test interval. Tracer contents in the circulating fluid were regularly measured by water sampling and analyzing. The decrease in activity was monitored over time and at the end of the experiment, the rock around the injection chamber where tracers diffused, was retrieved by over-coring to analyze tracers' concentration profiles within the rock. Since 2004, similar in situ experiments were also performed at Mont Terri and modelled by several teams (Wersin, 2008) (Yi, 2012) (Gimmi, 2014). Finally, the first set of in situ diffusion tests of COX had given following results (S. Dewonck, 2007):

1. Compared to tritiated water, which is considered as a reference, the relative activity of anionic species decreases more slowly. At the opposite, the relative activity of cationic species decreases faster than that of tritiated water.
2. For each tracer injected, no significant difference of diffusion behavior between different types of mineralogy related to geological layer were observed.
3. It is imperative to take into account a drilling disturbed zone around the borehole of 2-3 cm thickness with a higher porosity than the bulk rock. Beyond 3 cm around the wall of the borehole, the diffusion parameters obtained are consistent with those obtained from drill core samples and are representative of the undisturbed rock.

#### **Development of a new in situ diffusion test:**

One of the “time-consuming” and technically challenging part of previous in situ diffusion tests was the overcoring of the experiments and measurements of the diffusion profiles in the solid. Thus many other solutions have been proposed to analyze diffusion behavior of radionuclides, such as in the review of Jacques Pocachard, in which he proposed and patented 2 novel methodologies (the concentration echo and extension of the macropore column) in situ measurement of diffusivity (Jacques Pocachard, 2005). A new in situ experiment was considered and selected by ANDRA as well. The aim of this

experiment is to collect data on the migration of radionuclides, by means of experimental set-up as contrasting as possible with previous studies. This includes larger space scale (hundreds of mm), longer time-scale (over 10 years) and if possible in situ monitoring of radionuclides migration through the argillaceous rock during the experiment. Tracers are injected simultaneously within a synthetic solution through a central injection borehole and a circulation system.

The purpose of our work was to develop beta and gamma monitoring system to evaluate the possibility to monitor in situ both tracers diffusion by means of sensors located in peripheral boreholes. To this aim, we evaluated the performance of both beta and gamma sensor system. This included optimization of the design, characterization of sensitivity, limits of detection (L.D). Then we evaluated the possibility to detect a  $^{36}\text{Cl}$  and  $^{22}\text{Na}$  plume as a function of time and space and the relevance of such a device in the context of in situ experiments.

## 1.4 Art of tracers

### 1.4.1 Generalities

Tracer methods are a powerful diagnostic tool in various application fields. Tracers are defined as substances that can be introduced into a mechanical or a biological system allowing the determination of the position or the distribution of a process. For example, it is possible to find tracers in medicine (contrast agents), anti-counterfeiting or geological exploration. The principle of a tracer can be resumed by the following “A tracer tells you exactly what it sees, thereby optimizing the process” (Tor Bjørnstad, 2015). The tracer methodology consists of different steps as showed in Figure 3, all these processes can be derived from many fields of science including:

- Chemistry for the selection and production of tracers
- Physics for the simulation process and detection methods

- Mathematics for the statistical analyses
- Electronics for the signal treatment
- Information technology for embedded system and for the data acquisition and analysis

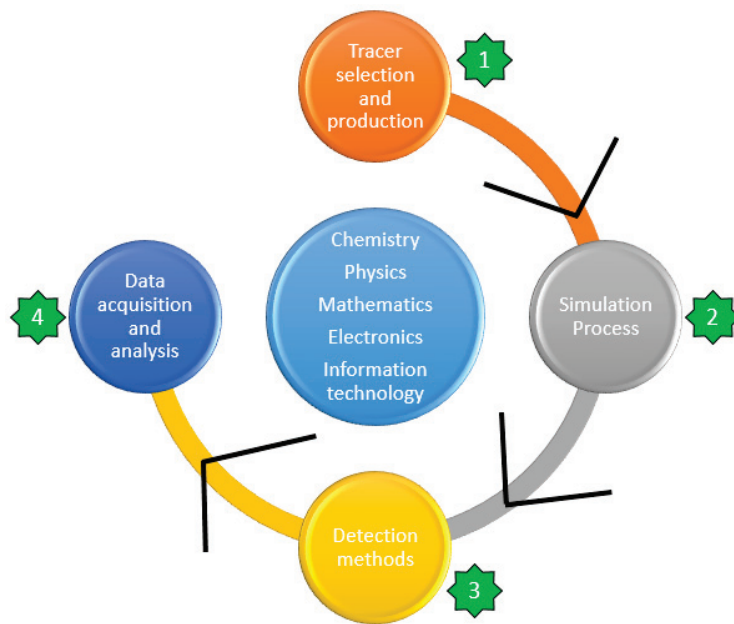


Figure 3 : Tracer methodology and interdisciplinary aspects

The first consideration in designing a tracer methodology is the selection of tracers. It is not only the first step but also the most important one that decides the following exploitation methods. The tracers can be classified into different categories such as radioactive chemical or nature tracers. While it is always a difficulty in the selection of the tracers for use in a tracing process, because a variety of selection criteria are required (H.Preud'homme, 2012). A tracer:

- must be inert, be highly stable thermally, chemically, physically, and biologically for several years
- must follow the phase in which it is injected. Not be absorbed and influenced the system

- must not influence the physical properties of the system
- must not be present before injection in the system
- must be detectable in very low concentration with simple and fast analytical methods to reduce the costs and the environmental impact via small injected quantities.
- must be at an acceptably low level of toxicity

### 1.4.2 Radiotracers

The radioactive tracers are the most frequently used as tracer methodology. It was used across a large industrial spectrum, the petroleum, and petrochemical industries, mineral processing and waste water treatment are identified as the most appropriate target beneficiaries of radiotracer application (IAEA, 2001) The first interest of radiotracers or called isotopes is that all the isotopes of a given element will present the same chemical properties, because of same number of protons. Another advantage of radiotracer experiments include being detectable even at very low concentrations which means very small quantities injected into the investigation system.

As radiotracers are identified as radioactive substances that can cause radiation hazards to the population and environment risks, a radiotracer must be chosen based on the inherent properties.

### 1.4.3 The half-life and types of radiotracers

The first important criteria in the selection of radiotracer is its half-life. As radionuclides are unstable and decay by emission of particle (alpha or beta) or  $\gamma$  - radiation to achieve stable configuration of protons and neutrons in the nucleus, the term Half-life (abbreviated  $T_{1/2}$ ) means the time required for a quantity to reduce to half its initial value. It is given by:

$$\text{Equation 1} \quad T_{1/2} = 0.693\tau = \frac{\ln(2)}{\lambda} \quad (\tau = \frac{1}{\lambda})$$

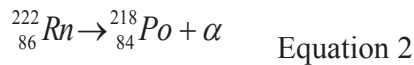
With  $\lambda$ : Decay constant

The second criteria in the selection of radiotracer is related to the emission of radiation types expected to be detected and traced. Differ to chemical reaction which is related to electronic structure around an atom, the radioactive radiations are original of nucleus effect of an atom. In theory, it exist 2 models for nuclear structure: the liquid drop model and the shell model (Cook, 2010). In these models, radionuclides are unstable and decay by emission of particle to achieve stable configuration of protons and neutrons in the nucleus. Radioactivity is the process through which nuclei spontaneously emit subatomic particles. It was discovered by a French scientist Henri Becquerel in 1896, when he found out that an element, uranium, emitted something invisible that fogged his photographic plates. The term radioactivity was suggested by Marie Curie about 4 years later (Robert, 2012). Originally, three types of radiation were discovered:

- \_  $\alpha$ -rays (helium nuclei with only 2 protons and 2 neutrons)
- \_  $\beta$ - rays (two categories:  $\beta^-$  electrons and  $\beta^+$  positrons)
- \_ X-rays and  $\gamma$ -rays (photons)

### ***Alpha rays:***

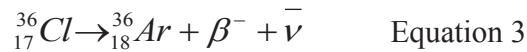
The Alpha decay occurs mostly in heavy nuclides such as uranium, radon (Equation 1) plutonium, and so on. It is a type of radioactive decay in which an atomic nucleus emits an alpha particle (helium nucleus) and thereby transforms or decays into an atom with a mass number that is reduced by four and an atomic number that is reduced by two. An alpha particle is identical to the nucleus of a helium-4 atom, which consists of two protons and two neutrons. For example, Radon-222 decays to form Polonium-218):



***Beta rays:***

- $\beta^-$  Decay:

On one hand, when a radionuclide is neutron rich—that is, the N/Z ratio is greater than that of the nearest stable nuclide—it decays by the emission of a  $\beta^-$  particle (note that it is an electron) and an antineutrino,  $\bar{\nu}$ . In the  $\beta^-$ -decay process, a neutron is converted to a proton, thus raising the atomic number Z of the product by 1:



- $\beta^+$  Decay:

On the other hand, when a radionuclide is proton rich—that is, the N/Z ratio is low relative to that of the nearest stable nuclide—it can decay by positron ( $\beta^+$ ) emission accompanied by the emission of a neutrino ( $\nu$ ), which is an opposite entity of the antineutrino. Positron emission takes place only when the energy difference (transition energy) between the parent and daughter nuclides is greater than 1.02 MeV. In  $\beta^+$  decay, essentially a proton is converted to a neutron plus a positron, thus, decreasing the atomic number Z of the daughter nuclide by 1:



The energetic  $\beta^+$  particle loses energy while passing through matter. The range of positrons is short in matter. When it loses almost all of its energy, it combines with an atomic electron of the medium and is annihilated, giving rise to **two photons of 511 KeV** emitted in opposite directions. These photons are called annihilation radiations. In

nuclear medicine, the radionuclides with positron decay as  $^{18}\text{F}$  are mostly used. Firstly, gamma ray with 511keV is sufficient for detection outside of the body. Secondly, this coincidence emission is also acted as the self-collimating nature in the use of PET imaging.

### ***X-rays and $\gamma$ -rays:***

X-rays and  $\gamma$  rays are both types of high energy (high frequency) electromagnetic radiation. They are packets of energy that have no charge or mass (weight). These packets of energy are known as photons. Because X-rays and gamma rays have the same properties, they can be grouped together in this thesis. The main difference between X-rays and gamma rays is that gamma rays are produced during nuclear decay by nuclei of atoms, whereas X-rays are produced by electrons.

#### 1.4.4 $\gamma$ -rays interactions in the matter:

When  $\gamma$  –rays produced by a decay of nuclide pass through matter, they lose energy by interaction with the orbital electrons or the nucleus of the absorber atom. The possible interactions with BGO ( $\text{Bi}_4\text{Ge}_3\text{O}_{12}$ ) matter are summarized in Figure 4 (XCOM, s.d.), it describes the photon mass attenuation coefficients depending on photon energy for scattering, absorption, and pair production.

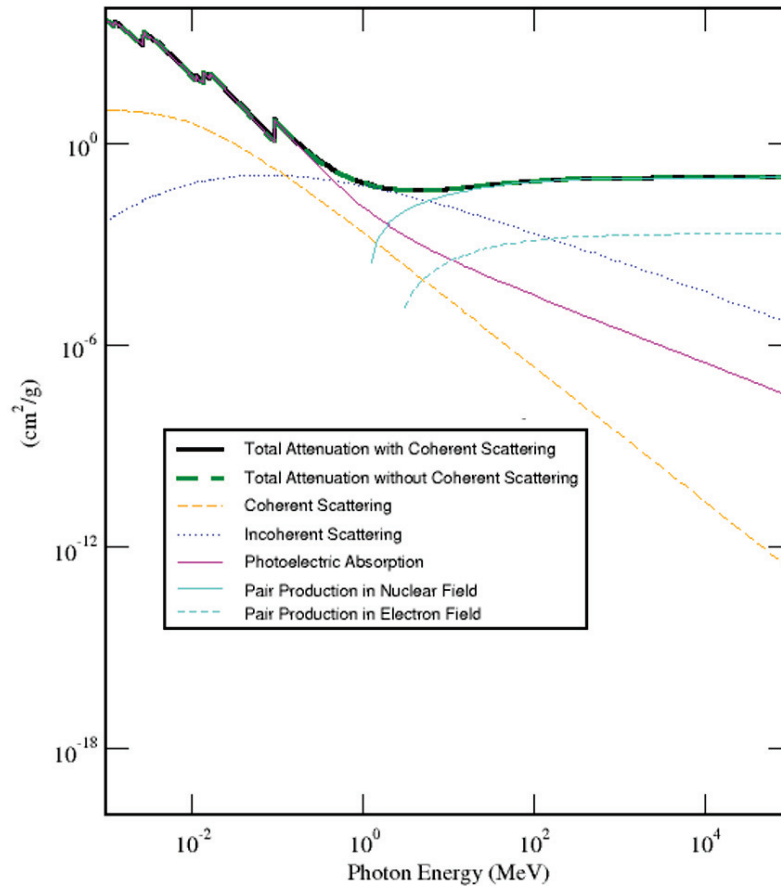


Figure 4: Dependences of photon mass attenuation coefficients ( $\text{cm}^2/\text{g}$ ) in BGO crystal on photon energy (XCOM, s.d.)

The  $\gamma$  -ray photons may lose all of their energy, or a fraction of it, in a single collision. The specific ionization of  $\gamma$  -rays is one-tenth to one-hundredth of that caused by an electron of the same energy. There is no quantity equivalent to a range of particles for  $\gamma$  -rays, but they travel a long path in the absorber before losing all energy. Therefore, the  $\gamma$  -rays are referred to as penetrating radiations. Here, an energy histogram (Figure 5) for  $^{137}\text{Cs}$  is plotted to reveal the possible  $\gamma$  -ray interactions with the absorbing matter. It works in multiple channel analyzer (MCA) mode (Detailed in section 2.2.5).

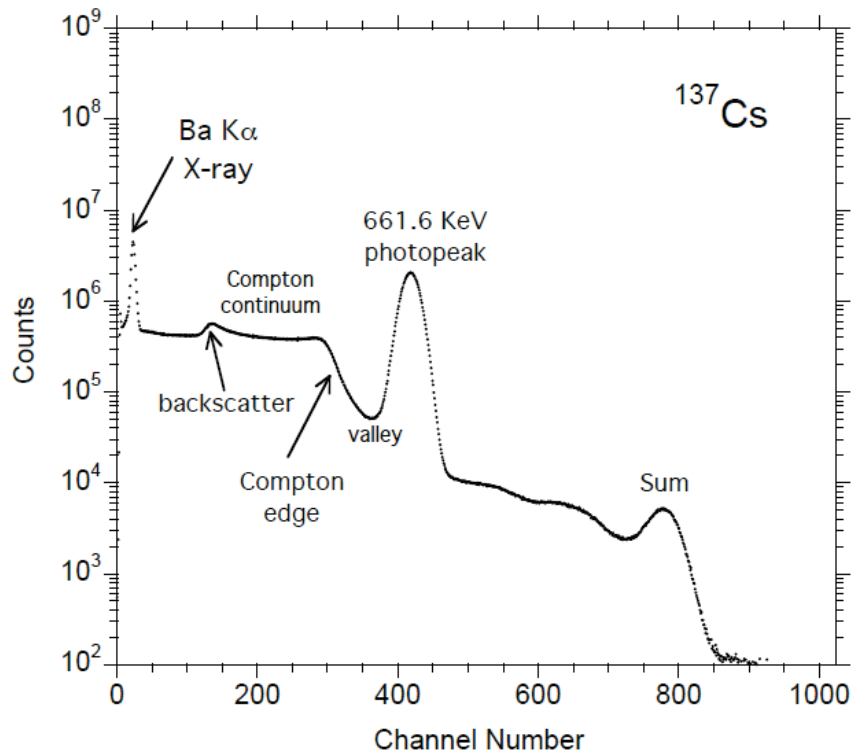


Figure 5: Energy histogram for  $^{137}\text{Cs}$

The different characteristics of  $\gamma$  –ray absorbed in a matter (Figure 5) can be explained as following:

### 1. X –ray

If the nucleus decays via electron capture or electron conversion, a hole in an inner shell is produced. When an orbiting electron fills the hole, an x-ray is emitted. In the spectra, X-rays may be seen at low channel number.

### 2. Backscatter

The backscatter peak is formed when the gamma ray undergoes directly a large-angle scattering ( $180^\circ$ ) in the material surrounding the sensor and then escapes in the detector.

### 3. Compton Scattering

Compton scattering involves the scattering of photons by charged particles where both energy and momentum are transferred to the charged particle while the photon moves off with a reduced energy and a change of momentum (Figure 6). Generally, the charged particles is an electron considered to be at rest and the photon is usually considered to be an energetic photon such as an X-ray photon or gamma ray photon. During compton scattering process, 3 major spectral feature can be produced and explained as follows:

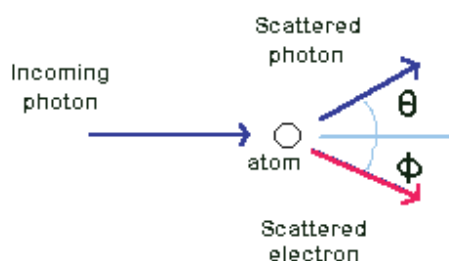


Figure 6: Compton scattering diagram

#### 3.1: The Compton Continuum

Compton interactions in which the Compton photons scatter at angles less than  $180^\circ$  and then escape the detector deposit less than the maximum energy for Compton scattering ( $E_c$ ) in the detector. The energy deposited decreases with scattering angle and since the angle can take any value, the resulting pulse heights range downward from that of  $E_c$  in an almost continuous manner producing a plateau-like feature in the spectrum.

#### 3.2: The Compton Edge

This feature is due to photons that undergo Compton scattering with a scattering angle of  $180^\circ$  and then escape the detector. The energy deposited in the detector by such an event is the maximum for Compton events ( $E_c$ ).

#### 3.3: The Valley

Since the maximum energy for Compton scattering ( $E_c$ ) is still less than the photo peak energy, thus, the region between the Compton edge and the photo peak should be void of pulses. However, due to the moderate resolution of the detector, the void is filled on either side resulting in a V-shaped depression known as the "valley".

#### **4. The Photoelectric Peak**

This is primarily the result of initial photoelectric interactions which is why it is referred to as the Photoelectric Peak or simply the photo peak. However, gamma photons that are initially Compton scattered (and thus lose energy), but do not escape the detector, can undergo subsequent photoelectric absorption and the total amount of light produced is the same as if the initial interaction had been photoelectric so a full energy pulse is observed. Thus, this peak is sometimes referred to as the total absorption peak.

#### **5. Sum Peaks**

Occasionally two gamma ray photons will be simultaneously measured in the detector. Such events give rise to measurable "sum peaks" associated with full conversion of both gamma rays.

### 1.4.5 The injections of radiotracers in the DRN experiments

#### *1.4.5.1 Mineralogy composition and structure of the COX clay:*

The COX Clay mineralogical characterization has been the subject of many studies ( (E. Gaucher a, 2004), (P. Jacquier, 2013) (Éric C. Gaucher, 2006)). The argillite

mineral fraction representing about 41 % percentage by weight (wt. %) of the COX Clay is mainly constituted of illite/muscovite/biotite (~ 14 wt. %), illite/smectite (~ 23 wt. %), and a small quantities of kaolinite (~ 2 wt. %) and chlorite (~ 2 wt. %). Quartz (~ 25 wt. %), carbonate (~ 31 wt. %) and others constitute rest of mineral fraction in COX Clay (Figure 7 and Table 3). While the solid carbonates make the medium slightly alkaline (pH: around 6.5) depending on the extent of CO<sub>2</sub> degassing of the interstitial water.

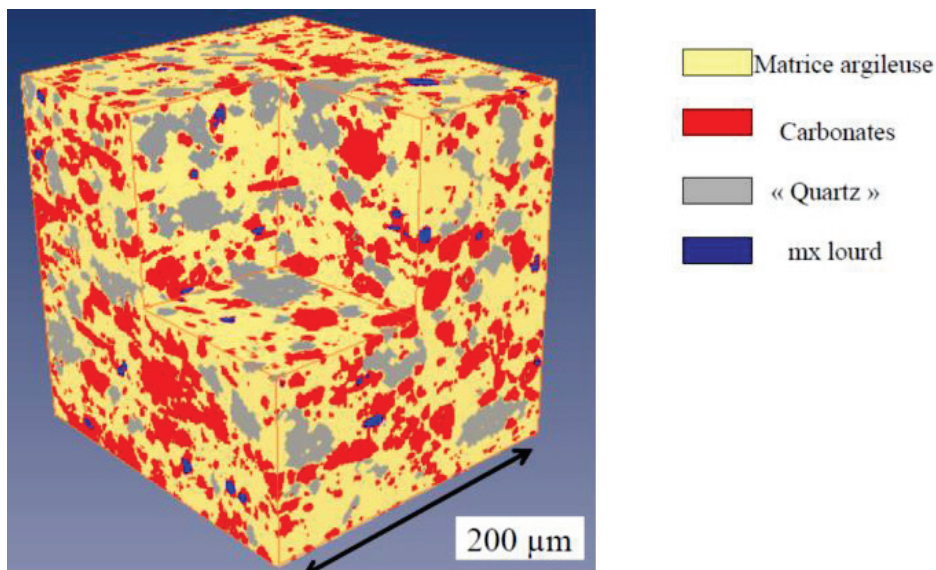


Figure 7: Composition of COX clay  
(Gerard, 2016)

Minerals	COX average percentage by weight (%)
Argillite minerals	~41
Quartz(SiO <sub>2</sub> )	~25
Carbonate(CO <sub>3</sub> <sup>2-</sup> )	~31
Others	~3
Composition of argillite minerals	

Illite(+muscovite + biotite)	~14
Illite/ smectite	~23
Kaolinite	~2
Chlorite	~2

Table 3: Mineralogical composition of the COX

(Gaucher, 2004)

### Crystallography of various argillite minerals:

In this section, we will introduce the structure of COX clay that is essential for good sorption properties for many nuclides as long term natural barrier against radionuclides dissemination.

The argillite minerals are structured by 2 types of fundamental sheet layers: Silica tetrahedral and alumina octahedral sheets (Figure 8).

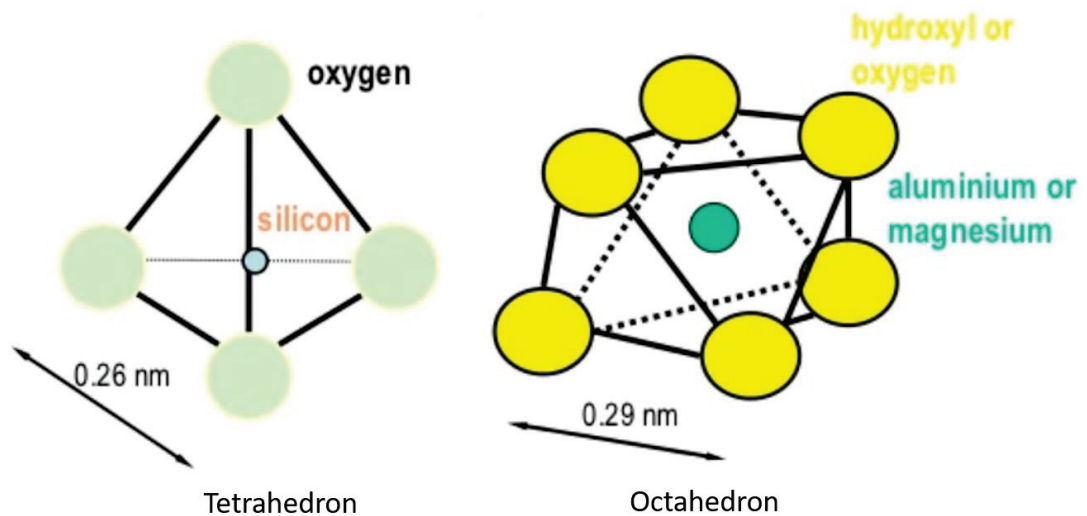


Figure 8: Basic component of clay minerals

From these basic layer component, different clay minerals are formed by different combinations of tetrahedral and octahedral sheets. Clay minerals are generally classified into three layer types based upon the number and arrangement of tetrahedral and

octahedral sheets in their basic structure. These are further separated into five groups that differ with respect to their net charge (Table 4).

Group	Layer type	Net negative charge (cmol/kg)	Spacing (nm)
Kaolinite	1:1	2-5	0.7
Illite/(+muscovite+ biotite)	2:1	15-40	1.0-2.0
Illite/ smectite	2:1	80-120	1.0-2.0
Chlorite	2:1:1	15-40	1.4

Table 4: Classification and properties of COX clay groups

1:1 clay mineral: Kaolinite (TO constitution):

The 1:1 layer minerals contain one tetrahedral and one octahedral sheet in their basic structural unit (Figure 9). This two-sheet mineral type is represented by the kaolin group, with the general formula  $Al_2Si_2O_5(OH)_4$ . It exhibits a low capacity for adsorbing cations.

Example: kaolinite  $Al_2O_3 \cdot 2SiO_2 \cdot 2H_2O$  (TO)

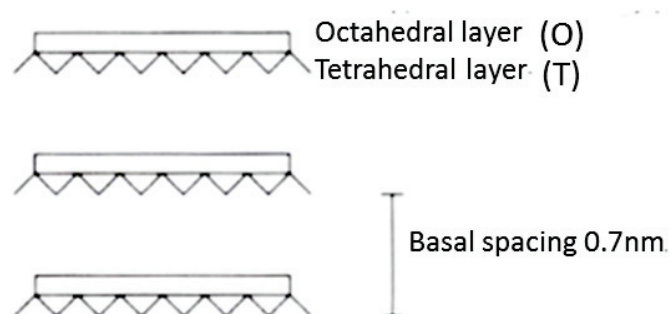


Figure 9: Structure of kaolinite

2:1 clay minerals: Illite muscovite and smectite (TOT constitution):

The joining of two tetrahedral sheets (one from each side) to one octahedral sheet produces a three-sheet mineral type, which is called 2:1 and is represented by the illite muscovite and smectite. **Illite muscovite** is formed by substitution of  $\text{Al}^{3+}$  for  $\text{Si}^{4+}$  in every fourth tetrahedral site results in an excess of one negative charge per formula unit (Figure 10). The negative charge is satisfied by monovalent cations, primarily  $\text{K}^+$ , that reside on interlayer sites between the 2:1 layers.

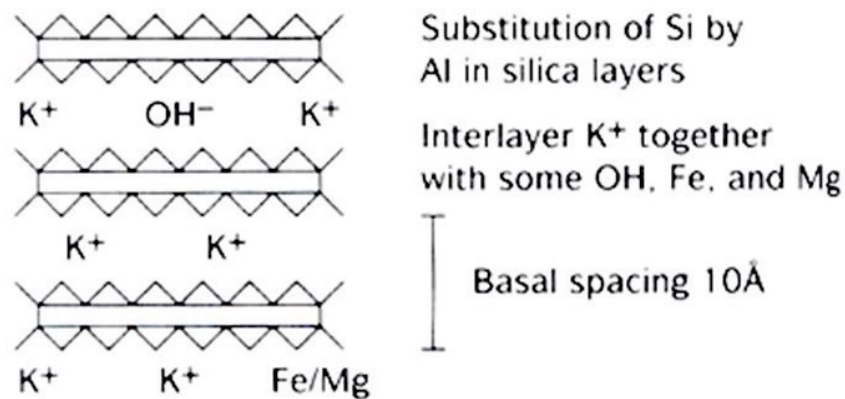
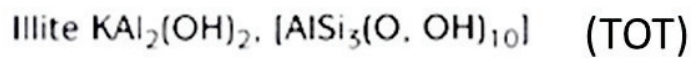


Figure 10: Structure of illite muscovite

**Illite/smectite** is a 2:1 clay generally similar to illite muscovite - a "closed face sandwiches" of tetrahedral site between two  $\text{SiO}_2$ , however some substitution of  $\text{Mg}^{2+}$  for  $\text{Al}^{3+}$  in the tetrahedral site layer creates a slight negative charge (Figure 11). That causes,

water or  $\text{OH}^-$  to substitute abundantly in cation interlayer, along with  $\text{Ca}^{2+}$ ,  $\text{K}^+$ , and  $\text{Na}^+$ .

Smectite basic formula:  $2\text{Al}_2\text{O}_3 \cdot 8\text{SiO}_2 \cdot 2\text{H}_2\text{O} \cdot n\text{H}_2\text{O}$   
 Example: montmorillonite  $(\text{Mg}, \text{Ca}) \text{O} \cdot \text{Al}_2\text{O}_3 \cdot 5\text{SiO}_2 \cdot n\text{H}_2\text{O}(\text{TOT})$

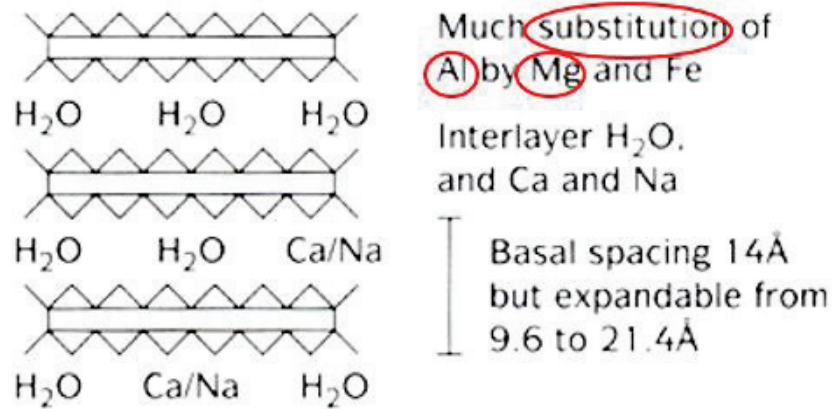


Figure 11: Structure of illite smectite

2:1:1 clay minerals: Chlorite

Chlorites are a group of minerals that exhibits a basic 2:1 layer structure similar to that described previously, but with an interlayer brucite sheet, which forms a 2:1:1 structural arrangement (Figure 12). Isomorphic substitutions within the interlayer hydroxide sheet create a net positive charge that balances the negative charge arising from the 2:1 layers. A typical formula for the interlayer sheet is  $(\text{MgFeAl})(\text{OH})_2$ ; however, a variety of cation species may exist in these brucite that contribute to a large number of mineral species within this group. There is no water adsorption within the interlayer space; thus, chlorites are considered non expansive minerals

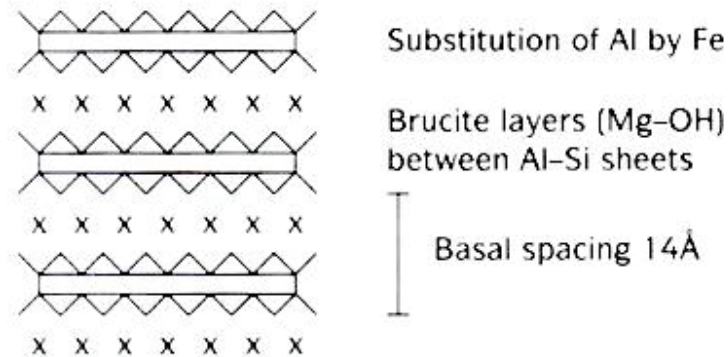
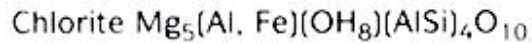


Figure 12: Structure of chlorite

#### *1.4.5.2 The diffusion properties of neutral, anionic and cationic radiotracers*

Radiotracer diffusion is one of key parameter considered for assessment of COX formation as migration barrier. We observed from the previous in situ diffusion tests a significant difference between anionic and cationic diffusion behavior. This difference could be explained by the anionic exclusion effect (Luc R. Van Loon, 2007) for anions and by the combined effect of ion exchange and surface complexation reactions with functional groups located on the clay surface for cations.

##### **Anionic exclusion effect for anions:**

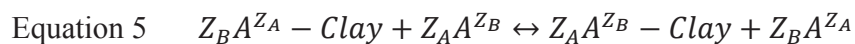
Normally, a mudstone milieu can be identified as charged porous milieu that exhibit strong anion exclusion effects (Luc R. Van Loon, 2007). From the sign of the charge of injection radionuclide and the surface charge of the clay, various electrostatic interactions occur which influence both the sorption and the fraction of space of the

porous medium. Generally, in most of conditions, the surface of Clay minerals is negatively charged. As a consequence, anions such as  $^{36}\text{Cl}^-$  and  $^{125}\text{I}^-$ , are repelled by the negative surface of the clay minerals and are therefore confined into "channels" narrower than those accessible to cations and neutral species (P.De Cannière, 1996).

### **Ion exchange and surface complexation reactions for cations:**

**Ion exchange** in these minerals is a reversible chemical reaction that takes place between ions (A) of valency  $Z_A$  held near a mineral surface by unbalanced electrical charges ( $Z_B$ ) within the mineral framework and ions (B) of valency  $Z_B$  in a solution in contact with the mineral (Equation 5). Generally the excess charge on the mineral is negative, and it attracts cations from the solution to neutralize this charge.

The chemical reactions in ion exchange follow the law of mass action, but the reactions are restricted by the number of exchange sites on the mineral and by the strength of the bonding of the exchangeable cations to the mineral surface (Michael H. Bradbury, 2005).



If a surface functional group reacts with an ion to form a stable molecular unit, a surface complex is said to exist and the formation reaction is termed **surface complexation**. Figure 13 illustrates the structure of the surface complex formed between  $\text{Na}^+$  and a surface site on the siloxane surface of montmorillonite. **The  $\text{Na}^+$  tends to be attracted on the siloxane surface near negative charge sites.** The way in which this negative charge is distributed on the siloxane surface is not well-known (Sposito, 2008).

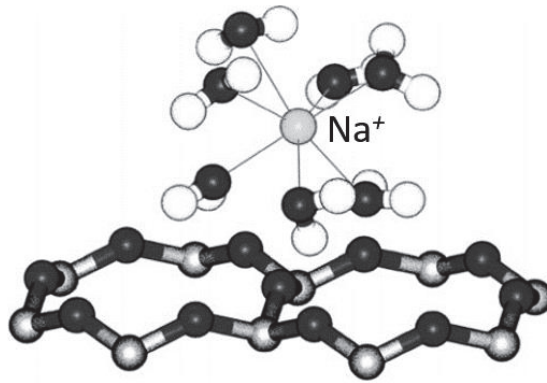


Figure 13: A surface complex formed between  $\text{Na}^+$  and a charged surface site on montmorillonite

**Neutral species (HTO) as a reference:**

Neutral species such as HTO is considered as non-reactive tracer that was measured in previous in situ measurements. HTO was commonly identified as a relative reference activity compared to anionic and cationic species in various in situ diffusion researches (Wersin, 2008) (Yi, 2012) (Gimmi, 2014) .

In summary, in argillite milieu, the surface of Clay minerals is negatively charged. As a consequence, cations can be retained in interlayer of clay minerals and anions are repulsed from surface (Figure 14) (F. Goutelard, 2007). Ions exchange and surface complexion favorite cations adsorption as well.

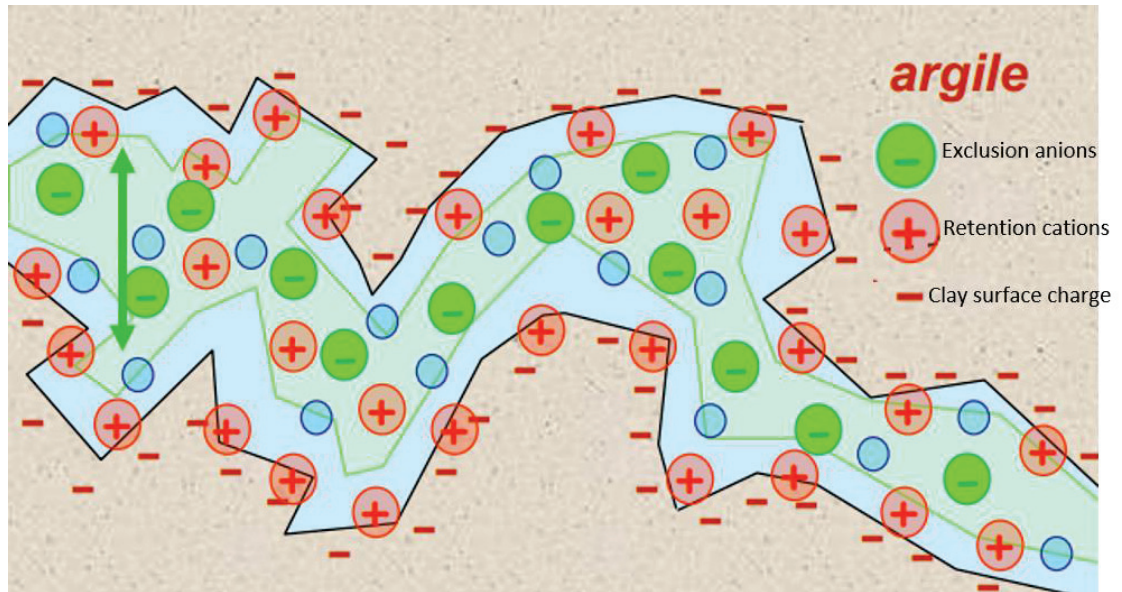


Figure 14: Inside view of surface charge and interlayer for clay mineral (COX)

(F. Goutelard, 2007)

### *1.4.5.3 The mobility of radioactive substance and candidate tracer for non-mobility radionuclide*

Nevertheless, a vast number of radionuclides produced by nuclear application exists. First of all, we have divided radionuclides into three types related to their mobility in clay medium.

#### **Medium mobility species:**

Cations ( $^{22}\text{Na}^+$ ,  $^{134}\text{Cs}^+$ ,  $^{85}\text{Sr}^{2+}$  and  $\text{Co}^{2+}$ ) due to various possible mechanisms interact (Cationic attraction, surface complexation, ion exchange) with clay minerals, and can be retarded or retained in argillite.

#### **Mobile species:**

The mobile radionuclides are principally neutral species such as tritiated water (HTO), or anions such as ( $^{125}\text{I}$  and  $\text{Br}$ ,  $^{36}\text{Cl}$ : section 1.3 table 2) due to relatively simple or no interactions with the argillite.

#### **Almost non mobility radionuclides:**

High level waste (HLW) are mainly composed of actinides family such as thorium, protactinium, uranium, neptunium, plutonium and americium that are radioactive, long-lived and highly toxic. In clay environment, the first barrier to actinides confinement is their solubility in solution. Once an actinide has dissolved in water or solution, its sorption onto the surrounding rock or mineral surfaces is expected to act as a barrier. When the actinide concentrations are far below the solubility limits, rock interfacial processes are expected to dominate actinide transport through the environment. The sorption distribution coefficient  $K_d$ , identified as the moles of radionuclide per gram of solid phase divided by the moles of radionuclide per milliliter of solution are reported as milliliters per gram (mL/g). It is studied that different mechanisms such as physical adsorption, ion exchange, chemisorption, surface precipitation favorite the retention of actinides on clay surface (Runde, 2000).

#### **Argument in the selection of radionuclides species depending on mobility:**

In previous in situ diffusion studies (DIR), mobile (anionic) and medium-mobile (cationic) radionuclides had been selected for in situ tests (Table 2).

The radionuclide  $^{22}\text{Na}$  is measured as the quickest cationic radionuclide diffusion in the host rock (M. García-Gutiérrez, 2009).  $^{22}\text{Na}$  decay schema is showed in Figure 15:  $^{22}\text{Na}$  disintegrates to the **1275 keV** level of Ne-22 via electron capture (9.64%) and beta plus (90.3%) process (Gamma emission @**511KeV**: section 1.4.3) with a half-life of 2.6029 years; only a very small fraction (0.056% for beta plus and 0.00098% for electron capture) disintegrate to the ground state of Ne-22 (Nucléide-Lara, s.d.).

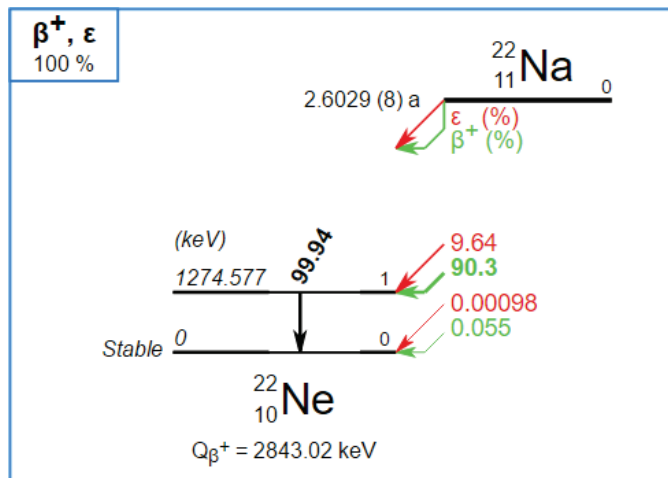


Figure 15: Decay scheme for  $^{22}\text{Na}$

For anion, isotope  $^{36}\text{Cl}$  is characterized and selected. It is one of interest in the case of impact assessment studies of nuclear disposal due to its very high mobility and long half-life (C.Fréchou, 2004). It is characterized through beta radiation (Figure 16): Cl-36 disintegrate by 98.1% beta minus decay to the ground state of Ar-36 with a half-life of  $302 \cdot 10^3$  years and beta emission of **709.55KeV** (Nucléide-Lara, s.d.).

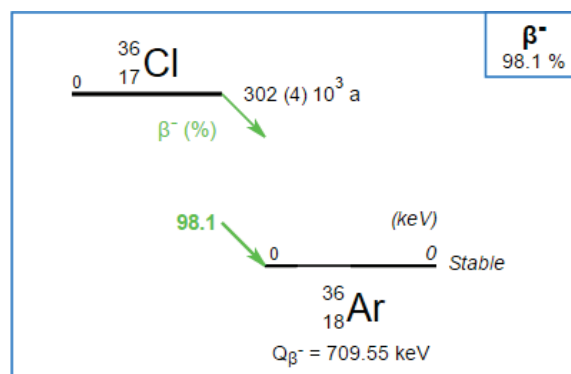


Figure 16: Decay schema for  $^{36}\text{Cl}$

Although representative mobile and non-mobile radionuclides have been characterized and selected, up to now our question focus on the selection of almost non-

mobile radionuclides, various candidates were possible. But some are limited as listed in the table below (Table 5):

Candidate	Difficulties	Complement
$^{233}\text{U}$	Nuclear raw material	Authorization requirement
$^{235}\text{U}$	Nuclear raw material	Authorization requirement
$^{234}\text{U}$	Low intensity (I<1%)	Impossible to be detected
$^{238}\text{U}$	Possible	No test for sensor
$^{234}\text{Th}$	Nuclear raw material	Authorization requirement
$^{232}\text{Th}$	Low intensity (I=0.19%)	Impossible to be detected
$^{241}\text{Am}$	Possible	Tested to be detected by sensors
$^{243}\text{Am}$	Possible	No test for sensor
$^{241}\text{Pu}$	Nuclear raw material	Authorization requirement

Table 5: Lists of actinide candidates and arguments for radionuclide injection in situ diffusion test

To summary, the criteria in the selection of radionuclides principally based on sensor detection possibility related on radionuclide decay intensity emission, origin of radionuclides (Nuclear raw material), and chemical and physical properties of radionuclides interaction with clay minerals (adsorption on clay surface). 3 candidates seem to be possible to be injected. For isotope Am, sensors had been validated to detect low gamma energy at around 60KeV (Nucléide-Lara, s.d.). No further sensor test had been done for detection of  $^{238}\text{U}$ . For the moment, Am is selected for the further new in situ diffusion test as representative of non-mobile nuclear waste radionuclide.

#### **New in situ diffusion test (DRN) overview:**

As mentioned just now, candidate radiotracers have been selected for new in situ diffusion test: Am,  $^{22}\text{Na}$  and  $^{36}\text{Cl}$  with respective test name: DRN1204, DRN1202 and DRN1203 (Table 6 and Figure 17). In NED gallery, the research methods consists on:

- (i) Injection of a quantity and one type of radio tracers solution mixed with neutral species HTO (Tritiated water) in circulation (Dewonck. S, 2007)
- (ii) Measurements of radionuclides diffusion after a fixed delay by a series of sensors located in peripheral boreholes. Here, we would like to point out that HTO is an inert tracer (no adsorption) and will be used as a reference.

Trial	Gallery / drilling	Cocktail mixture	Observations
DRN1202	NED / horizontal	HTO, $^{22}\text{Na}$	Observation the circulation of solution in injection drilling + $\gamma$ detection around injection drilling
DRN1203	NED / horizontal	HTO, $^{36}\text{Cl}$	Observation the circulation of solution in injection drilling + mini $\beta$ detection around injection drilling
DRN1204	NED / vertical	An actinide	$\gamma$ detection around injection drilling

Table 6: Principal tests in NED gallery

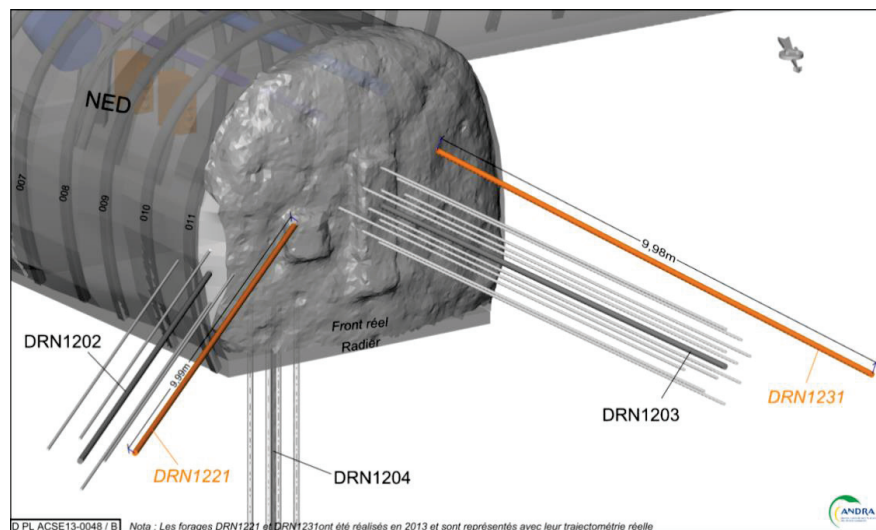


Figure 17: General scheme of implementation of DRN test drilling NED

(Vinsot, 2015)

## 1.5 Conclusion

In France, by 2011 there were 58 nuclear reactors electronuclear reactors (run by EDF, the French utility). Spent nuclear fuel contains a wide range of radionuclides; activation products originating from neutron capture by metals in the fuel, fission products from the cleaved nuclei and actinides originating from neutron capture by uranium. Some types (ILW-LL, HLW) of nuclear waste require deep disposal in long term. In France, an underground research laboratory (URL) has been built by Andra to investigate the feasibility of radioactive waste disposal facility at a depth of 490 m within the Callovian-Oxfordian (COX) mudstone. Our interests are mainly focus on the investigation and quantification of the radionuclide diffused through the Callovian-Oxfordian rock in situ. In the first in situ experiment HTO,  $^{22}\text{Na}$ ,  $^{36}\text{Cl}$ ,  $^{125}\text{I}$ ,  $^{85}\text{Sr}$  and  $^{134}\text{Cs}$  were used as tracers and as chemical and physical analog to different radionuclides in the waste. A circulation pump is maintaining a homogeneous concentration of the tracers in the interval. Tracer contents in the circulation fluid are regularly measured by water sampling and analyzing. The tracers 'concentrations in injection chamber decrease with time due to the diffusion into the rock. The monitoring of these concentration gives an information about the different behaviors of the tracers, as expected in theory a large decrease of cationic radionuclide due to their retention on the rock surfaces, and a slower decrease of anionic radionuclides compared to tritiated water due to anionic exclusion. Based on the previous in situ diffusion test (DIR), a new in situ diffusion test (DRN: Diffusion RadioNuclides) had been studied consists of monitoring at a long time scale (3 to 8 years) and at a metric scale (50 cm) in situ. DRN experiments response to the requirement of using compact sensors located in peripheral boreholes. Up to now,  $^{22}\text{Na}$  and  $^{36}\text{Cl}$  have been considered as representative cationic and anionic radiotracer to be injected, because of their relative mobility. Non-mobile candidate is always under study, for moment, Am seems to be the candidate for its half-life, detection possibility and authorization aspect.

# CHAPTER 2 General methods, theory and technical aspects

## 2.1 Introduction:

In this chapter we will introduce different stages related to radiation measurements. As illustrated in Figure 18, in a whole, when radiation is absorbed in a scintillator, it will create photons and then convert into electric signal through photo sensor. After that this low-level signal pass through a set of analog processing (preamplifier, amplifier and pulse shaping), and then selected and digitized for subsequent storage and analysis and interfaced with MCU.

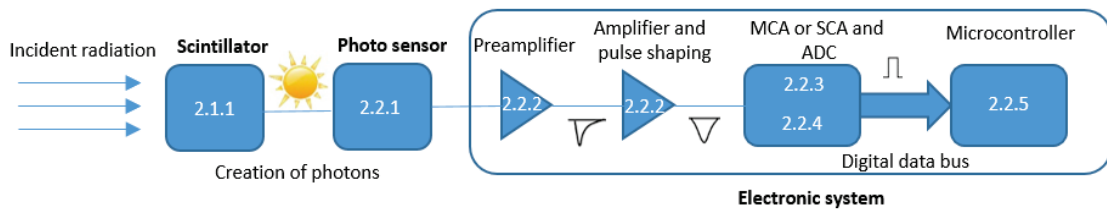


Figure 18: Overview of radiation detection process

First of all, a good selection of **scintillators** for the detection of different energy radiations could provide a optimize measurement. The criteria in the selection of different scintillator will be introduced in this chapter.

Although diverse **photo sensors** existed, each has its advantages and drawbacks. In this chapter, we will analyses the functionalities and limits of various photo sensors such as PMT, Pin diode, APD, SiPM.

**Electronic** plays an important role in radiation detection system. It can be almost considered as the last stage of radiation detection system. An electronic system includes electronic readout, optimization of signal to noise ratio, digital signal processing and communication.

Apart from radiation measurement system, another important tool in radiation research is the use of **MCNP code**. It simulates the transport of radiation particles that allow us to estimate the detection efficiency, detection signal response related on different tracers distribution versus time and help to radiation sensor design.

## 2.2 The technology behind sensors

### 2.2.1 Principles of the scintillator detection

Among various radiation detection technologies that exist, our work only focus on the use of scintillation detection technologies. The scintillation process could be summarized as following: when atoms of incident ionizing radiation interacts with atoms of these so called scintillation materials, they transfer some of their energy to the atoms. As a result these excited atoms go into short lived excited states. When they return to ground state they emit photons, mostly in visible and ultraviolet regions of the spectrum (Figure 19).

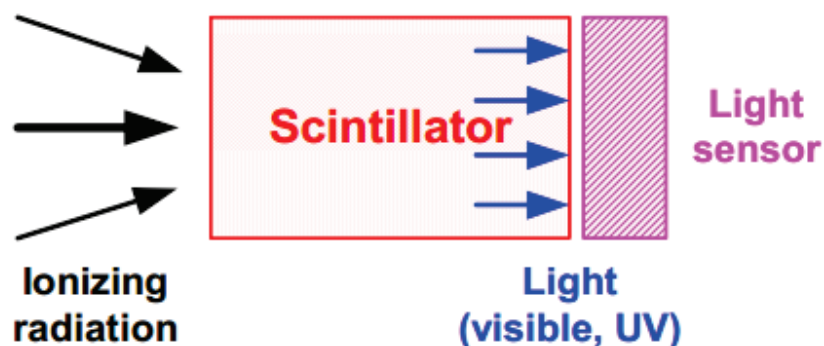


Figure 19: Working scheme for a scintillation detector

Although scintillation materials come in a lot of forms and types, in general, they can be divided into two categories: organic and inorganic. In this thesis we only worked with the inorganic scintillation materials. The inorganic scintillation mechanism depends on the structure of the crystal lattice. In a pure inorganic crystal lattice such as NaI, electrons are only allowed to occupy specific energy bands. The forbidden band (band gap) is the range of energies in which electrons can never be found in the pure crystal. In the pure crystal, absorption of energy can elevate electrons from the valence band to the conduction band leaving a gap in the valence band (Figure 20a: left part). However, the return of an electron to the valence band with the emission of a photon is an inefficient process. Furthermore, typical gap widths in pure crystals are such that the resulting emitted photon would be too high to lie within the visible range (Byun, chapter 4).

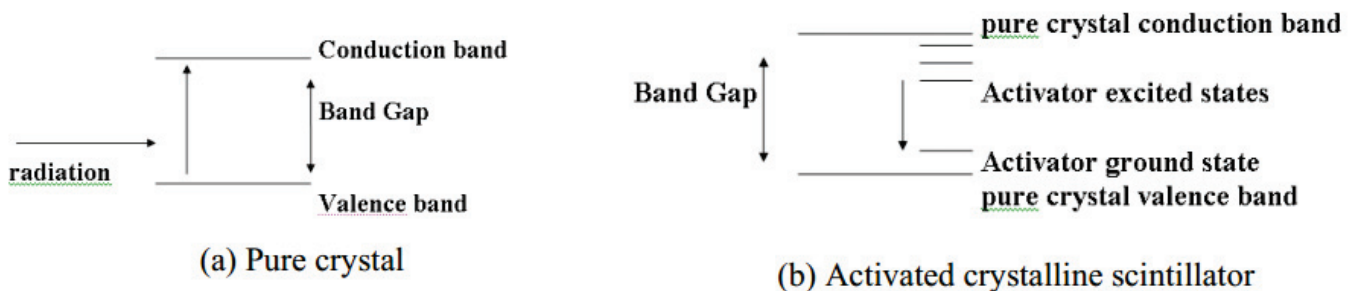


Figure 20: Energy band structure in an inorganic scintillator

To enhance the probability of visible photon emission during the de-excitation process, small amounts of an impurity are commonly added to inorganic scintillators. Such deliberately added impurities, called activators, create special sites in the lattice at which the normal energy band structure is modified from that of the pure crystal (Figure 20b: right part). As a result, the electron can de-excite through these levels back to the valence band. The energy levels created by the activator's presence within the crystal are narrower than in the pure crystal. The photons emitted by the transitions of electrons

from upper to lower states will be lower in energy than in the pure crystal. Thus the wavelength emission spectrum is shifted to longer wavelengths (Figure 21), and the photons are emitted in the visible range.

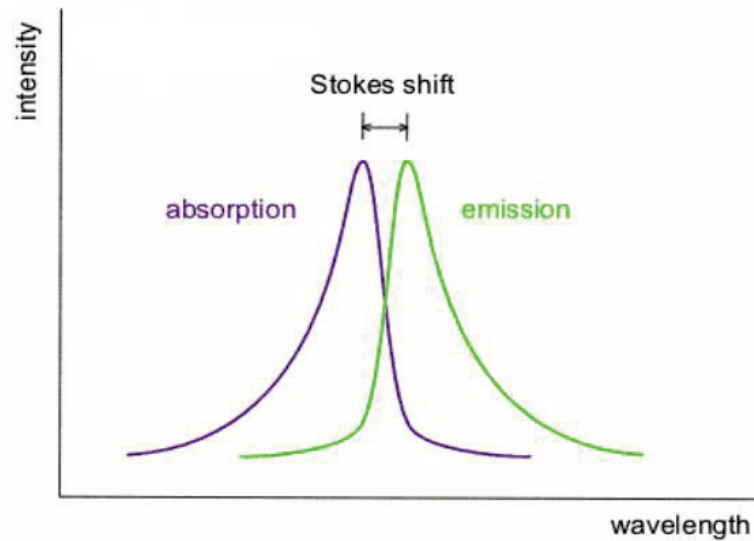


Figure 21: Wavelength stokes shift

### 2.2.2 The criteria for the selection of scintillators

Some commercial inorganic scintillators were listed in Table 7. It summarized the most attractive aspects for detector developers in selection of most effective scintillator related to different applications.

	<b>Density (g/cm<sup>3</sup>)</b>	<b>Light Yield (ph/MeV)</b>	<b>Decay (ns)</b>	<b>Energy resolution (%)</b>	<b>Attenuation coefficient for 662KeV (mm)</b>
<b>NaI(Tl)</b>	3.7	40000	230	6.5	29
<b>BGO</b>	7.1	8000	300	9	11
<b>YSO</b>	4.44	25000	70	12	25

<b>LSO</b>	7.4	32000	41	8	11.2
<b>LaBr<sub>3</sub></b>	5.08	63000	16	2.8-4	>10cm
<b>LaCl<sub>3</sub></b>	3.9	50000	20	3.2	similar to NaI

Table 7: Density, light yield and decay time of some commonly used inorganic scintillators

Crystal NaI(Tl) is the well-known standard scintillator. Crystal BGO, is a standard solution to make small and compact detectors available to detect all gamma-ray range (above 100 keV, up to several MeV) because of a good stopping power (11mm) and high density without any internal radiation background. As a result, for our project, **BGO (1 inch) was selected to detect the diffusion of radiotracer <sup>22</sup>Na in situ.** Nevertheless, BGO crystal is limited for high count rate due to its slow decay time (300ns).

In case of detecting very low energy gamma and beta particles, the 1 inch BGO scintillator may be replaced by an YSO scintillator. It is used to detect the gamma emissions at low energy between 40 and 200 KeV with a high light yield and shorter decay time available to detect more counts per second. Thus **YSO is validated for the construction of <sup>241</sup>Am and <sup>36</sup>Cl monitoring system in situ.**

Lutetium (Lu) based scintillators such as LSO and LYSO, are widely used in modern PET detectors due to their high stopping power for 511 keV gamma rays, high light yield and short decay time. However, 2.6% of naturally occurring Lu is <sup>176</sup>Lu, a long-lived radioactive element including a beta decay and three major simultaneous gamma decays. This phenomenon introduces random events that affects the system performance. It has been calculated that the intrinsic emission of a milliliter scintillator could achieve at 307Bq/ml (Wei, 2014).

In the last years, the Lanthanum Halide scintillators ( $\text{LaBr}_3$  and  $\text{LaCl}_3$ ) are attracting the scientific community in nuclear spectroscopy because of their ‘almost ideal’ scintillation properties expected to an alternative to HpGe detector. Studies have shown that  $\text{LaBr}_3:\text{Ce}$  material gives optimal energy resolution for scintillators ( $<3\%$  at 662 keV), an excellent time resolution ( $\approx 300$  ps), good efficiency and a negligible variation of light output within temperature range  $-20: +60$  °C (F.C.L. Crespi F. N., 2009). Although many interests of using Lanthanum Halide scintillators, they are limited to relatively high intrinsic radiation background due to naturally occurring  $^{138}\text{La}$  and  $^{227}\text{Ac}$  radioisotopes. A good use of this kind of crystal needs an accurate determination of the self-activity, particularly when low background is required. It is investigated that for a 3x3 inches  $\text{LaBr}_3$ , The rate of all the crystal self-activity was measured to be around 320 cts/s in the energy range from 50 keV up (A. Lavagno, 2012). In order to avoid the internal background perturbation, typically in the very low count situation as we will be, we do not adapt Lanthanum Halide scintillator.

### 2.2.3 Photon sensors

We knew from previous section that the essential role of the scintillator is to convert radiation (gamma or beta particle) into a large number of low energy photons (visible light), and this number of visible light are proportional to the radiation energy absorbed in scintillator. To quantify this quantity, photon sensors are used to convert light photons into a very large number of electrons formed electronic signals. In this paragraph, we will introduce three types of photon sensors: photomultiplier, photo diode and SiPM.

#### 2.2.3.1 *Photomultiplier (PMT)*

The basic building blocks of a complete PMT are a photocathode, an electron multiplication structure, and a readout electrode (Figure 22). At first, the incident photons strike on the photocathode, then get converted into electrons through the process of photoelectric effect. The electron is then made to accelerate and collide a metallic

structure called dynode, which results in the emission of more electrons. The newly produced electrons are again accelerated towards another dynode, where even more electrons are produced. This process of electron multiplication continues until the electrons reach the last dynode where the resulting current is measured by some electronic device.

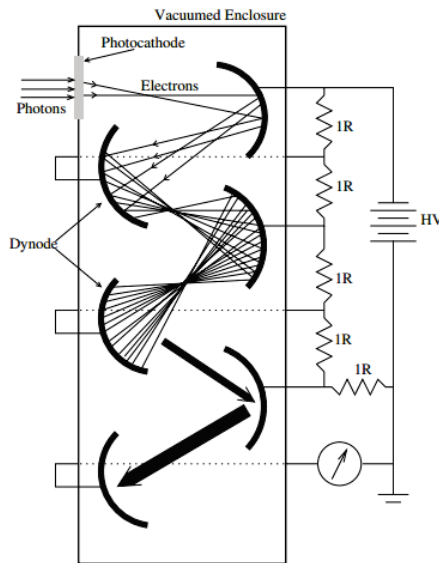


Figure 22: Working principle for a typical PMT

PMT is generally the most used as standard photon sensors, it presents:

- High sensitivity
- Good signal to noise ratio
- Fast time response
- Large photosensitive area

### 2.2.3.2 *Photo diode*

**PN diode**

A traditional photodiode is a semiconductor device that can convert visible light into current. It consists of a p-n junction working in reverse biased mode.

When a photon with sufficient energy (i.e. higher than the band gap of 1.12 eV that corresponds to a wavelength shorter than 1100 nm) strikes the photodiode, it is absorbed and it create a mobile electron and a positively charged electron hole. Such electron-hole pair creation occurs throughout the p-layer, depletion layer or n-layer material as a function of the photons wavelength: short wavelength photons are absorbed in the p-type layer whereas the long wavelength photons are absorbed in the n-type layer. When the photo-carrier generation is created in the depletion region, where the electron and hole quickly drift in opposite directions because of presence of the electric field in this region. Since recombination does not take place in the depletion region, each photo-carrier adds a charge  $q$  (considering generation rate of 1) to the current collected to the device electrodes. The collection of the created charges gives rise to the “photocurrent” which is proportional to the intensity of the incident light (Dinu, 2013). Nevertheless, PN diode is limited to detect low radioactive activity due to its low gain.

### **Avalanche photodiode (APD)**

The mainly difference between PN diode and avalanche photodiodes is due to the reverse bias value. Applying a higher electric field (in Geiger mode) allows each photo-generated carrier to be multiplied by avalanche breakdown, resulting in internal gain within the photodiode, which increases the effective responsivity of the device. To be detailed, an electron colliding with a bound valence electron transfers enough energy to the electron to ionize it. This creates an additional electron-hole pair producing current gain. The additional carriers, in turn, can gain sufficient energy from the electric field to cause further impact ionization, creating an avalanche of carriers (Figure 23). Although single-pixel Geiger mode devices (Avalanche Photo Diodes—APDs) were developed in the mid-sixties, this technology gradually evolved by creating a large array of parallel connected APDS, called SiPM (Barral, 2004).

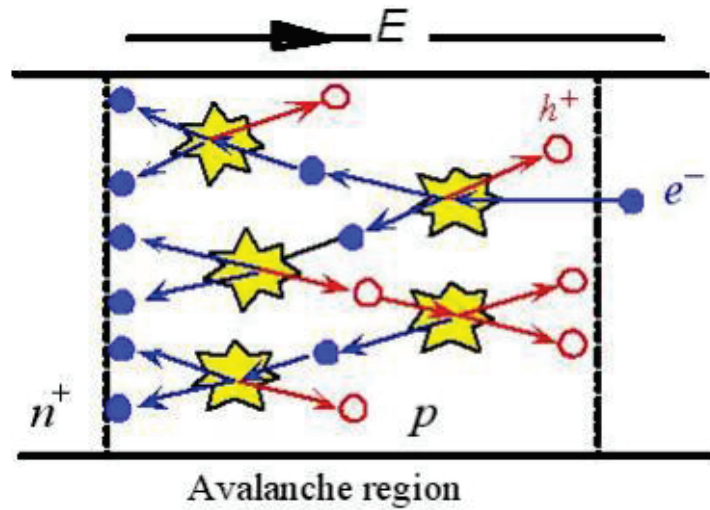


Figure 23: Geiger mode avalanche photodiodes

### 2.2.3.3 Silicon PhotoMultiplier (SiPM)

Silicon photomultiplier (SiPM) has been considered as the promising and candidate device to replace the vacuum photomultiplier tube (PMT) in a number of scintillation detection. It consists of various advantages as follows (AXINT, 2007):

- **Competitive to photomultipliers' one:**

With a quantum efficiency of about 20 % and a gain of about  $10^6$ , the SiPM detection characteristics allows us to compete with the classical photomultipliers of the market. In addition, the SiPM are cheaper and have a stable and reliable performance on the long term than PMT.

- **An insensitivity to the magnetic fields.**

The SiPM are the only photodetectors able to make measurements in strong magnetic fields. For exemple, SiPM can be measured in a field of more than 5 Tesla.

- **A low supply voltage**

The SiPM require only a supply voltage of 30-70 Volts to operate. This kind of sensors allows to suppress the expensive and bulky high voltage power supplies needed by the photomultipliers.

- **Compact dimensions**

Supposed that the active surfaces between PMT and SiPM are the same, PMT would be much larger than the APD or SiPM: more than 10 centimeters long for a PM whereas a SiPM have a thickness of only a few millimeters. Therefore, SiPM is more adapted in situ monitoring condition that a compact dimensions is required.

A SiPM (Figure 24: right part) is composed of hundreds of photodetector cells (Geiger-mode APD) of a very small size (between 20 and 100 micrometers per side). Each cell reacts binary: either it is at rest, or it captures a photon and emits a fixed amount of electricity. Each SiPM is a matrix consisting of thousands of these Geiger-mode APDs (Figure 24: left part). The signal from each SiPM is obtained by adding the signals of all the cells. Thus, one can obtain a measure of the analog quantity of light detected by a SiPM, which can range from one single detected photon to more than 10 000. SiPM is our selection of photo sensors in sensor fabrications for its performance of high gain, high photon detection efficiency, insensitivity to magnetic field, and low voltage supply.

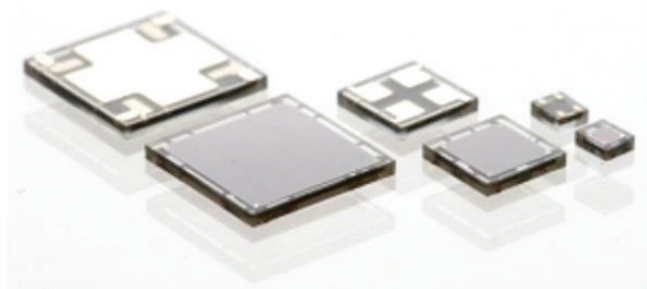
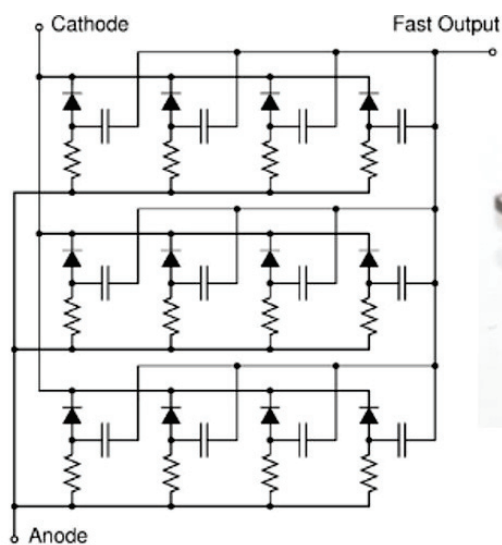


Figure 24: Sensl Silicon photomultiplier schema and sensl C-series product view

Although SiPM has various advantages, the use of SiPM is limited by its small active area. Only devices with an active area of  $6 \times 6 \text{ mm}^2$  are now widely available. The reason is due to parallel connection among the APDs to increase the sensitive area. This cause 2 effects: firstly, the characteristic dark count noise increase with the active area; secondly, the recovery time increases with the increasing capacitance of the APDs. To solve these limits, Paolo W. Cattaneo works reported that increasing on the active area size up to  $120 \times 40 \times 5 \text{ mm}^3$  with series connections of multiple SiPM gives a better time resolution (Figure 25) (Paolo W, 2014). This solution have been verified by us with 2 SiPM in series for another cooperation in the field of radio-pharmaceuticals quality control, while it was not yet involved in situ monitoring system due to the time limit for our preparations. It will be integrated in the next sensors generation.

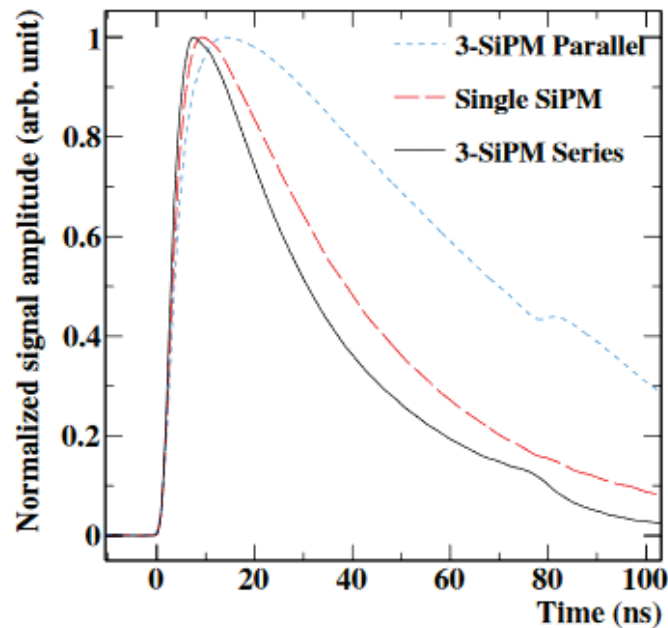


Figure 25: Pulses shape comparison for various SiPM connections

## 2.2.4 Electronic signal processing

Signal processing plays an extremely important role in extracting useful information from detectors. Generally, the detection and measurement of radiation involve 2 important aspects: the amplitude and the timing of the output pulse. The first one is related to an estimation of energy deposited by the incoming radiation, the second one for the particle tracking. The extraction of information from the narrow width and low amplitude sensor pulses, requires a number of analog and digital signal processing (DSP) steps. Firstly, for amplifying the signal and then convert to a digital value using analog to digital converters (ADC) module.

### 2.2.4.1 Preamplification

The detector output signal collected from PMT, PIN diode or SiPM required a preamplification. Usually the pulse has a very low amplitude and very short duration, making the direct measurements of amplitude and time complicated. This step not only amplifies the pulse but also increases its width for any further processing on electronic circuit. In general, the preamplifiers used in radiation detection systems are chosen from the following categories:

- 1. Voltage Sensitive Preamplifier;**
- 2. Current Sensitive Preamplifier;**
- 3. Charge Sensitive Preamplifier;**

The voltage sensitive Preamplifier is the most basic type of preamplifier, it amplify the potential at the input stage by some gain factor depending on the detector capacitance. Meanwhile, the detectors' capacitance may change during operation due to small fluctuation in temperature and then introduced some environmental noise. Hence, voltage sensitive amplifiers are not always preferred over other types of amplifiers. Current sensitive amplifier is used to measure the instantaneous current flowing through the detector, converting the detector's instantaneous current through a measurable voltage. To fulfill the design of current sensitive amplifier, the preamplifier's input

impedance should very small compared to source impedance, whereas it is usual not the case for the preamplifier.

As stated in previous paragraph, both of voltage and current sensitive preamplifier present its drawbacks. The charge sensitive preamplifier seems to be the mostly suitable for integration in radiation detection system, and designed to make the charge accumulated on the detector capacitance to another integrator capacitor called  $C_f$ , as showed in Figure 26. The resulting potential ( $V_{out}$ ) on capacitor is proportional to the original charge on the detector. One disadvantage as showed in Figure 27 is on the absence of discharge on the plateau of output voltage after reaching the maximum value. (Tension en fonction de charge)

$$V_{out} \propto \frac{Q_d}{C_f}$$

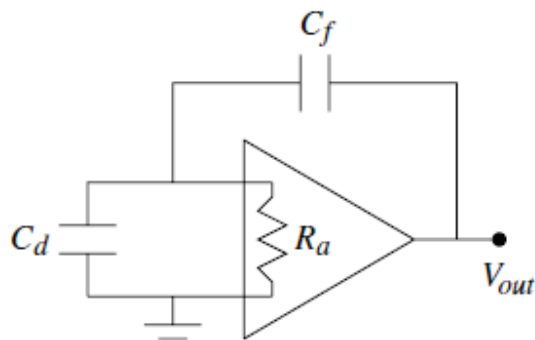


Figure 26: Basic principle of a charge sensitive preamplifier

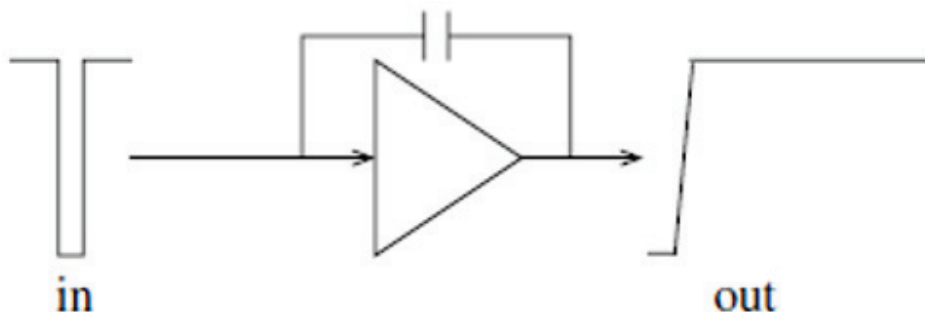


Figure 27: Output voltage pulse shapes view for a simple charge sensitive preamplifier

The discharge functionality is done with a feedback resistor, coupled with a feedback capacitor ( $R_f C_f$ ) (Figure 28). The high voltage (HV) bias of detector is fed through the preamp in general. A coupling capacitor ( $C_c$ ) should be provided between the detector and preamp circuits in ac-coupled configuration, while it is eliminated if the dc-coupled configuration is used. The discharge functionality follows an exponential decay related to R and C (Figure 29).

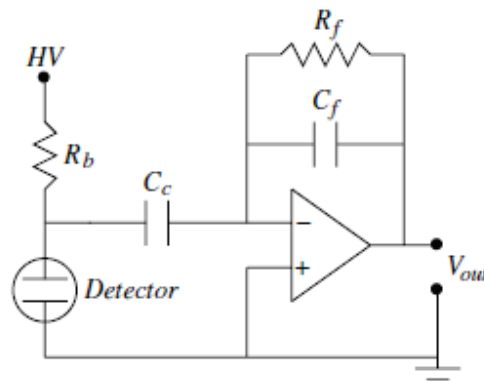


Figure 28: Schema of an AC coupled resistive feedback charge sensitive preamplifier

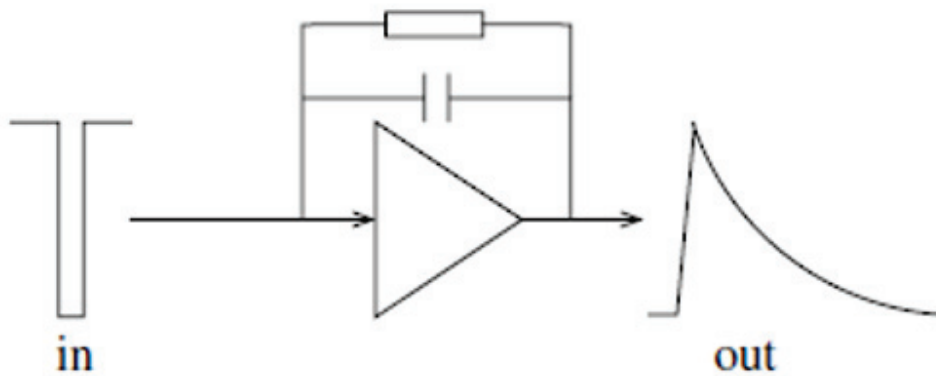


Figure 29: Output voltage pulse shapes view for a resistive feedback charge sensitive preamplifier

### 2.2.4.2 Pulse shaping

The raw signal coming out from the detector is usually very narrow and therefore not easy for extracting information such as the amplitude of the pulse (Figure 30). This narrow signal must be firstly shaped into a broader pulse with a rounded maximum before further treatment.

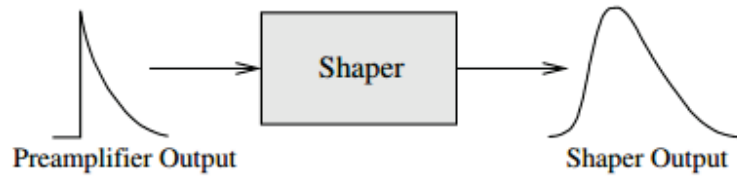


Figure 30: Functionality of shaper system

The simplest concept for pulse shaping is the use of a CR circuit followed by an RC circuit. In this shaping, the preamp signal first passes through a CR shaper and then RC shaper. This CR-RC circuit diagrams (Figure 31: top part) give rise to an output pulse (Figure 31: bottom part) shape. For circuit analysis, the Laplace and Fourier transformations are essential and the results are demonstrated as Equation 6 (Abmed, 2007):

$$\text{Equation 6: } V_{out} = \frac{t}{\tau} e^{-\frac{t}{\tau}} (\tau_i = \tau_d = \tau)$$

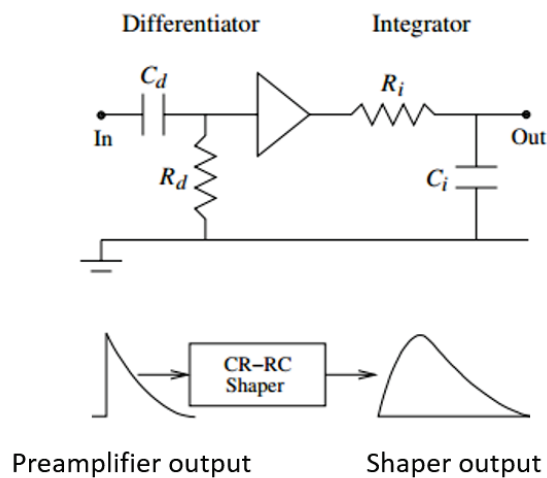


Figure 31: Simple CR-RC shaper schema and its response to preamplifier output

### 2.2.4.3 General view of AXINT analog electronic design

In this paragraph, we will introduce our own conception of electronic design suitable for detection of radiations of Gamma or beta sources as showed in the following figures (Figure 32, Figure 33 , and Figure 34 ). It is designed based on the two precedent design points (Charge sensitive preamplifier and CR-RC shaper). It begins with a SiPM output pulses (Figure 32: Marked with SiPM 02). These small output signals are then integrated into charges that is in proportional to the photon's energy by charge sensitive circuit (Figure 32: left part) and shaped via CR filter (Figure 32: right part). After that, the signals had to be amplified (Figure 33) and pass through peak detector prepared to be digitalized (Figure 34), the RC shaper is included in the peak detector circuit (Figure 34). The electric circuit considering footprints has been listed in ANNEX.

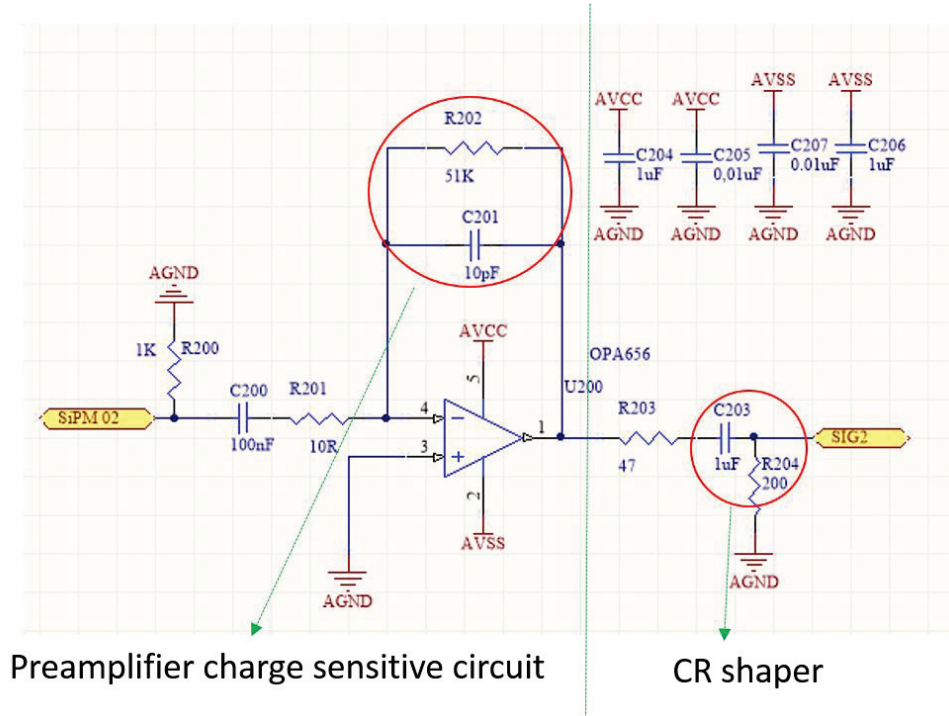


Figure 32: Schema of preamplifier circuit and CR shaper

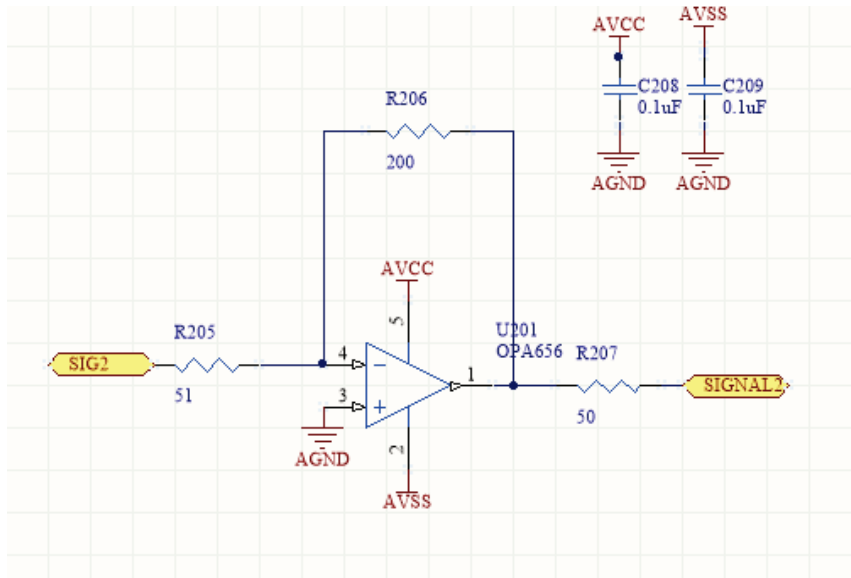


Figure 33: Schema of amplifier circuit

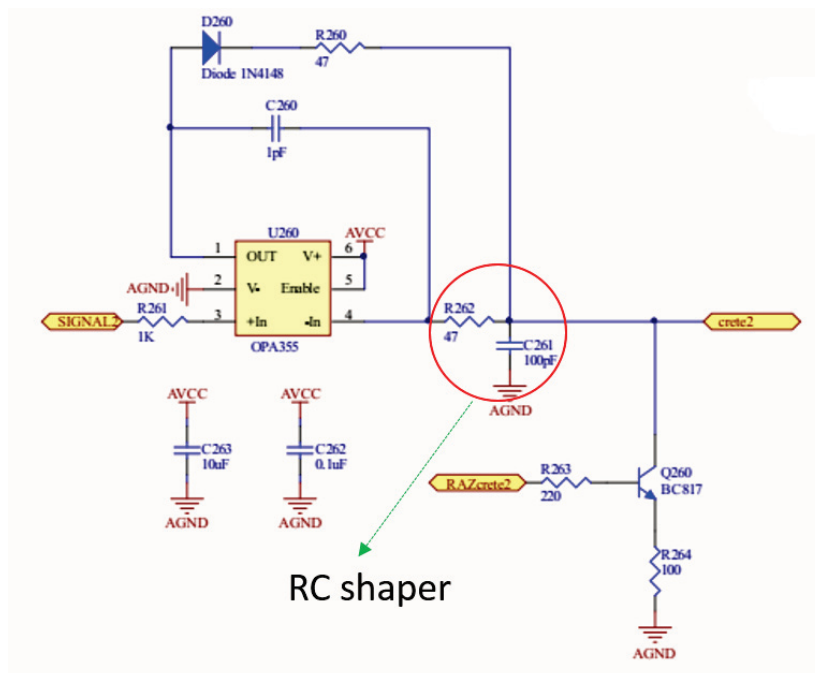


Figure 34: Schema of peak detector circuit

## 2.2.5 Discrimination

### ***Introduction:***

From analog output signal, it is often required to check whether the signal is above or below a predefined threshold. A discriminator module, which accepts an analog input and produces a digital output consists of a comparator circuitry between the input voltage to and the preset voltage that can be adjusted through a potentiometer. If the input pulse amplitude is higher than the preset threshold, the output logic level becomes active, otherwise it remains in its previous state. Figure 35 give an example of two-level discriminator that only pulses between the two preset thresholds ( $V_h$  and  $V_l$ ) are counted by a logic level high.

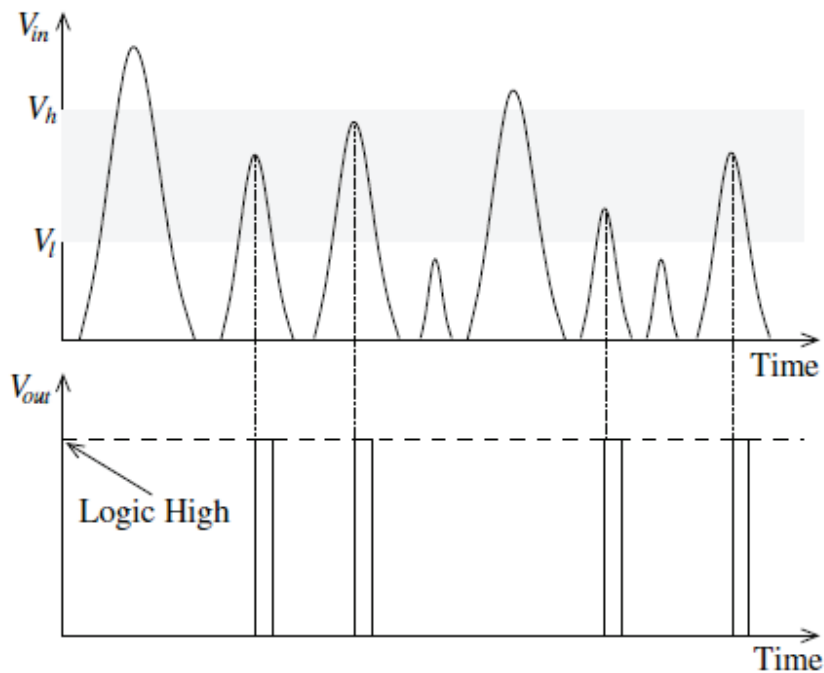


Figure 35: Pulse discrimination by a two-level discriminator

In most of radiation counting system, it is only required to count the number of interesting pulses. The definition of an interesting pulse depends normally on the characterized energy emission of radioactive source. Here LLD stand for lower level discriminator (Figure 36). It will consider all the pulses that have a pulse height superior to this lower level pulse height. After the pulse has been discriminated and a logical output high has been generated, it must count the number of logical output high.

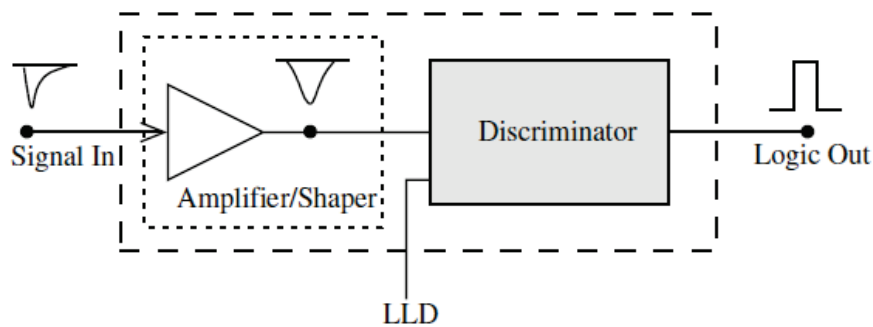
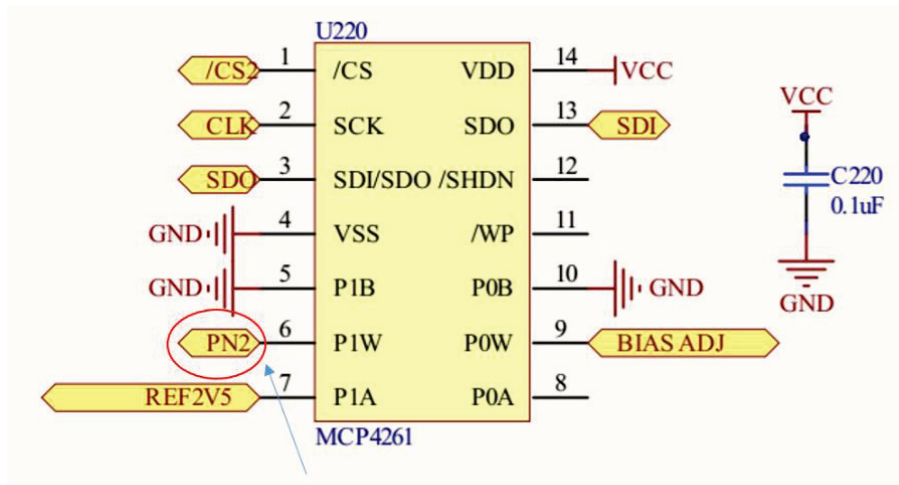


Figure 36: Block diagram for a simple single channel analyzer (SCA)

In AXINT detection electronic system, it is designed with only one preset voltage (the lower level discriminator: LLD) adjusted by a digital potentiometer (MCP4261) (Figure 37) using SPI interface (/CS2, CLK, SDI, SDO) communicates with microcontroller. The detail information about this digital potentiometer part is given by:

<http://ww1.microchip.com/downloads/en/DeviceDoc/22059b.pdf>



Controlled by digital potentiometer MCP4261

Figure 37: Electronic schema of a LLD system

Once the threshold voltage level (LLD) has been selected, it will pass through a comparator (Figure 38: bottom part, AD8612). The detection signals (Figure 38: bottom part, SIGNAL2) have to be compared with LLD (Figure 38: bottom part, PN2) to filter the pulses that inferior to LLD. Then the remaining pulses will go into monostable circuit part (Figure 38: top part, 74VHC221) to obtain a logic output (Figure 38: top part, MONO2). This logic output pulse width in seconds is determined by the equation:  $C298 \cdot R295$  (Figure 38: top part with R in Ohms and C in farads), and then passes into one pin of DSP (Digital Signal Processing) microcontroller using its rising edge functionality to construct a counting system.

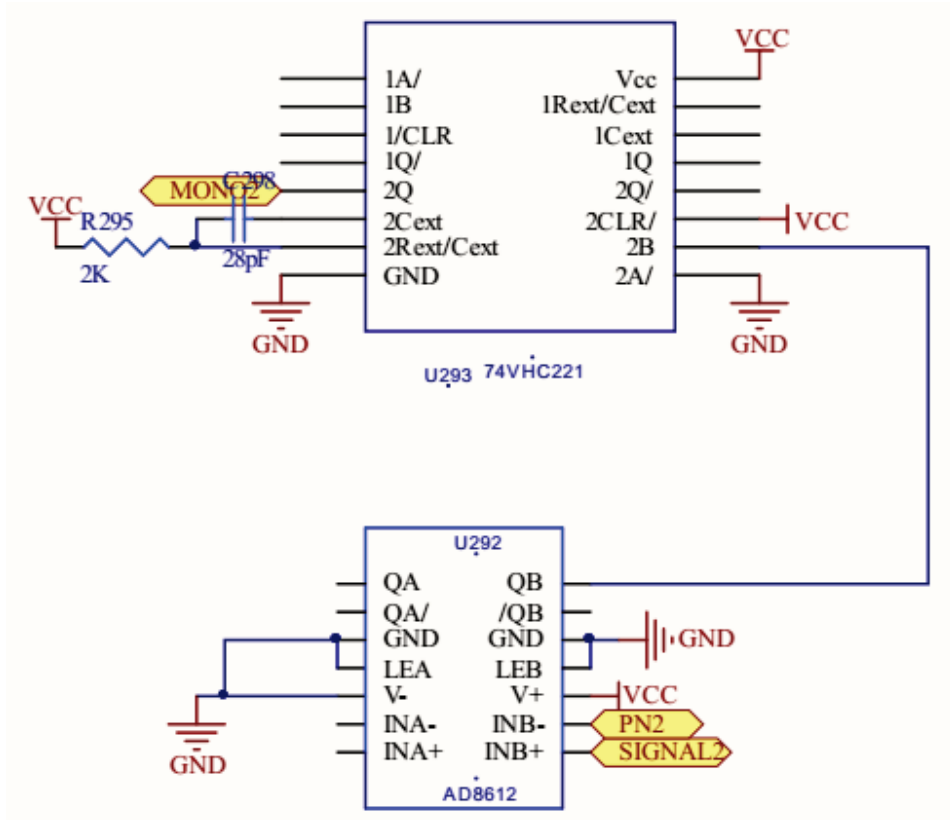


Figure 38: Electronic scheme of a comparator and of a monostable

The operation in selection of low level discriminator is essential to set the low preset voltage (discrimination threshold) superior to electronic and background noise threshold.

## 2.2.6 Analog to Digital Conversion (ADC) for multi-channel analyzer (MCA)

A peak sensing analog-to-digital converter (ADC) measures the height of an analog pulse and converts that value to a digital number. The digital output is a proportional representation of the analog pulse height at the ADC input. For sequentially

arriving pulses, the digital outputs from the ADC are fed to a dedicated memory, or a computer, and sorted into a histogram. This histogram represents the spectrum of input pulse heights. The dynamic range of the ADC operation is consistent with the range of the spectroscopy amplifier output, i.e. 0 ~ 2.5V. The AD7472 part (Figure 39) is in parallel output and within 12-bit high speed (1.5MSPS) conversion process. The analog input is 0 V to REF IN. The 2.5 V reference is applied externally to the REF IN pin. The conversion process and data acquisition are controlled using standard control inputs, allowing easy interfacing to DSPs (Detailed in the following digital signal processing part). The input signal is sampled on the falling edge of CONVST, and conversion is also initiated at this point. BUSY goes high at the start of conversion and goes low 531.66 ns after falling edge of CONVST to indicate that the conversion is complete. The conversion result is accessed via standard CS and RD signals over a high speed parallel interface. For further information attached to ADC part, please find the datasheet from [http://www.analog.com/media/en/technical-documentation/data-sheets/AD7470\\_7472.pdf](http://www.analog.com/media/en/technical-documentation/data-sheets/AD7470_7472.pdf)

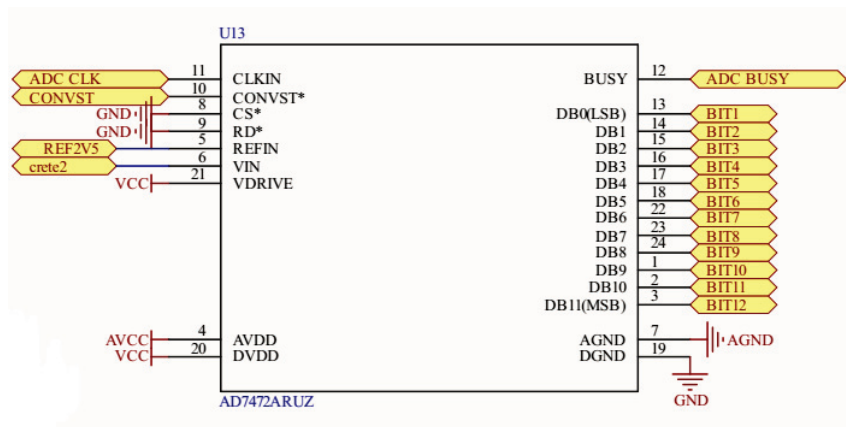


Figure 39: Representation of an ADC module

Here, we just extracted some essential information (PIN function) related to our applications from datasheet (Table 8).

<b>Pin</b>	<b>Function</b>
<b>CS and RD</b>	Chip Select and Read Input (CS and RD can be hardwired permanently low, in which case the data bus is always active)
<b>CONVST</b>	Conversion Start Input
<b>CLKIN</b>	Master Clock Input
<b>BUSY</b>	BUSY Output
<b>REFIN</b>	Reference Input
<b>AVDD</b>	Analog Supply Voltage
<b>DVDD</b>	Digital Supply Voltage
<b>AGND</b>	Analog Ground
<b>DGND</b>	Digital Ground
<b>VIN</b>	Analog Input
<b>VDRIVE</b>	Supply Voltage for the Output
<b>DB0-DB11</b>	Data Bit 0 to Data Bit 9

Table 8: Pin function descriptions

### ***Multi-Channel Analyzer (MCA)***

A multi-channel analyzer (MCA) can be thought as a modified version of single channel analyzer introduced before where each input signal is digitized by an ADC module and stored in memory. Compared to SCA mode, MCA eliminate the limits of count pulses at only one threshold window. Figure 40 shows a simple block diagram of a multi-channel analyzer. First of all, the analog detector pulse is t amplified and shaped. The height of the amplified pulse is then digitized. After digitization, a count in the corresponding memory bin is incremented. Thus the results can display the number of counts vs. channel number (Figure 41) and is equivalent to a histogram of the number of counts vs. pulse height, i.e. a pulse height spectrum.

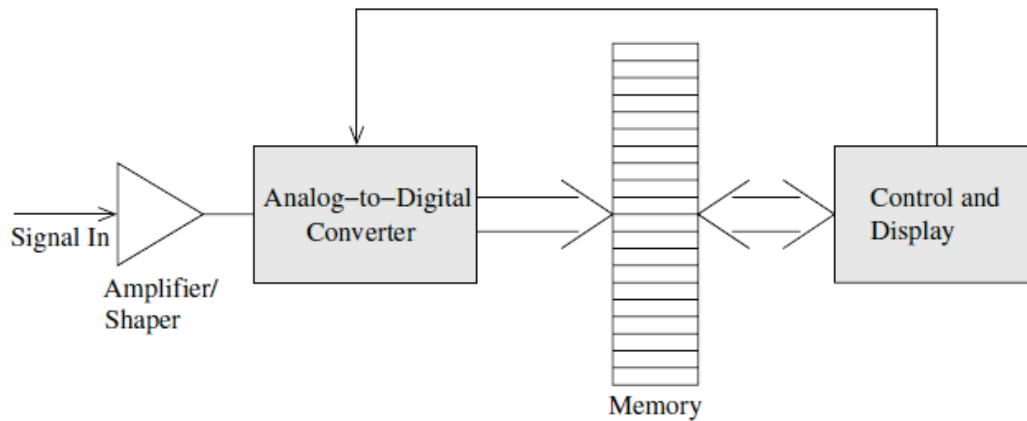


Figure 40: Block diagram of a multi-channel analyzer (MCA) designed for pulse height analysis

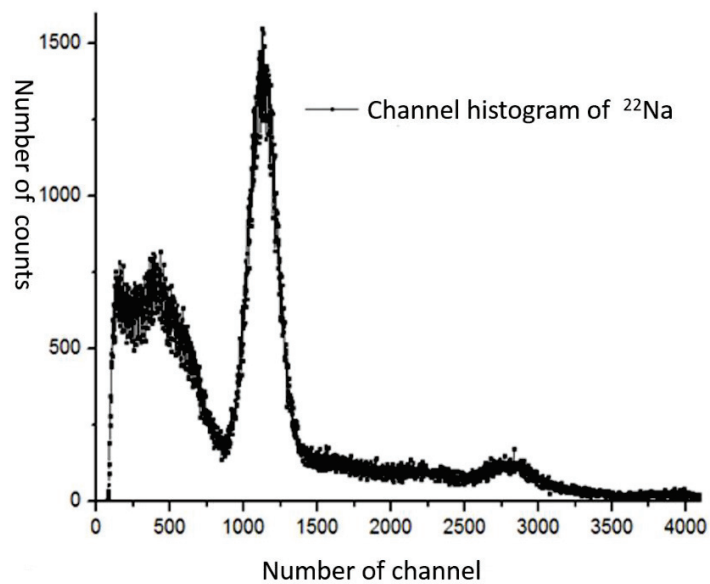


Figure 41: MCA channel histogram of  $^{22}\text{Na}$  as measured by AXINT sensors

Since the ADC output is digitized related to the pulse height at the ADC input and this pulse height is in proportion to the energy deposited by a radiation interaction as well. Thus, we plotted an energy histogram of  $^{22}\text{Na}$  as showed in Figure 42.

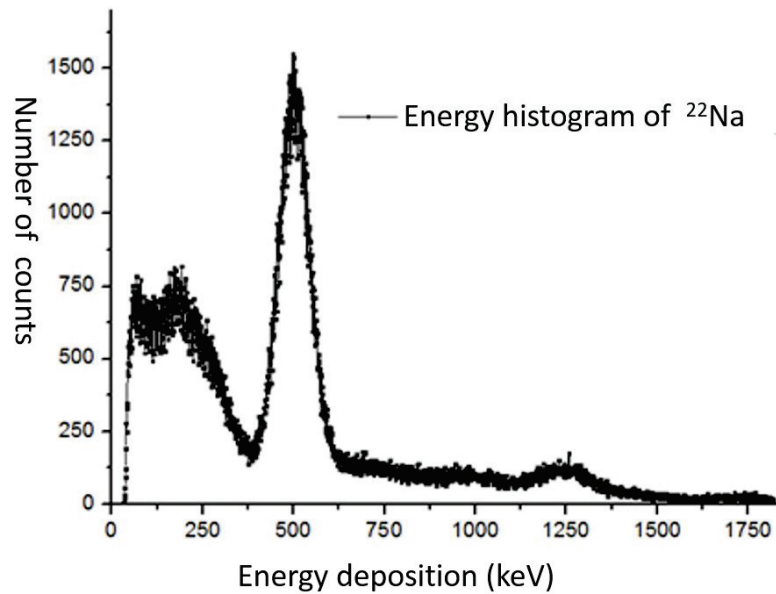


Figure 42: MCA energy histogram of  $^{22}\text{Na}$  as measured by AXINT sensors

## 2.2.7 Digital signal procession and communication protocols

### *Microcontroller: dspic33EP512MC806*

With the advent of cost effective and stability, digital signal processing (DSP) with MCU is used by us. It should, however, be noted that DSP does not eliminate the need for analog circuitry from the electronics chain. Some analog units are always needed to amplify the signal and make it usable for the analog to digital converters. Our MCU (Dspic33EP512MC806) used is a 16-Bit microcontroller with 64 configurable pins working with a CPU speed of 70MHz (Microchip, 2012). It is coded on C language under an integrated development environment (IDE) called MPLABX (microchip, web). For further details please check in ANNEX part of thesis, it gives a general view of programing structure. The overall pin maps are as showed in Figure 43, and they are detailed as follows:



- **SDO(Pin 52):** Serial data output
- **CLK(Pin 50):** Serial clock
- **/CS(Pin 42) and /CS2(Pin 43):** Slave select

### **CAN (Controller Area Network) communication pins:**

The CAN is a communication controller implementing the CAN 2.0 A/B protocol, as defined in the BOSCH CAN Specification (Instruments, 2008). The microcontroller DSP can generate a full CAN control system, and I developed a CAN communication protocol (ANNEXE) used as standard in AXINT sensor system now. Then **TX (Pin 34) and RX (Pin 33)** are connected to the physical medium implemented through a line transceiver such as TI's SN65HVD232 3.3-V CAN transceiver to form a system node as shown in Figure 44, and all nodes are connected to each other through a two wire bus (CANH2, CANL2). The wires are 120  $\Omega$  nominal twisted pair (R270) to avoid signal reflections (Corrigan, 2008).

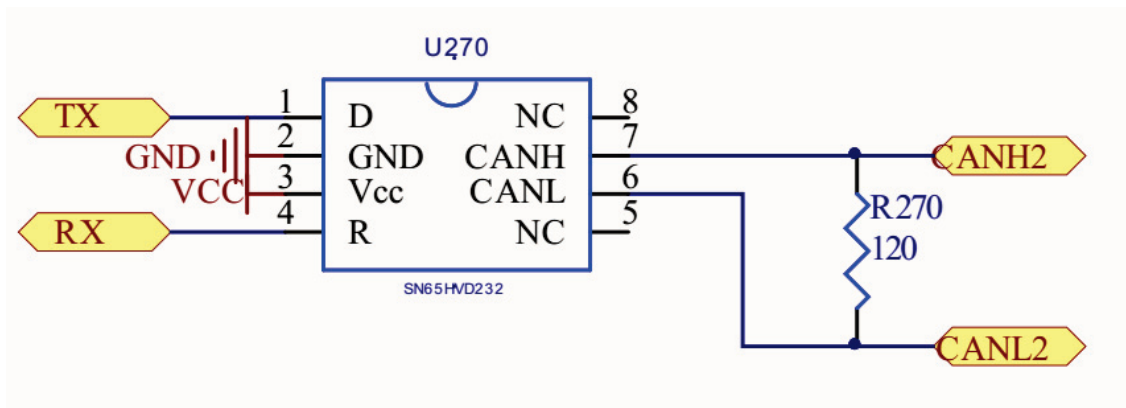


Figure 44: Electronic schema view of CAN transceiver connections

Generally, CAN is a multi-master serial bus standard for connecting Electronic Control Units also known as nodes. Two or more nodes are required on the CAN network to communicate (Figure 45). This guaranteed the multiplicities of communications between nodes or sensors. The node may also be a gateway allowing a standard computer to communicate over a USB or Ethernet port to the devices on a CAN network.

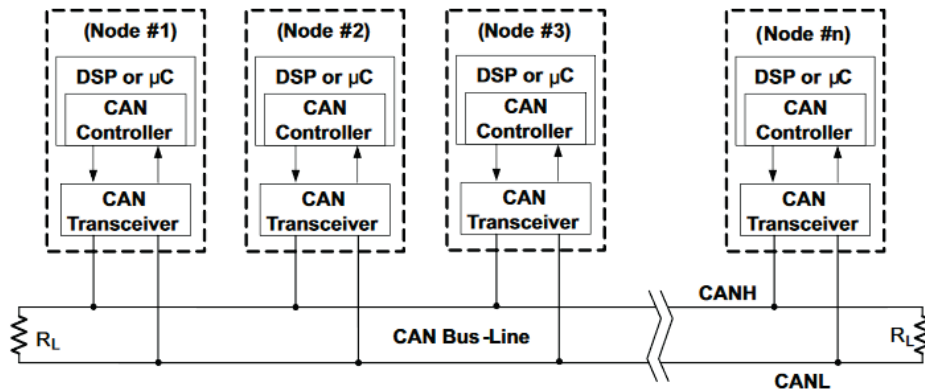


Figure 45: General schematic of CAN network

### **Rising edge Pins:**

As we stated before, the logic output pulse of radiation signal is formed through a comparator and logic output circuit (Figure 38), and is connected to microcontroller of **Mono2 (pin32)** (Figure 43). The interruption timer related to the counting of rising edge is activated through configuration operations refer to microcontroller datasheet.

### **Energy histograms Pins:**

The energy histogram has been obtained using external ADC (Part AD7472) conversion and a control chip select of **RAZcrete2 (Pin 55)** (Figure 43). Once the pulse height have been digitalized through an external ADC, RAZcrete has to be set at low level to eliminate the pile up of the radiation signals. This reset to low level have been preformatted through a switch transistor (BC817) (Figure 46), when RAZcrete2 is at low level, the transistor is not activated until the RAZcrete2 is set at high level. Then the signal has been digitalized (crete2) is connected to ground (AGND) to be cleaned up through this transistor.

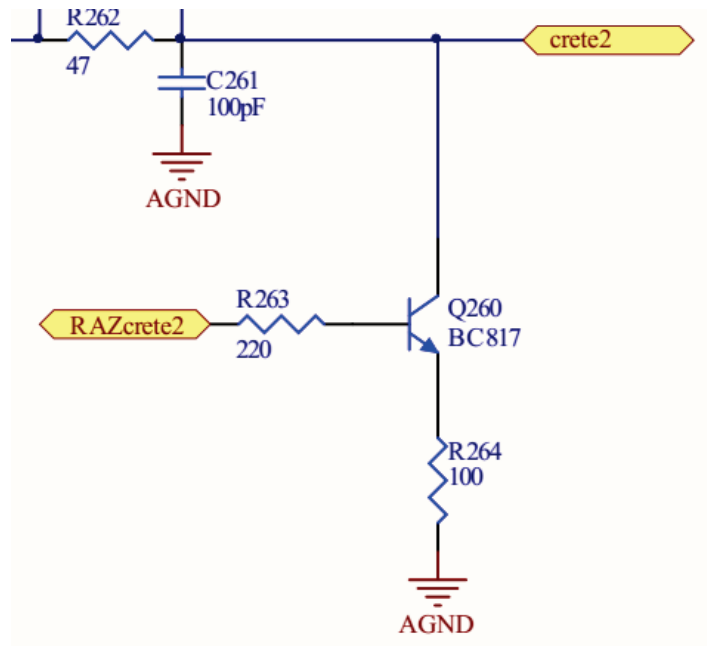


Figure 46: Electronic view of switch transistor

The external ADC conversion process have been interfaced via DSPs. To be detailed, both **ADC\_CLK (Pin 59)**, **ADC\_BUSY (Pin 58)**, **CONVST (Pin 60)** communicated with DSP control the conversion process, and the 12 bit parallel output data is mapped to **Pins BIT1-BIT12** to be digitized into 12 bit prepared for further calculation and accumulation in a histogram.

### **Configuration requirements for DSP**

Up to now, we introduced all the functionalities of mapped DSP pins. Nevertheless, in MCU programming, the tedious work is to configure them properly, this requires a numerous of work in understanding of the MCU datasheet, in creating different communication (CAN and SPI) and ADC conversion protocols. Overall, developing a MCU programing, a lot of lecture work are indispensable.

## 2.2.8 Friendly interpretation interface: Labview

All the software were developed in LabVIEW development environment. Instead text coding as Java or C++, LabVIEW (short for Laboratory Virtual Instrument Engineering Workbench) is a system-design platform and development environment for a visual programming language from National Instruments and has various benefits as following:

1. Easy to learn
2. Rapid programming pace
3. Effortless interfacing to hardware using bus commands
4. Automatic code compilation
5. Large libraries
6. Parallel programming
7. Large user community support

Each VI has two components: a block diagram and a front panel (Instruments N. , 2013) (Figure 47). The front panel is built using controls and indicators. Controls are inputs – they allow a user to supply information to the VI. Indicators are outputs – they indicate, or display, the results based on the inputs given to the VI. The front panel, which is a block diagram, contains the graphical source code.

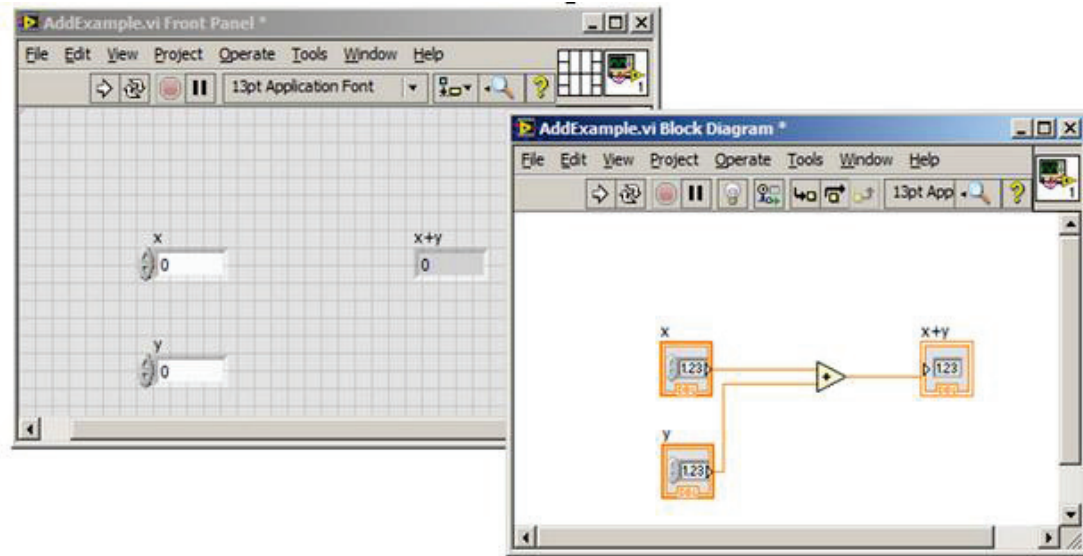


Figure 47: LabVIEW Windows: Front Panel and Block Diagram

All of the objects placed on the front panel will appear on the back panel as terminals. The back panel also contains structures and functions which perform operations on controls and supply data to indicators. The structures and functions are found on the Functions palette and can be placed on the back panel. Collectively controls, indicators, structures and functions will be referred to as nodes. Nodes are connected to one another using wires.

## 2.3 Statistics for data analysis

Radioactive decay and other nuclear reactions are randomly occurring events, and therefore must be described quantitatively in statistical terms.

The statistical methods

In the measurement of any quantity, an error or deviation from the true value is likely to occur. We begin by assuming that we have a collection of  $N$  independent measurements of the same physical quantity:

$$X_1, X_2, X_3, X_4, X_5 \dots X_i, \dots X_N$$

For example, these measurements quantity can be represented as integer values measured by a radiation counter for repeated time intervals of equal length. To characterize such sets of measurements data, two fundamental parameters are can be considered: The mean value and the standard deviation.

The mean value as showed in is obtained by adding the values of all measurements divided by the number of measurements.

$$\text{Equation 7} \quad \bar{x} = \sum_{i=1}^N x_i / N$$

And the standard deviation ( $\sigma$ ) expressed in Equation 8 of a series of measurements indicates the deviation from the mean value and a measurement of the precision.

$$\text{Equation 8} \quad \sigma^2 = \frac{1}{N} \sum_{i=1}^N (x_i - \bar{x})^2$$

Another convenient way to represent a set of measurement data is to use frequency distribution function  $F(x)$ . The value of  $F(x)$  is the relative frequency with which the occurrence number appears in the collection of data.

$$F(x) = \text{Number of occurrences of the value } x / \text{Number of measurements } (=N)$$

And the distribution is automatically normalized, that is,

$$\sum_{x=0}^{\infty} F(x) = 1$$

The distribution functions can correspond to different laws, e.g: Gaussian (or normal) as illustrated in Figure 48 , Poisson, binomial.

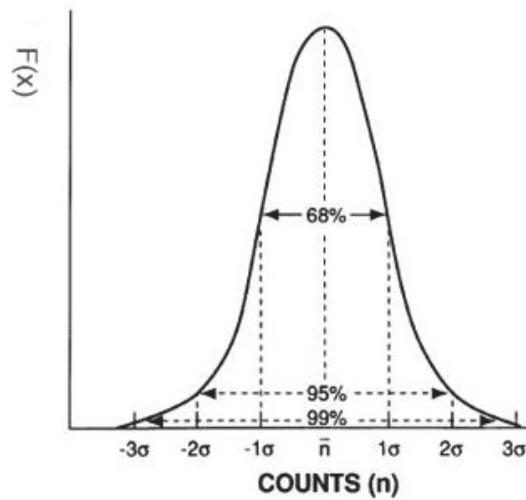


Figure 48: Example of Gaussian frequency distribution

If a series of measurements are made repeatedly on a radioactive sample giving a mean counts superior to 25 or 30, then the distribution of counts would normally follow a Gaussian law (F.KNOLL). From Figure 48, it can be seen that 68 % of all measurements fall within one standard deviation ( $\sigma$ ) on either side of the mean, that is, within the range  $n \pm \sigma$ . 95 % of all measurements fall within the range  $n \pm 2\sigma$  and 99 % fall within the range  $n \pm 3\sigma$ .

If the number of measurements is small, the distribution can be approximated by a Poisson distribution. In this thesis, all the radiation statistical approaches are used with Poisson or Gaussian statistical for which the standard deviation sigma ( $\sigma$ ) is given by  $\sqrt{\bar{N}}$ , with  $\bar{N}$  represents an average counts of different time's measurements. And we are always working at 95% confidence level at  $\pm 2\sigma$  (R.Taylor, Second Edition).

In statistical approaches we have treated so far, the direct results of counting experiments are considered. Whereas in real counts situation, the data are processed with subtraction, multiplication, division or addition from different independent measurements to arrive some interest parameters we are looking for. For example in the research of net counts, a subtraction of total counts to background is required. And these arithmetic

process can induce Error Propagation. We assume a series of independent quantities, say x, y and z, with their respective standard deviations  $\sigma_x$ ,  $\sigma_y$  and  $\sigma_z$ , and  $u(x,y,z)$  represent the calculation function of these quantities, then the standard deviation for this calculation quantity u derived from these independent quantities (x,y,z) can be calculated from formula below:

$$\text{Equation 9} \quad \sigma_u^2 = \left(\frac{\partial u}{\partial x}\right)^2 \sigma_x^2 + \left(\frac{\partial u}{\partial y}\right)^2 \sigma_y^2 + \left(\frac{\partial u}{\partial z}\right)^2 \sigma_z^2$$

Case 1: Subtraction of background count

The most common application of radiation counts from a radioactive source is:

$$\text{Equation 10} \quad \text{Net counts} = \text{Total counts} - \text{Background counts} \quad (u = x - y)$$

With x: Total counts    y: Background counts    u: Net counts

$$\text{Equation 11} \quad \left(\frac{\partial u}{\partial x}\right) = 1 \quad \left(\frac{\partial u}{\partial y}\right) = -1 \quad \left(\frac{\partial u}{\partial z}\right) = 0$$

Applied Equation 11 to Equation 9, in a simple subtraction case, the standard deviation is presented in

$$\text{Equation 12} \quad \sigma_u = \sqrt{\sigma_x^2 + \sigma_y^2}$$

And in Poisson and Gaussians statistics, as mentioned before the standard deviation  $\sigma$  is given by square of mean value of measurements ( $\sqrt{\bar{N}}$ ) Thus the Equation 12 become in Equation 13

$$\text{Equation 13} \quad \sigma_u = \sqrt{\bar{N}_{total} + \bar{N}_{background}}$$

## Case 2: Average Value of Independent Counts

In Poisson and Gaussian statistics, the sigma can be improved by increasing equal counting times. We suppose that we have measured a series of independent variables:

$$X_1, X_2, X_3, X_4, X_5 \dots X_i, \dots X_N$$

With Sum:  $S = X_1 + X_2 + X_3 + \dots + X_N$

The sigma of this sum is expressed as:

$$\sigma_{\Sigma} = \sqrt{\sigma_{x_1}^2 + \sigma_{x_2}^2 + \dots + \sigma_{x_N}^2} = \sqrt{x_1 + x_2 + \dots + x_N}$$

$$\text{Equation 14} \quad \sigma_{\Sigma} = \sqrt{\Sigma}$$

Supposed the average of these N independent measurements is:  $\bar{x} = \frac{\Sigma}{N}$

Then the standard deviation of this average parameter is expressed as:

$$\sigma_{\bar{x}} = \frac{\sigma_{\Sigma}}{N} = \frac{\sqrt{\Sigma}}{N} = \frac{\sqrt{N\bar{x}}}{N} = \sqrt{\frac{\bar{x}}{N}}$$

Thus this mean value of N independent counts gives a sigma that is smaller by a factor compared with any single measurement. Thus its expected standard deviation becomes:

$$\text{Equation 15} \quad \sigma_{\bar{x}} = \sqrt{\frac{\bar{x}}{N}}$$

Where  $\bar{x}$  represents the average value of all the independent measurements and N means the number of equal counting times.

## The limits of detection

A radiation monitoring detector can only detect source activity greater than background. With increased interest in monitoring of radioactive wastes, measuring low level radioactivity is often required and the determination of the limits of detection is very essential.

The limits of detection evaluates the minimum detectable counts of a radioactive source that can be distinguished from the background counts (N.L.Hassing, 1990). Let assume that  $N_T$  to be the number of counts recorder with an unknown sample and  $N_B$  to be the number of recorder counts when a blank sample is substituted to determine the background level. Thus the net counts resulting from the unknown sample are then calculated as

$$\text{Equation 16 } N_S = N_T - N_B$$

To make a decision whether the sample contains activity,  $N_S$  is then compared with critical level  $L_c$ . If  $N_S$  is less than  $L_c$ , it is conclude that the sample does not contain activity, whereas if  $N_S$  exceeds  $L_c$ , it is assumed that some real activity is present.

The well-known limits of detection is deducted as follows:

Firstly, to understand the original of limits of detection, we assume the case that in the absence of statistical fluctuations and source activity, the detection probability of net counting should always be at 1(100%), and both  $N_S$  and  $L_c$  could be set at 0 as showed in Figure 49.

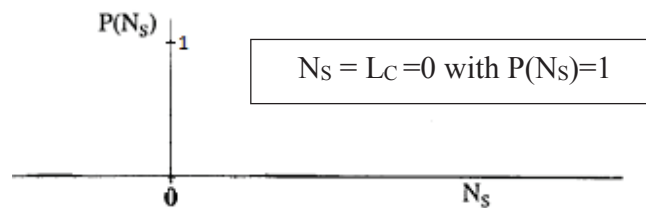


Figure 49: Distribution expected for the net counts  $N_S$  in absence of statistical fluctuations

Whereas in the radiation count system, it follows Poisson or Gaussian distribution as showed in Figure 50, and this is the origin of limits of detection. The Figure 50 shows the expected probability distribution (Poisson distribution) of  $N_S$  value in the case no activity present in the sample. The false positive rate presents the percent of background count that have been regarded as radioactivity count. Normally, it is set to be 5% of false positive rate. Thus  $L_C$  is at 95% confidence level ( $2\sigma_{N_S}$ ).

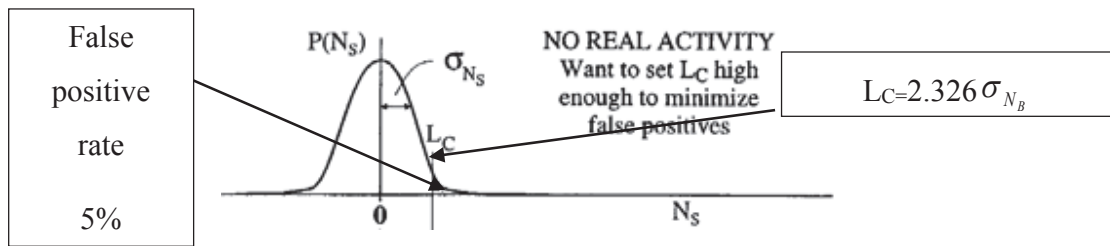


Figure 50: Probability distribution expected for the net counts  $N_S$  in case of no real activity

As in Equation 16, two variables ( $N_T$  and  $N_B$ ) are subtracted to determine  $N_S$ , the standard deviation of net counts can be predicted using Equation 13.

$$\sigma_{N_S} = \sqrt{\bar{N}_B + \bar{N}_T}$$

And in our case, the true mean value of  $N_T$  and  $N_B$  are the same, thus the standard deviation of this subtraction is expressed in

$$\sigma_{N_S} = \sqrt{2\bar{N}_B}$$

And if we were to accept a 5% false positive rate ( $1.645\sigma$  or 90% on distribution), then  $L_C$  is at  $1.645 \sigma_{N_S}$ , thus it gives:

$$\text{Equation 17: } L_C = 1.645 * \sqrt{2\bar{N}_B} = 2.32 \sigma_{N_B} \text{ with } \sigma_{N_B} = \sqrt{\bar{N}_B}$$

Now we assume that the real activity is present in the sample, thus the true mean value of  $N_s$  (in abscissa) is a positive value as showed in Figure 51. False negative rate is defined as the probability of radioactive source counts that be treated as noise counts. This false negative rate is commonly at 5% basically.  $N_D$  represents the minimum net value of  $N_s$ . And this value is defined to a count that produce a mean value of  $N_s$  that is high enough to reduce the false-negative rate to an acceptable level at 5%.

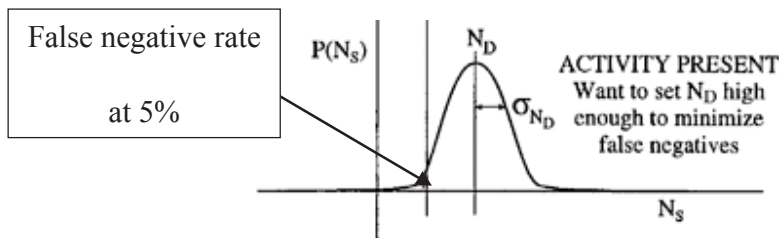


Figure 51: Probability distribution expected for the net counts  $N_s$  in case of real activity

To ensure that the  $N_D$  probability distribution above  $L_C$  level comprise 95% of the distribution area,  $N_D$  is determined at

$$\text{Equation 18} \quad N_D = L_C + 1.645 \sigma_{N_D}$$

We use approximation that  $N_D \ll N_B$  and the width of the distribution of the source + background is approximately the same as that of the background only. It gives using Equation 13:

$$\text{Equation 19:} \quad \sigma_{N_D} = \sqrt{2} \sigma_{N_B}$$

Applied Equation 19 to Equation 18, the  $N_D$  is determined :

$$N_D = L_C + 1.645 * \sqrt{2} \sigma_{N_B} = L_C + 2.326 \sigma_{N_B} = L_C + 2.326 \sqrt{N_B}$$

In Equation 17,  $L_C = 2.326 * \sigma_{N_B} = 2.326 * \sqrt{N_B}$ , thus it gives

$$\text{Equation 20: } N_D = 4.653 \sqrt{N_B}$$

Obviously, in the above demonstration, the assumption that the width of the net distribution of  $N_S$  with activity is the same as the width of the net distribution without activity. Certainly, these widths are not exactly the same, a more rigorous deviation is:

$$\text{Equation 21: } \sigma_{N_D} = \sqrt{N_B + N_D + N_B} = \sqrt{2N_B + N_D}$$

Expanding for  $N_D \ll N_B$ :

$$\text{Equation 22: } \sigma_{N_D} \cong \sqrt{2N_B} \left(1 + \frac{N_D}{4N_B}\right)$$

We put  $\sigma_{N_B} \cong \sqrt{N_B}$  into Equation 22 to get:

$$\text{Equation 23: } \sigma_{N_D} = \sqrt{2} \sigma_{N_B} + 1.645$$

We know from Equation 18

$$N_D = L_C + 1.645 \sigma_{N_D}$$

Using the values for  $\sigma_{N_D}$  specified by Equation 23 and  $L_C$  from Equation 17

$$N_D = 4.653 \sigma_{N_B} + 1.645(\sqrt{2} \sigma_{N_B} + 1.645)$$

This is the frequently-quoted **Currie Equation**.

$$N_D = 4.653 \sigma_{N_B} + 2.706$$

## 2.4 The radiotracers simulation tools

### 2.4.1 How to simulate radiation phenomenon?

#### *2.4.1.1 Introduction Monte Carlo (Monte Carlo N-Particle Transport Code)*

In the field of nuclear engineering, deterministic (e.g., discrete ordinates) and stochastic (Monte Carlo) methods are widely used to solve radiation transport problems. Deterministic methods produce detailed, system-wide solutions and are computationally efficient. The differential Boltzmann transport equations describe how radiation fields could be transformed on average when passing through a given mass thickness (Santin, Chapter II). As a consequence of the mathematical approach in the analytical solutions, deterministic methods are in general extremely fast, even for deep penetration problems. However, they contain uncertainties associated with the discretization of the independent variables (space, energy or angle) of the transport equation and can admit solutions that exhibit non-physical features (e.g., ray effects and negative fluxes); i.e: the case of shielding applications. On the other side, Monte Carlo method, also known as stochastic simulation, implements a generic computation method that makes use of random numbers in its algorithm for the solution. It ensure detailed, explicit geometric, energy, and angular representations and hence is considered as the most accurate method available for solving complex radiation transport problems (John C. WAGNER, 2011). To the term called MCNP (Monte-Carlo N-Particles transport) was developed at beginning by Los Alamos National Laboratory is used for the simulation of nuclear process, such as fission, then it has been extended to simulate neutron, photon, electron, or coupled neutron/photon/electron transport. Specific areas of application including radiation protection and dosimeter, radiation shielding, radiography, medical physics, nuclear

criticality safety, detector design and analysis, accelerator target design have been really affected by the development of Monte Carlo algorithms (Shultis, 2004-2011).

### *2.4.1.2 MCNP simulation process*

Monte Carlo particle transport simulation consists of following each particles from a source throughout its life to its death by absorption, escape, etc. Probability distributions are then randomly sampled using transport data to determine the outcome at each step of life.

Numbers between 0 and 1 are selected randomly to determine what (if any) and where interaction takes place, based on the rules (physics) and probabilities (transport data) governing the processes and materials involved. In this particular example (Figure 52), a neutron collision occurs at event 1; the neutron is scattered in the direction shown, which is selected randomly from the physical scattering distribution. A photon is then produced and is temporarily stored, or banked, for later analysis. At event 2, fission occurs, resulting in the termination of the incoming neutron and the birth of two outgoing neutrons plus one photon. Again one neutron and the photon are banked for later analysis. Then the first fission neutron is captured at event 3 and terminated. The banked neutron is now retrieved and, by random sampling, leaks out of the slab at event 4. The fission-produced photon has a collision at event 5 and leaks out at event 6. The remaining photon generated at event 1 is now followed with a capture at event 7 and so on. Note that MCNP retrieves banked particles (such that the last particle stored in the bank) is the first particle taken out (Team, 2003).

This neutron path history is now complete. Several histories like that the previous one are followed with an information about the neutron and photon distributions. The quantities of interest (whatever the user requests) are tallied, along with estimates of the statistical precision (uncertainty) of the results.

### Event Log

1. Neutron scatter, photon production
2. Fission, photon production
3. Neutron capture
4. Neutron leakage
5. Photon scatter
6. Photon leakage
7. Photon capture

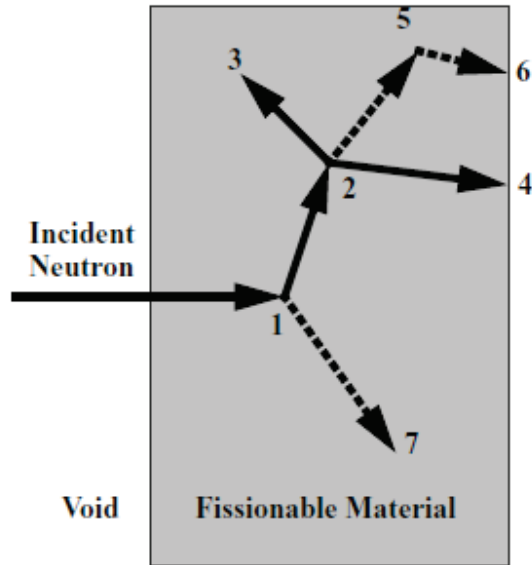


Figure 52: Random history of a neutron incident on a slab of material that can undergo fission

### *2.4.1.3 Structure of the MCNP Input File*

In the following paragraph, we will describe how to construct MCNP simulations following an example of MCNP sample code. First of all, we should know the basic units used in MCNP simulations: (1) length in cm, (2) energy in MeV, (3) time in shakes ( $10^{-8}$ s), (4) temperature in MeV (kT), (5) mass density in  $\text{g}\cdot\text{cm}^{-3}$ , and (6) cross sections in barns. The user creates an input file consists of 3 principal input blocks: **Cell cards**, **Surface cards**, **Data cards**. To be better understand the structure and functionality of MCNP file, we show a MCNP simulation sample as follows (Figure 53):

Our example is to study the NaI detection efficiency of 1 inch ( $2.54\text{cm}\times 2.54\text{cm}$ ) size to detect gamma emissions @511KeV placed 2 cm away from NaI crystal. To be similar to the real experimental setup conditions, a layer of aluminum had to be considered, and we are looking for number of photons that are absorbed in crystal.

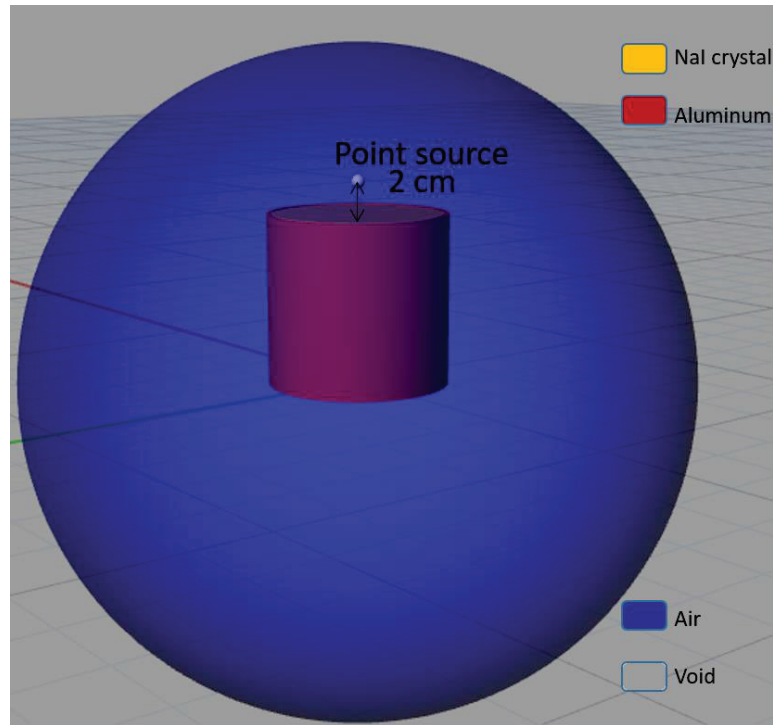


Figure 53: Sample 3D geometry view for determination of NaI detection efficiency by MCNP simulations

**1: The simulation geometry (Surface card and Cell cards):**

The traditional geometry of MCNP treats an arbitrary 3-dimensional configuration in geometric cells bounded by first- and second-degree surfaces or fourth-degree elliptical tori. Cells are defined as showed in Figure 54, by the intersections, unions, and complements of the regions bounded by the surfaces. This construction methodology is called Constructive Solid Geometry (CSG). Surfaces are described by supplying coefficients of the analytic surface equations or, for some types of surfaces, known points on the surfaces. MCNP also provides a “macrobody” capability, where basic shapes such as spheres, boxes, cylinders, etc., might be combined using Boolean operators (Team, 2003).

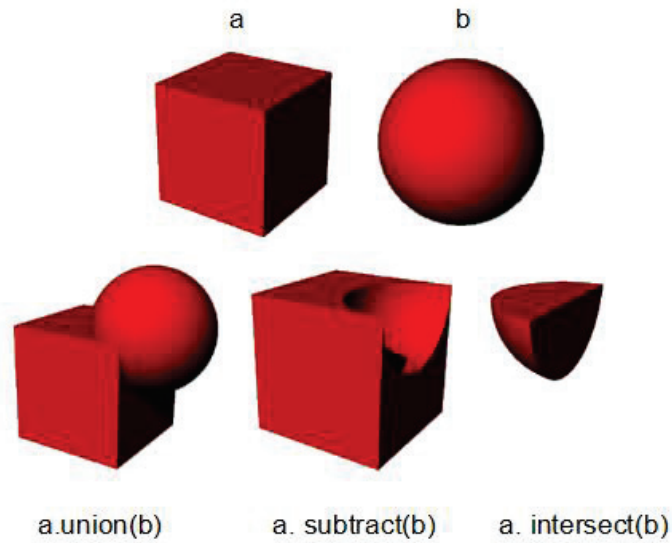


Figure 54: CSG methodology for MCNP6

**Surface cards:**

First of all, we will see how the surfaces are defined to be used for cell construction later. Taken our example, 7 surfaces were defined using MCNP integrated surface card (Table 9: page 3-13 of MCNP5 manual). Each cylinder cell is composed of 3 surfaces (Top and base plan surface, cylinder surface). 2 cylinder cell account for 6 surfaces card and a sphere surface card is prepared to limit particles simulation space (Figure 55). No particles can be found outside of this sphere.

Mnemonic	Type	Equation	Card Entries
PZ	Plane	$Z-D=0$	D
CZ	Cylinder	$x^2+y^2-R^2=0$	R
SO	Sphere centered at origin	$x^2+y^2+z^2-R^2=0$	R

Table 9: MCNP surface cards used for sample codes

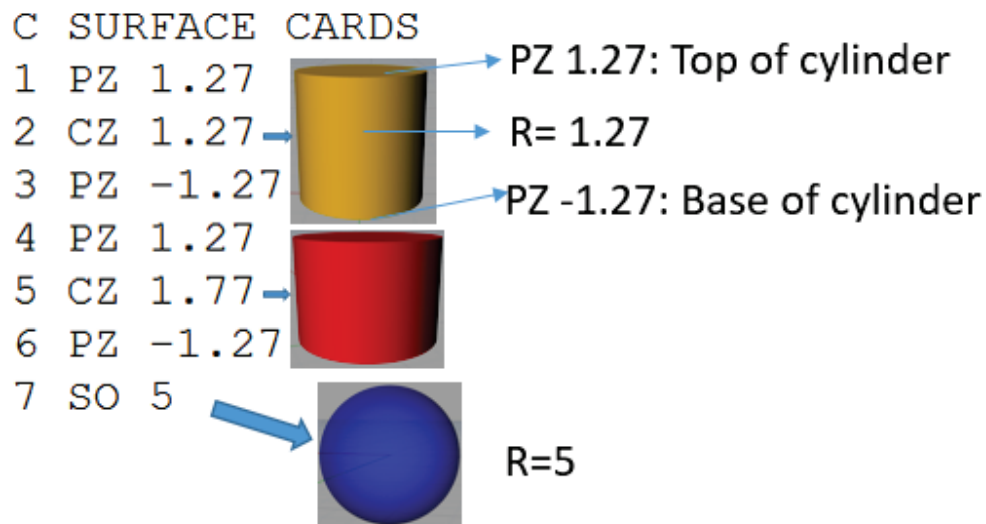


Figure 55: MCNP surfaces block sample code

**Cell block:**

In cell block, we will illustrate how surfaces and Boolean logic are used to define cells by considering our example (Figure 56). The first number on a cell definition card is the cell number. The following number represents cell filled by one material number. The third number illustrate the density of filled material (Positive: Atom density in units of  $10^{24}$  atoms/cm<sup>3</sup>). Then the next set of numbers before IMP are intersection of surfaces. Taken the first cell as example, the NaI cylinder cell is defined as inside the cylinder surface 2, below plane 1 and above plane 3 (Figure 55). The last IMP specification define the importance of simulated particles in this region like neutron for example. No specific defined of importance will be set at 1 as default.

```

C Cell cards
1 2 -3.67 -2 -1 3 imp:n=1 $Crystal NaI
2 3 -2.7 6 -5 -4 #1 imp:n=1 $ Al
3 1 -1.293e-3 -7 #1 #2 imp:n=1 $ Air
4 0 7 imp:n=0 $ void

```

Figure 56: Cell cards specification for MCNP sample code

## 2. Data cards:

This block of data cards defines the type of particles, problem materials, radiation sources, how the results have to be scored (or tallied), the particles to be simulated (Table 10) (Team, 2003).

	MCNP data cards name
Material specification	Mn
Mode	Mode
Source specification	SDEF
Tally specification	Fn,En
Cut off particles	NPS

Table 10: Essential information requirements for MCNP data cards

### Material specification:

Specification of materials filling the various cells in an MCNP calculation involves the following elements: (a) defining a unique material number, (b) the elemental (or isotopic) composition, and (c) the cross section compilations to be used. Taken the first column of material specification (Air) as example (Figure 57), the first value m1 present the material number 1. For each elemental composition, it composed of ZZZAAA in which ZZZ is the atomic number and AAA is the atomic mass number.

AAA=0 means naturally occurring element, it can be set to 000 as default only except for neutron transport problems, the atomic mass number must be specified. 7000 defines an elemental of nitrogen with nature mixed composition and following 0.784 giving atomic fraction (mass fraction: a negative sign before the value) of nitrogen in air. Using the same argument, the oxygen (8000) and argon (18000) are defined with respective 0.211 and 0.005 atomic fraction.

```
m1 7000 0.784 8000 0.211 18000 0.005 $ Air
m2 11000 1 53000 1$NaI
m3 13000 1 $Al
```

Figure 57: Material specification for MCNP sample code

Mode card:

In this part of code, the transport particles are defined to be simulated. In our case photon transports are used (Figure 58).

```
mode p
```

Figure 58: Mode specification for MCNP sample code

### Source specification (SDEF)

The source properties are characterized in source specification SDEF part related to different MCNP data cards name (POS, CEL, ERG, and WGT) (Table 11). Only some essential MCNP data cards name are listed.

POS = x y z	Default is 0 0 0
CEL = starting cell number	
ERG = starting energy	Default is 14 MeV

WGT = starting weight	Default is 1
-----------------------	--------------

Table 11: Source specification in MCNP data cards

In our example, we simulated gamma particles source with an energy of 511KeV at position (0, 0, 3) (Figure 59).

```
SDEF ERG=0.511 POS=0 0 3
```

Figure 59: Source specification for MCNP sample code

**Tally specification:**

In MCNP code, the tally specification indicates the types of results we are looking for from simulation process (Table 12).

F1	Surface current
F2	Surface flux
F4	Track length estimate of cell flux
F5	Flux at a point (point detector)
F6	Track length estimate of energy deposition
F8	Energy distribution of pulse created in a detector

Table 12: Tally specification in MCNP data cards

In our situation, we expected to score the number of photons that can be absorbed in NaI crystal (Cell 1) (Figure 60).

```
f8:p 1
```

Figure 60: Tally specification for MCNP sample code

### **Cut off particles (NPS):**

MCNP data card name “NPS” following by a value define the number of particle to be simulated. This value should not to be high and low for time consuming and statistic considerations. In our case, 100000 particles has been simulated.

### **Complete MCNP sample code:**

Finally, we can construct a complete MCNP code revealed in the following figure (Figure 61).

```
Example source code
C Cell cards
1 2 -3.67 -2 -1 3 imp:n=1 $Crystal NaI
2 3 -2.7 6 -5 -4 #1 imp:n=1 $ Al
3 1 -1.293e-3 -7 #1 #2 imp:n=1 $ Air
4 0 7 imp:n=0 $ void

C SURFACE CARDS
1 PZ 1.27
2 CZ 1.27
3 PZ -1.27
4 PZ 1.27
5 CZ 1.77
6 PZ -1.27
7 SO 5

C Data block
m1 7000 0.784 8000 0.211 18000 0.005 $ Air
m2 11000 1 53000 1$NaI
m3 13000 1 $Al
mode p
SDEF ERG=0.511 POS=0 0 3
f8:p 1
nps 100000
```

Figure 61: MCNP sample codes

## 2.4.2 Development of CAD or CFD auto-conversion algorithm

### 2.4.2.1 Introduction

#### **Context:**

As we saw previously, MCNP code was used to simulate the transport of particles, and we are looking for track the photon particles. Nevertheless, to fulfill the technical requirements for the DRN MCNP simulations, it is impossible to use MCNP code with CSG geometric description, we had to face to two difficulties:

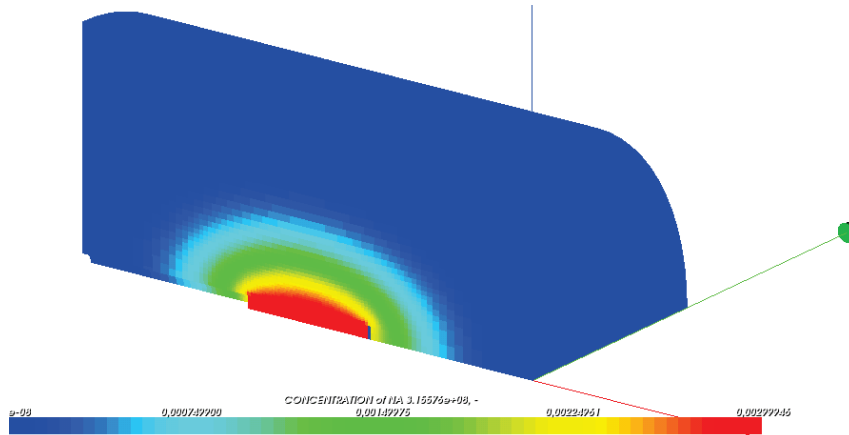
1. How to create a complex geometry?

As stated before, the simulation geometry can be easily defined by a set of boolean operations of one and two-dimensional surfaces (CSG methodology), but it is limited when it comes to construct more complex geometries, the process is difficult, time-consuming, and error-prone (Kelley, 2009).

2. How to use CFD results as input data in MCNP code for source description?

The activity distribution of radiotracers modeled by CEA/L3MR is represented by tetrahedral meshes with activity value attributed to each polygon (Figure 62), no classical MCNP tools were able to interpret such a meshe structure.

Nevertheless, since the release of the latests version of MCNP (MCNP6), a new functionality has been introduced, called “Unstructured Mesh input function”. This function has been developed to be able to import Abaqus/CAE problems into MCNP6. Nevertheless, there are some strong technical limitations for use in our problems.



The MCNP6 code developers usually chose to implement a mesh geometry into the code build for hybrid geometries (CSG+Mesh geometries) (Figure 63 for example). The “official” first step for creating of unstructured mesh geometries are building solid parts in Abaqus/CAE (Chelsea A. D’Angelo, 2012). Then they are meshed according to the type and size of element desired for the specific application and finally provide different choose of basic mesh elements as revealed in Figure 64. We can conclude that this unstructured meshed, created by Abaqus/CAE, can also be built by any software as long as the files and data formats remains the same, and so can be interpreted and integrated directly into MCNP code.

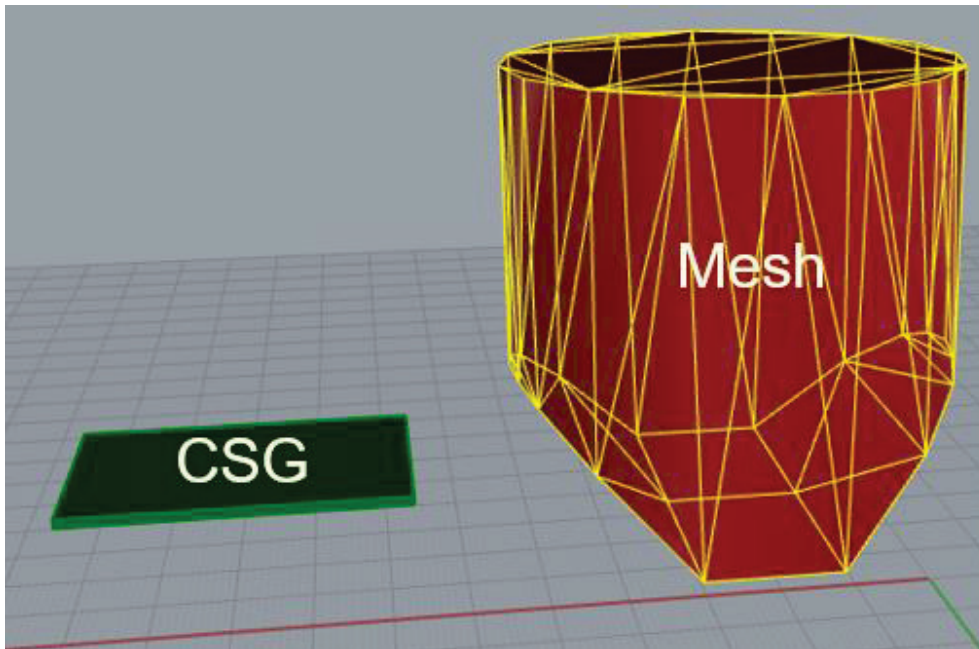


Figure 63: Hybrid geometry construction

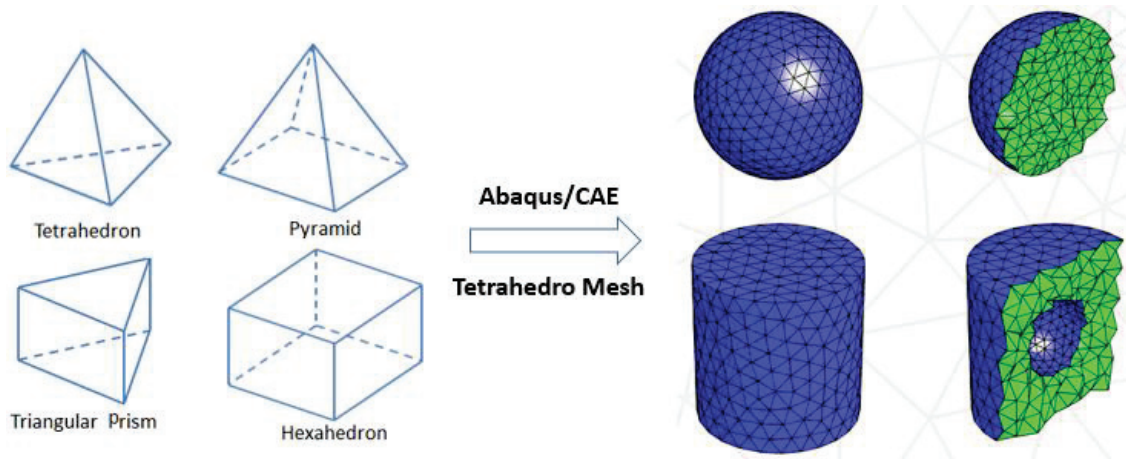


Figure 64: Basic mesh elements and construction of 3D meshes via Abaqus/CAE

### **The Abaqus/CAE .inp files structure:**

We have known that the key file used to be imported into MCNP6 code is Abaqus/CAE “inp” file. If the raw data exists, it is easy to convert it to the ABAQUS “inp” file format. As a consequence, we should understand how a specific “inp” file is structured. A complete “INP” file should consist of following object: **Part, Elset, Instance, Assembly, Material and density.**

### **Part and Elset:**

Part is defined as the smallest geometric object created in the Abaqus/CAE tool. It is built by smallest unstructured polyhedrons with 4-, 5-, and 6-sides or faces (tetrahedral, pentahedra, hexahedral, tetrahedral). Obviously, the form of unstructured polyhedrons depends on the number of **nodes** and **element**. After part is physically constructed, then it should be attributed with **element set of material** and **statistics set** (Figure 65). We should remark that element set of material are the way to group collections of elements for the purpose of volume based MCNP tallies. In an Abaqus/CAE input file (inp), in general, comments begin with a double asterisk, “\*\*”. Keyword lines begin with a single asterisk, “\*” and are followed by the keywords.

```

*Part, name="S1_101_source_1.2"
*Node
1, -93., 0., 0.
2, -93., 1.900000, 0.
3, -94., 1.900000, 0.
4, -94., 0., 0.
5, -92., 0., 0.
6, -92., 1.900000, 0.
7, -91., 0., 0.
.....
311739, -95., -1.216943, -1.230216
311740, -95., -1.168131, -1.346697
*Element, type=C3D8R
1, 1428, 75852, 32740, 2727, 1426, 75869, 33369, 2725
2, 1426, 75869, 33369, 2725, 1425, 75886, 33998, 2688
3, 75869, 75870, 33374, 33369, 75886, 75887, 34003, 33998
4, 75870, 75871, 33379, 33374, 75887, 75888, 34008, 34003
5, 1425, 75886, 33998, 2688, 1409, 75903, 34627, 2686
6, 75886, 75887, 34003, 33998, 75903, 75904, 34632, 34627
.....
4568, 1422, 15886, 31998, 2688, 3409, 45903, 34627, 2286
*Elset, elset=S1_101_source_1.2_statistic_1 generate
1, 4568, 1
*Elset, elset=S1_101_source_1.2_source_1 generate
1, 4568, 1
*End Part

```

Beginning of node specification

Beginning of element specification: hexahedra mesh

Elemental set with statistics

Elemental set with material

Part generate with elements

Figure 65: Sample input part file of Abaqus/CAE used for MCNP6 unstructured mesh

### Instance:

Instance is simply a copy of a part used when constructing an assembly. It begins with “\*Instance” keywords (Figure 66). There are two parameters appearing on the “\*Instance” keyword line: “name” and “part”. The “name” parameter is just the name of the instance and the “part” parameter is the same as one of those used with the part name. The number of “\*Instance” appeared can correspond to the number of parts that were instantiated into the Assembly we will see later.

```

*Instance, name="S1_101_source_1.2", part="S1_101_source_1.2"
*End Instance
**
*Instance, name="S1_201_air1.1", part="S1_201_air1.1"
*End Instance

```

Figure 66: Two instance construction for Abaqus/CAE sample file

### Assembly:

The “\*Assembly” keyword appears after all of the parts are defined. It is the largest geometric object created in the Abaqus CAE/tool and is constructed from instances of parts. Between keywords “\*Assembly and \*End Assembly are the important information used to construct the mesh model from the parts (Figure 67).

```
** ASSEMBLY
**
*Assembly, name=Assembly
*Instance, name="S1_101_source_1.2", part="S1_101_source_1.2"
*End Instance
**
*Instance, name="S1_201_air1.1", part="S1_201_air1.1"
*End Instance
**
*End Assembly
```

Figure 67: Assembly example for Abaqus/CAE sample file

### Material and density:

The next to last keyword of interest in the inp file is “\*Material”. This keyword has one parameter which is the material name. The last keyword of interest to the UM library appearing in the inp file is “\*Density” (Figure 68). If the number is positive, it is a number density. If it is negative, then it would be the negative of a physical density (g/cm<sup>3</sup>). This is the same convention as MCNP.

```
*Material, names=BGO_material_001
*Density
-7.4
*Material, names=Air_material_002
*Density
-1.293e-3
```

Figure 68: Example of material and density for Abaqus/CAE sample file

Finally, we create a complete Abaqus/CAE input file as follows (Figure 69):

```

*Heading
** Job name: Job-9 Model name: Model-1
** Generated by: Abaqus/CAE 6.10-1
*Preprint, echo=NO, model=NO, history=NO, contact=NO
**
** PARTS
**
*Part, name="S1_101_source_1.2"
*Node
1, -93., 0., 0.
2, -93., 1.900000, 0.
3, -94., 1.900000, 0.
4, -94., 0., 0.
5, -92., 0., 0.
6, -92., 1.900000, 0.
7, -91., 0., 0.
.....
311739, -95., -1.216943, -1.230216
311740, -95., -1.168131, -1.346697
*Element, type=C3D8R
1, 1428, 75852, 32740, 2727, 1426, 75869, 33369, 2725
2, 1426, 75869, 33369, 2725, 1425, 75886, 33998, 2688
3, 75869, 75870, 33374, 33369, 75886, 75887, 34003, 33998
4, 75870, 75871, 33379, 33374, 75887, 75888, 34008, 34003
5, 1425, 75886, 33998, 2688, 1409, 75903, 34627, 2686
6, 75886, 75887, 34003, 33998, 75903, 75904, 34632, 34627
.....
4568, 1422, 15886, 31998, 2688, 3409, 45903, 34627, 2286
*Elset, elset=S1_101_source_1.2_statistic_1, generate
1, 4568, 1

*Elset, elset=S1_101_source_1.2_source_1, generate
1, 4568, 1
*End Part
*Part, name="S1_201_air1.1"
*Node
1, -51.159999847412109, 43.099998474121094, -3.2537450488516313e-17
2, -54.659999847412109, 43.099998474121094, -4.3643584365514639e-17
3, -61.659999847412109, 43.099998474121094, -6.5855845502066389e-17
4, -75.660003662109375, 43.099998474121094, -1.1028037439261479e-16
5, -110.66000366210938, 43.233402252197266, -0.69937992095947266e-16
.....
** ASSEMBLY
**
*Assembly, name=Assembly
*Instance, name="S1_101_source_1.2", part="S1_101_source_1.2"
*End Instance
**
*Instance, name="S1_201_air1.1", part="S1_201_air1.1"
*End Instance
**
*End Assembly
**
** MATERIALS
**
*Material, names=BGO_material_001
*Density
-7.4
*Material, names=Air_material_002
*Density
-1.293e-3

```

Figure 69: Abaqus/CAE sample file

### 2.4.2.2 CAD auto conversion algorithm

First of all, we begin with our own development of CAD models to Abaqus/CAE input file. In a whole it was a self-conversion mythology to convert CAD based computational model to the new MCNP6 Embedded Unstructured Mesh source code.

To summary, our technologies consist of 4 main steps (Figure 70):

1. A general CAD or CFD software to produce the initial data;
2. The creation of .STL (Stereo Lithography) files format for each CAD element;
3. A third party software for creating 3D mesh from the .STL input data;

4. A custom LabVIEW program developed by our team to combine the mesh data into one single MCNP geometry input data (Abaqus/CAE format files);

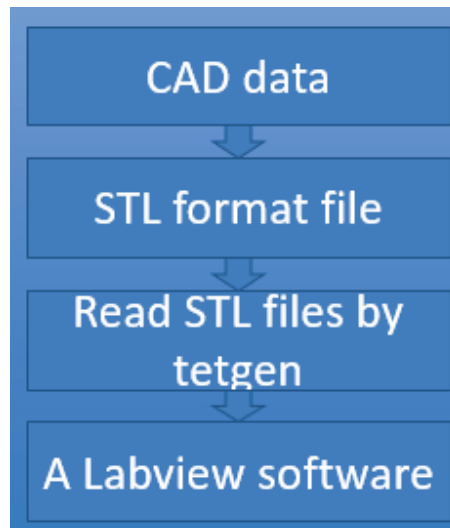


Figure 70: The process of CAD conversion

### **Step 1: CAD data**

As the MCNP input file is complex for the description of geometric model in MCNP code (highly abstract, not intuitive as well as error-prone). Our solution is to build MCNP input file that correspond to CAD model, since CAD software makes use of powerful functions in geometric modeling. It can be constructed through any commercial CAD software (Rhino, Solidworks etc) and then using our algorithm to be simulated in MCNP code.

### **Step 2: STL format file**

After each solid object is created by rhinoceros, we run a script called “export STL” developed by ourselves to form an STL file from each object of the CAD. This

script is to get information of each solid object in xxxx.stl format. The detailed script source code was presented in ANNEX. STL (Stereo Lithography) file is the most widely used and the de-facto standard of Rapid Prototyping (RP) processes; this format was originated by 3D Systems in 1989 (Mitch Heynick, LAPA Digital Technology Seminar ). It describes a raw unstructured triangulated surface by the unit normal and vertices (ordered by the right-hand rule) of the triangles, using a three-dimensional Cartesian coordinate system (Figure 71). STL coordinates must be positive numbers with arbitrary units.

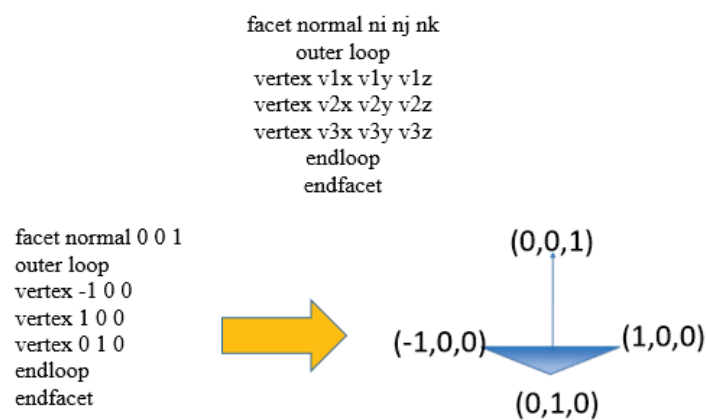


Figure 71: Example of STL file structure for one triangle facets

A typical STL file is composed of a list of triangle facets as illustrated in Figure 72.

```

solid OBJECT
facet normal 0.99720300878640733 -0.074740613238962889 0
  outer loop
    vertex 46.270000457763672 0 17.540000915527344
    vertex 46.255813598632813 -0.18928368389606476 17.540000915527344
    vertex 46.255813598632813 -0.18928368389606476 15
  endloop
endfacet
facet normal 0.99720300878640733 -0.074740613238962889 8.649957348224351e-19
  outer loop
    vertex 46.270000457763672 0 17.540000915527344
    vertex 46.255813598632813 -0.18928368389606476 15
    vertex 46.270000457763672 0 15
  endloop
endfacet
facet normal 0.97492946314650974 -0.22251413862687106 0
  outer loop
    vertex 46.255813598632813 -0.18928368389606476 17.540000915527344
    vertex 46.213577270507813 -0.37433907389640808 17.540000915527344
    vertex 46.213577270507813 -0.37433907389640808 15
  endloop
endfacet
facet normal 0.97492946314650974 -0.22251413862687106 0
  outer loop
    vertex 46.255813598632813 -0.18928368389606476 17.540000915527344
    vertex 46.213577270507813 -0.37433907389640808 15
    vertex 46.255813598632813 -0.18928368389606476 15
  endloop
endfacet
facet normal 0.9308730762949412 -0.36534273747974338 0
  outer loop
    vertex 46.213577270507813 -0.37433907389640808 17.540000915527344
    vertex 46.144229888916016 -0.55103236436843872 17.540000915527344
    vertex 46.144229888916016 -0.55103236436843872 15
  endloop
endfacet

```

Triangle facet

Figure 72: Example of STL file content

### Step 3: Read STL files by tetgen

TetGen program is able to generate tetrahedral meshes of any 3D polyhedral domains (Tetrahedralization) from STL files (Figure 73). We used a line command as follows:

The command in CMD prompt: / tetgen -pq xxxxxx.stl

It allows us to create a xxxxx.ele and xxxxx.node files for each stl solid object (Si, 2013).

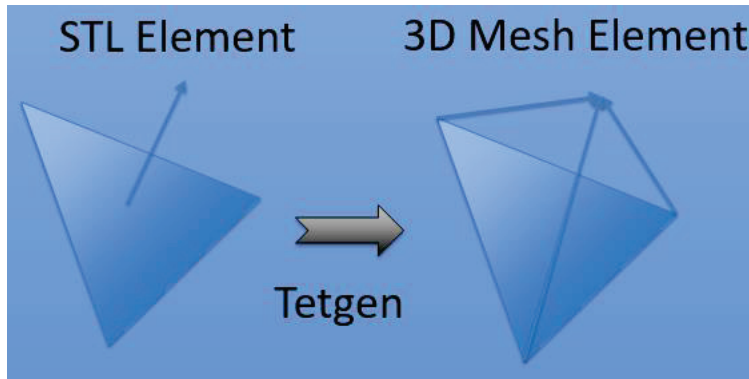


Figure 73: Generation of tetrahedral meshes from TetGen software

Node files (xxxx.node) represent the lists of points in a three-dimensional Cartesian coordinate system, used to construct tetrahedral meshes whereas element files (xxxx.ele) indicate the structure of each tetrahedral mesh formed by 4 nodes (Figure 74).

```

1 Node file created by Tetgen software
2
3 1 46.255813598632812 -0.18928368389606476 17.540000915527344
4 2 46.255813598632812 -0.18928368389606476 15
5 3 46.213577270507812 -0.37433907389640808 17.540000915527344
6 4 46.049324035644531 -0.71541649103164673 15
7 5 45.930976867675781 -0.86381936073303223 15
8 6 45.930976867675781 -0.86381936073303223 17.540000915527344
9 7 45.463981628417969 -1.1822096109390259 17.540000915527344
10 8 45.282600402832031 -1.2381584644317627 15
11 9 45.094905853271484 -1.2664488554000854 17.540000915527344
12 10 45.094905853271484 -1.2664488554000854 15
13 .....
14 .....
15
1 Element file created by Tetgen software
2 1460 4 0
3 1 349 369 451 78
4 2 237 239 365 467
5 3 206 316 363 465
6 4 147 148 367 446
7 5 114 113 243 373
8 6 174 176 251 438
9 7 154 146 444 446
10 8 67 321 320 318
11 9 97 106 258 448
12 10 366 26 420 461
13 11 85 109 434 445
14 12 91 103 452 459
15 13 348 186 350 422
16 .....
17 .....
18

```

Figure 74: Node and element output files created by TetGen software

#### Step 4: Labview conversion process

Based on the element and node files created by Tetgen software, we developed a Labview software that fulfill the translation of 3D tetrahedral meshes to another understandable “language” (MCNP code) (Figure 75).

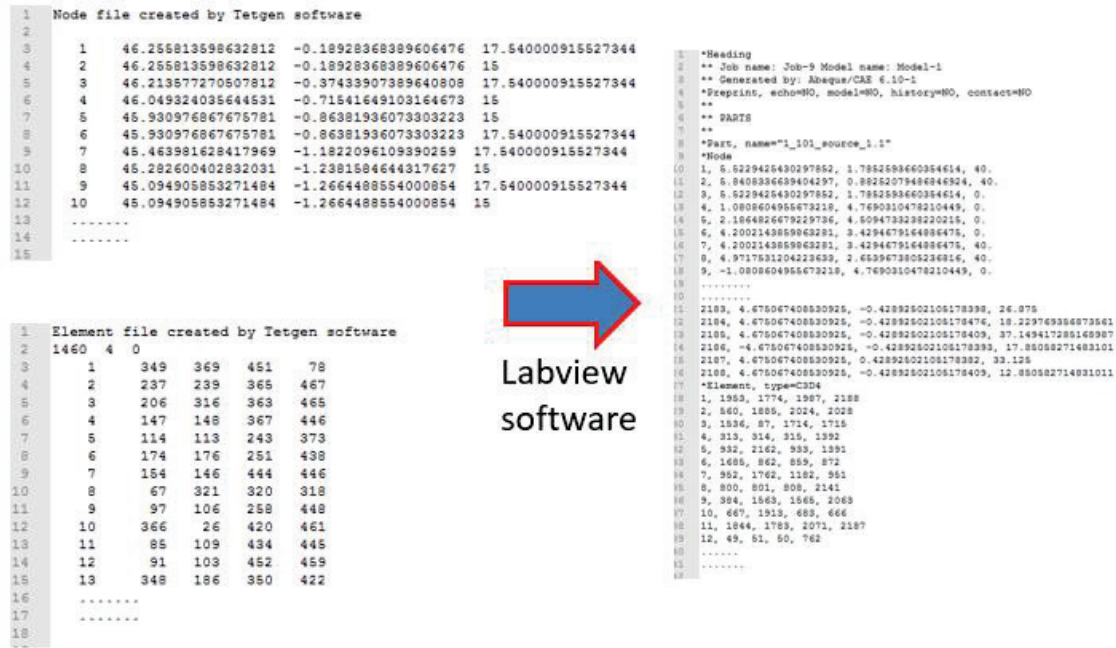


Figure 75: Labview development from 3D meshes to MCNP6 code

The objectives in developing this program is to format the output file into another standard file (xxxx.inp) related on functionality of MCNP6 unstructured mesh. Normally, as cited before, this file can be created through Abaqus/CAE tools. Meanwhile we developed an alternative solution instead of using Abaqus/CAE. The requirements of combinational node and element file plus further more information description in creating an INP file led to many text descriptions appeared in this program (Figure 76). Finally, to be noted that this development gave me the first concrete opportunity to practice Labview.



### 2.4.2.3 CFD auto conversion algorithm

Normally, the CFD data is directly composed of node, element and intensity mesh data, this gives fact to be similar at the last step of CAD auto conversion process (Figure 75), and thus our work was expected to develop only one Labview software that can organize initial CFD data to MCNP code. Nevertheless, it is not always easy to integrate CFD data into MCNP6 unstructured mesh format. Typically, in our situation, I took time in developing conversion program because of various reasons listed follows:

#### **Reformulation of raw data:**

Firstly, the CFD file composed of a geometry information file (nodes and elements) and intensity meshes file separately. Thus, a Labview program was developed to combine 2 files into one file. Secondly, the raw data only consists of one quarter of data (Figure 77). As a result, symmetry operations of nodes, elements and intensity meshes are necessary to construct full space of unstructured meshes. In a whole, all these constraints made us to restructure raw data at first.

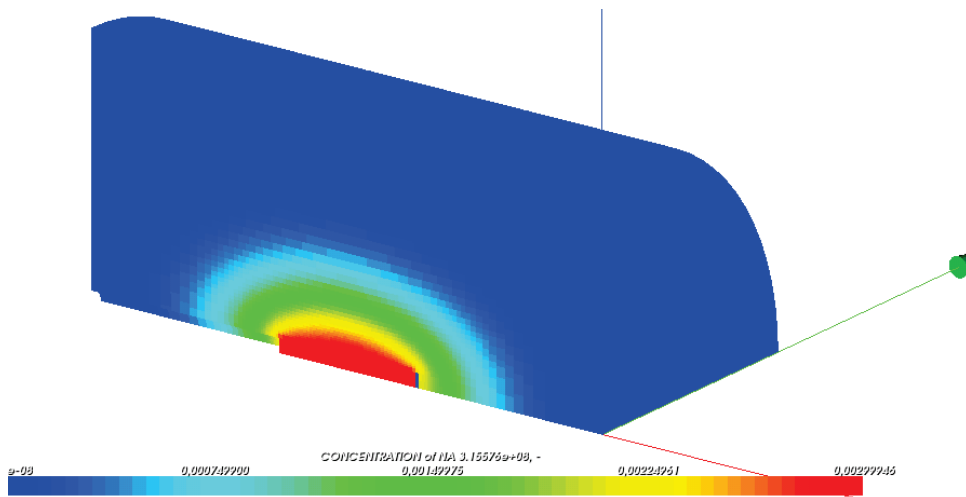


Figure 77: Raw data of CFD file

### **Constraint of MCNP6.1 beta:**

The MCNP6.1 beta evaluation version that we used did not allow the user to define multiply volume source constructed by unstructured meshes. Thus we decided to divide our density meshes (source activity) into 20 layer varying from 0 to 100% (normalized by maximum value) with 5% increment for each layer (Figure 78). Then we had to simulate for each source layer, this gave fact that for a complete formulate CFD data, 20 MCNP simulations had to be performed instead of one simulation with all intensity meshes information. In we illustrated the lists of nodes for 20 density meshes layer, it was recreated by Paraview software (Moreland, Version 3.12) extracting information from reformulated CFD data.

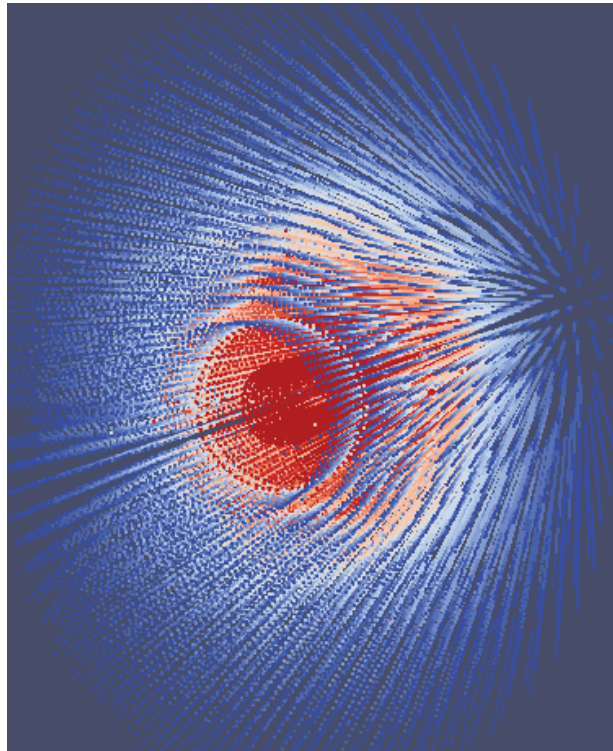


Figure 78: View of CFD list nodes

### Supplementary add of CAD data:

As CFD data gave only information about source distribution in our situation, to fulfill our simulation conditions, various experimental setup part such as monitoring sensors, injection and sensor boreholes had to be taken into account. All these CAD parts were interpreted as MCNP6 unstructured meshes following CAD auto conversion algorithm stated previously and illustrated in (Figure 79).

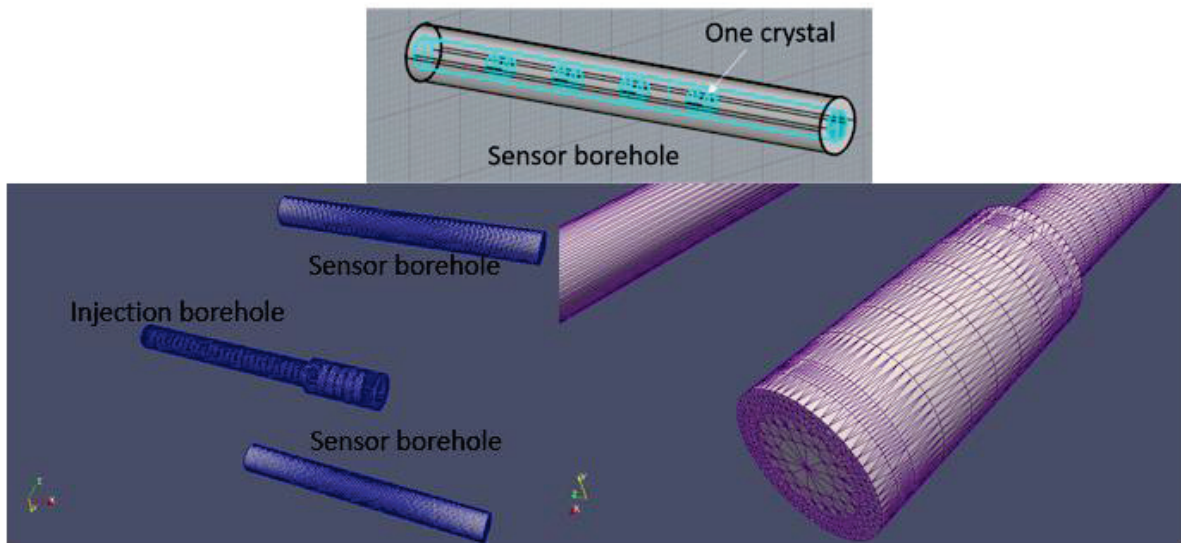


Figure 79: Supplementary imported CAD unstructured meshes view

Finally, CFD plus CAD data are made during my PhD works as showed in bottom part of Figure 80. The full MCNP input code of this example can be found in annex.

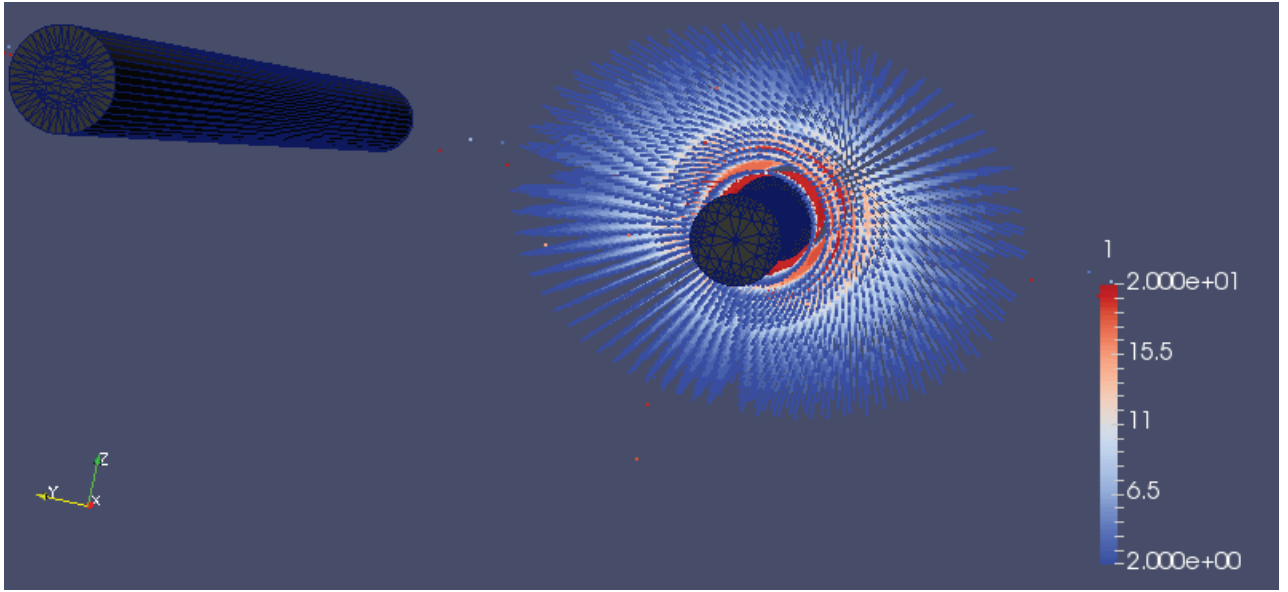


Figure 80: Combination of CFD reformulated data with CAD data

# CHAPTER 3: The in situ tracers diffusion studies

## 3.1 Introduction

As stated before, in November 1999, the underground research laboratories (URL) are built by ANDRA to conduct the research in the feasibility of reversible, deep geological disposal of high –activity, long-lived radioactive wastes in an argillaceous rock host. In order to validate the safety of disposal waste over several tens and even hundreds of thousands of years, three principal research goals are proposed:

- i. Characterization of the edge properties of the argillaceous rocks by in situ hydrogeological tests
- ii. Chemical measurements
- iii. Diffusion experiments (section 1.3) (Jacques delay, 2006)

In this thesis, we focus on the diffusion experiments. A new in situ experiment is considered by Andra for the study of the radionuclide migration research (Diffusion RadioNuclide: DRN). The aim of this experiment are collect data on the migration of radionuclides, by means of experimental set-up as contrasting as possible with previous in situ studies. In a whole, the originality of the new in situ tests principally relates on:

- i. longer time-scale (over 10 years)
- ii. larger space scale (hundreds of mm)
- iii. In situ radionuclides migration monitoring device

In the following part, we will discuss about three main axes of development that concern the 3 candidate radiotracers, they consist of:

- **Dimensional design of in DRN experience via CFD and MCNP simulations**
- **Verification of the feasibility of beta and gamma drilling sensors**
- **Detailed design of radiation measurement equipment**

## 3.2 Calculation of dimensional design in DRN experience via CFD and MCNP simulations

### 3.2.1 Introduction

In order to optimize the dimensional design of DRN, we had to base our experiences at first on simulations, which consists of different steps as following:

#### **Step 1: CFD simulations made by CEA/L3MR**

The first step in dimensional calculations of DRN experience is developed via CFD simulations based on Alliance software (Montarnal, 2007). This calculation is based on solving the diffusive transport, taking into account radioactive decay and using the second law of Fick with sorption of the tracer according to the following equation (Crank, 1975):

$$\text{Equation 24} \quad \frac{\partial C}{\partial t} = \frac{D_e}{\varepsilon_a + \rho K_d} \nabla^2 C = \frac{D_e}{R \times \varepsilon_a} \nabla^2 C = \frac{D_e}{\alpha} \nabla^2 C$$

C: the concentration or activity per unit volume ( $\text{mol.m}^{-3}$ ) or ( $\text{Bq}^{-3}$ )

t: the time (s)

$D_e$ : effective diffusion ( $\text{m}^2 \text{s}^{-1}$ ),

$\varepsilon_a$ : porosity

$\rho$ : the density of the dry solid ( $\text{kg m}^{-3}$ )

$K_d$ : Liquid solid distribution coefficient ( $\text{m}^3 \cdot \text{kg}^{-1}$ ),

R: delay factor to the diffusion

$\alpha$ : anisotropy of diffusion

The objectives in CFD simulations are listed as following:

- **Predict decreased activity in solution and spatial extension of tracers into the rock**
- **Suggest injected solution volumes and activities, validate the test period**
- **Propose the geometry design of in situ monitoring system**
- **Provide 2D and 3D cartography in temporal or spatial activity profiles in order to integrate in MCNP simulations**

### **Step 2: MCNP simulations**

The 3D CFD modeling results give rise to a large amount of tetrahedral meshes with attributed activity during diffusion. In order to interpret these distributions (CFD distributions) into MCNP code, we developed an approach with consideration of approach introduced in previous chapter (2.4.2.3: CFD auto conversion algorithm). In a whole, the MCNP simulations were designed to verify the various parameters in design of final dimensional drilling and sensor monitoring system such as:

- **the detection ability to discriminate between two different diffusion time;**
- **the detection ability to discriminate between two diffusion coefficient (Anisotropy)**
- **the number and position of the crystals to be implanted;**
- **the length of the sensors;**
- **the distance of drilling sensor from injection borehole;**

## 3.2.1 CFD Simulations for geometry profile data and for parameter setting data

### **Simulation for geometry profile data**

- Gamma sensors

As revealed in the following figure (Figure 81), the reference modelling scenario is made of 3 set of gamma sensors placed inside sensor borehole with a distance of 50cm from injection borehole. This injection borehole contains the solution with radiotracers in contact with the mudstone. A parietal zone (green part in Figure 81) was included to account for the drilling that induced disturbed zone surrounding the boreholes. A void between the parietal zone and plastic Polyoxymethylene (POM) is supposed to be filled by poral water and the gamma sensors are put inside the POM.

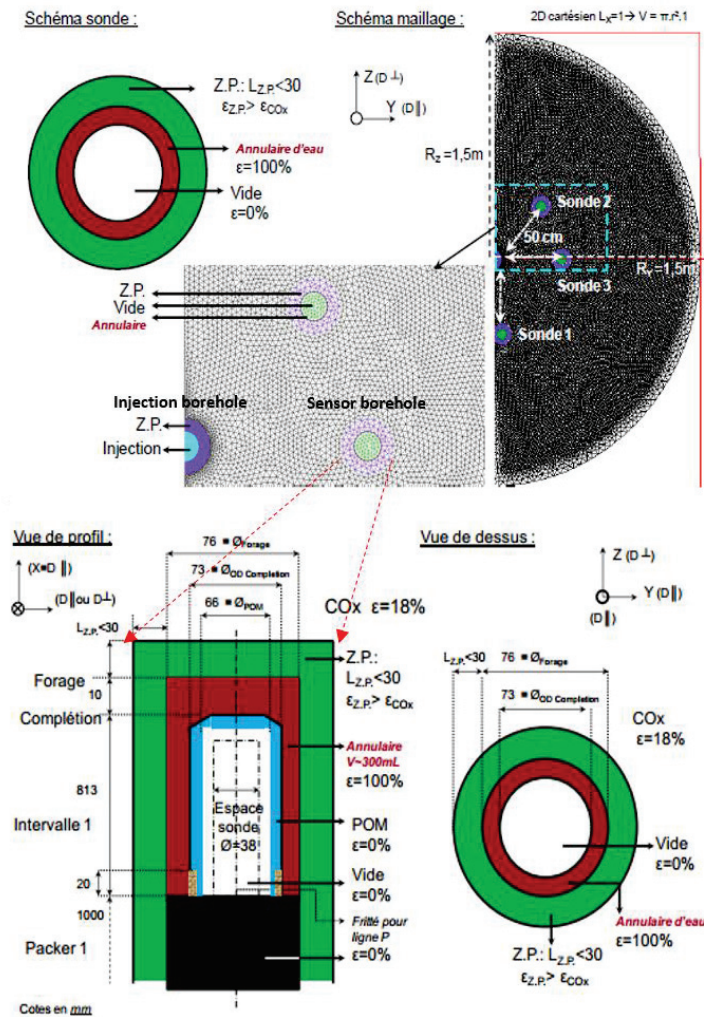


Figure 81:  $^{22}\text{Na}$  and HTO modeling scenario in DRN1202 drilling for dimensional calculations

- Beta sensors

Similar to gamma geometry profile, as showed in Figure 82, the modelling scenario was performed with beta monitoring sensor placed in one borehole inside the mudstone at a distance of 500 mm or 300mm from the injection borehole. This injection borehole contains the solution with radiotracers in direct contact with the mudstone as well. A parietal zone (green) was presented to account for the drilling that caused disturbed zone surrounding the boreholes. Differ from gamma geometry profile, a void between the parietal zone and the sensor is supposed to be filled by poral water and in contact with detection crystal via a stainless steel filter plate.

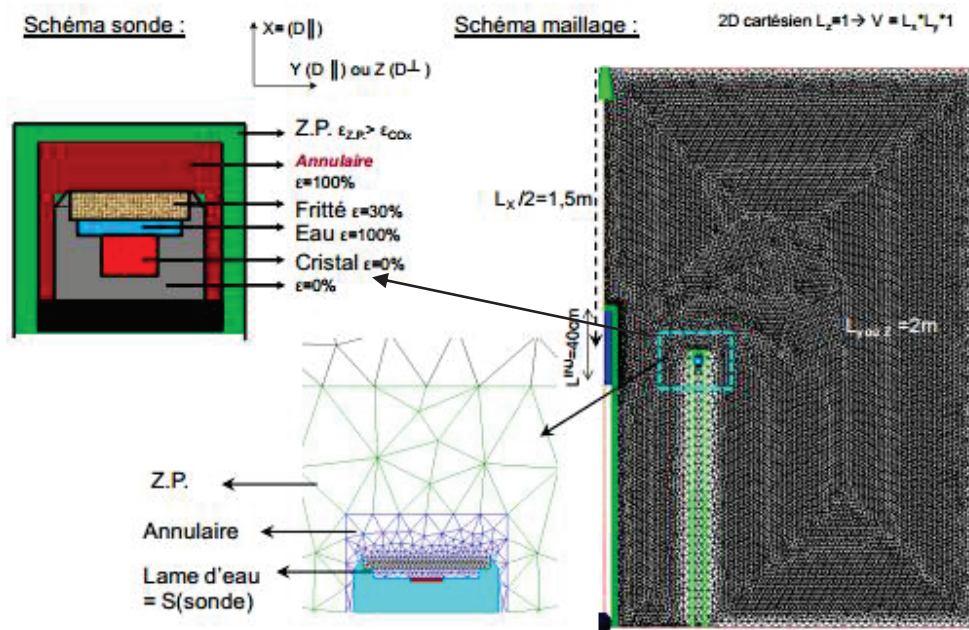


Figure 82:  $^{36}\text{Cl}$  and HTO modeling scenario in DRN1203 drilling for dimensional calculations

- Simulations for parameter setting data

Based on different parameters considered in Equation 24, we have listed the following parameters as reference simulation input value.

○ **Gamma sensors (HTO+<sup>22</sup>Na)**

**General data:**

Interaxial distance between injection and probes:	$r_i(\text{sondes})=0.5\text{m}$
Injection volume of solution:	$V(\text{Inj.}) = 10\text{L}$
Solution volume in the injection chamber:	$v(\text{Inj.})=4.53\text{L}$
Solution porosity in the injection chamber:	$\epsilon(\text{Inj.}) = V(\text{Inj.})/v(\text{Inj.})$
Simulation period:	$t=10 \text{ years}$

**HTO tracers data:**

Radiation decay: years	$T_{1/2}(\text{HTO}) = 12.33$
Effective diffusion in the clay COx perpendicular to the bedding $\text{m}^2.\text{s}^{-1}$	$D_e(^{22}\text{Na})=2.5*10^{-11}$
Anisotropy of diffusion in clay COx $a = D_{e\parallel} / D_{e\perp}$	$a(\text{HTO})=1.5$
Diffusion in water $\text{m}^2.\text{s}^{-1}$	$D_0(\text{HTO})=2.4*10^{-9}$
HTO porosity in the clay COx	$\epsilon(\text{HTO}/\text{COx})=0.18$
Delay factor to the diffusion	$R(\text{HTO})=1$
Adsorption on clay COX (no absorption)	$K_d(\text{HTO}/\text{COx})=0\text{L}/\text{Kg}$

**<sup>22</sup>Na tracers data:**

Radiation decay: years	$T_{1/2}(^{22}\text{Na})=2.6019$
Effective diffusion in the clay COx perpendicular to the bedding $\text{m}^2.\text{s}^{-1}$	$D_e(^{22}\text{Na})=4.8*10^{-11}$
Anisotropy of diffusion in clay COx $a = D_{e\parallel} / D_{e\perp}$	$a(^{22}\text{Na}) = 2$
Diffusion in water $\text{m}^2.\text{s}^{-1}$	$D_0(^{22}\text{Na})=1.27*10^{-9}$
$^{22}\text{Na}$ porosity in the clay COx	$\epsilon(^{22}\text{Na}/\text{COx}) = \epsilon(\text{HTO})$
Delay factor to the diffusion	$R(^{22}\text{Na})=6$
Adsorption on clay COX $\text{L}.\text{kg}^{-1}$	$K_d(^{22}\text{Na}/\text{COx})=f(R)$

○ **Beta sensors (HTO +  $^{36}\text{Cl}$ )**

**General data:**

Interaxial distance between injection and probes:	0.5 or 0.3 m
Injection volume of solution:	10L
Solution volume in the injection chamber:	30.4L
Solution porosity in the injection chamber:	30.4/10
Simulation period:	5 years

**HTO tracers data:**

Radiation decay:	12.33 years
Effective diffusion in the clay COx perpendicular to the bedding $\text{m}^2.\text{s}^{-1}$	$2.5*10^{-11}$
Anisotropy of diffusion in clay COx $a = D_{e\parallel} / D_{e\perp}$	1.5
Diffusion in water $\text{m}^2.\text{s}^{-1}$	$2.4*10^{-9}$

HTO porosity in the clay COx	0.18
Delay factor to the diffusion	1
Adsorption on clay COX	0L/Kg (no absorption)

**<sup>36</sup>Cl tracers data:**

Radiation decay:	$3.01 \cdot 10^5$ years
Effective diffusion in the clay COx perpendicular to the bedding	$4.5 \cdot 10^{-12} \text{ m}^2 \cdot \text{s}^{-1}$
Anisotropy of diffusion in clay COx $a = D_{e\parallel} / D_{e\perp}$	1.5
Diffusion in water	$1.27 \cdot 10^{-9} \text{ m}^2 \cdot \text{s}^{-1}$
HTO porosity in the clay COx	0.08
Delay factor to the diffusion	1
Adsorption on clay COX	0L/Kg (no absorption)

Both gamma and beta simulation scenarios are studied in varying one setting parameter from reference simulation parameters.

### 3.2.2 Introduction to CFD simulations in 2D and 3D

- **Gamma CFD simulations**

Initially, the CFD modeling is developed by CEA/L3MR in 2 dimensional. The initial objective of these 2D modeling scenario is explained as following:

- Assess the reduction in activity of solution and the spatial diffusion of radiotracers into the rock
- Estimate volumes and injected activities and define the test period
- Adapt a geometry for the detection in situ
- Plot the cartographies (example in Figure 83) and temporal or spatial activity evolution during different years (example in Figure 84) to evaluate the ability of sensors located around the injection borehole to measure the evolution of tracer clouds and detect the effects of parameter changes on these clouds

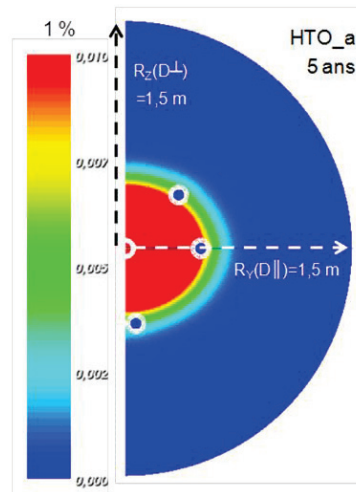


Figure 83: Simulation of HTO concentration cartography

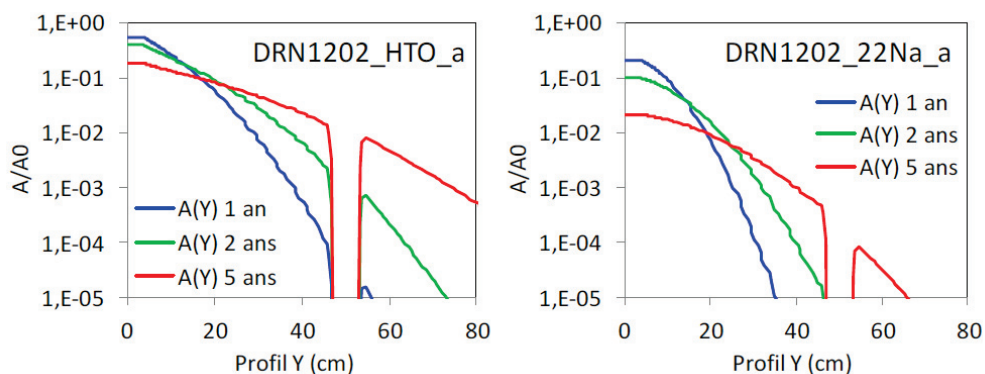


Figure 84: HTO (left) and  $^{22}\text{Na}$  concentration profile with different year's evolution

Although the information given by 2D modeling of radiotracers diffusion can be used for dimensional design in DRN experience, the global response of system must be found in 3D simulations. With 3D models, the additional Z axis helps to construct a solid mesh that can simulate the radiation counts received by the beta and gamma sensors, clarify the tracers diffusion in volume and test the effect of injection interval length ( $L^{INT}$ : in Figure 85).

Figure 85 shows a typical reference mesh geometry for the CFD simulations. As explained in previous chapter, each mesh is in tetrahedral form and full filled with tracer's concentration as illustrated in Figure 77. In both figures only one quarter of mesh are presented. A supplementary labview work is required to create a complete mesh in space with symmetric functionality.

Table 13 summarized 6 parameters used for the CFD calculations, then the results based on CFD calculations are used for MCNP6 simulation.

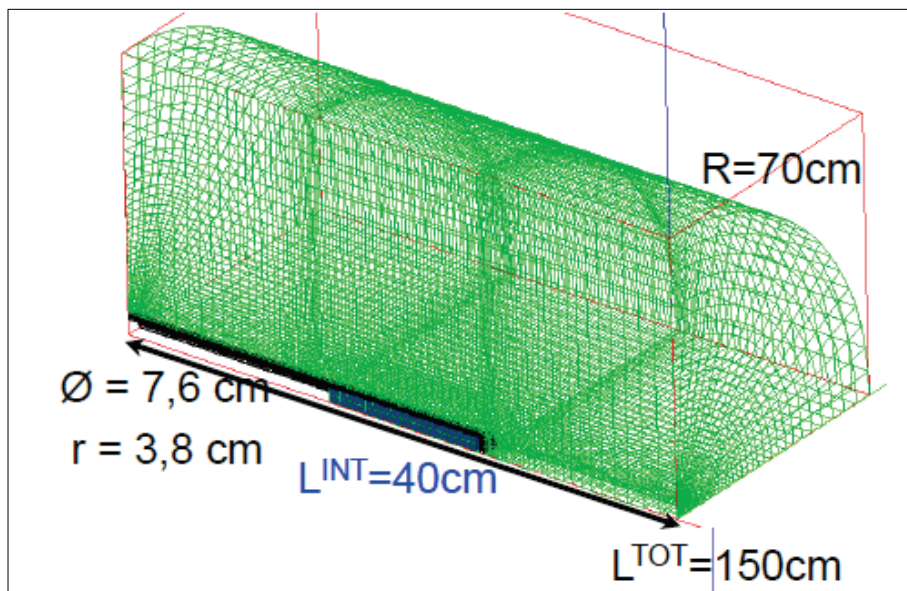


Figure 85: 3D mesh simulations used for  $^{22}\text{Na}$  injection tests

Parameters	Reference value (simulation S1)	Alternative parameter simulation (simulations S2 to S6)
Inter-axial distance between injection chamber and the 2 detectors located along the horizontal axis (Y) and along the vertical axis (Z)	0,45 m	-
The volume of water in circulation	5 L	3 L (S2)
Internal length of test	40 cm	15 cm (S5)
Effective diffusion coefficient of host rock Callovo- Oxfordian (COX), perpendicular to bedding	$De(^{22}\text{Na}) = 4,8 \cdot 10^{-11} \text{ m}^2 \cdot \text{s}^{-1}$	$De(^{22}\text{Na}) = 9,6 \cdot 10^{-11} \text{ m}^2 \cdot \text{s}^{-1}$ (S6) $De(^{22}\text{Na}) = 14,4 \cdot 10^{-11} \text{ m}^2 \cdot \text{s}^{-1}$ (S3)
Anisotropy diffusion of host rock of COX: $a = De_{\parallel} / De_{\perp}$	$a(^{22}\text{Na}) = 2,0$	$a(^{22}\text{Na}) = 3,0$ (S4)
Adsorption of the rock of COx and delay factor (R)	$K_d(^{22}\text{Na}/\text{COx}) = f(\text{R}) \text{ L} \cdot \text{kg}^{-1}$ $R(^{22}\text{Na}) = 6$	-

Table 13: Parameter setting in 3D simulations for  $^{22}\text{Na}$

### 3.2.3 The MCNP simulation of gamma sensors response under different radiotracers distribution

As cited previously, the CFD modeling has been done based on Alliance software by CEA/L3MR team. It studied the distribution of radiotracer diffusion during transport in porous media, first in 2D and then in 3D. My work was to assemble between CFD data that consists of radiotracer information and CAD data including basic experimental setup conditions into MCNP code. The conversion methodology was detailed and applied related on the chapter 2: 2.4.4.3. In geometry CAD setup part of MCNP6 simulation profile (Figure 79), all scale were kept the same as in CFD simulation profile (Figure 81), meanwhile a little differ was existed. Parietal zone was eliminated for the reason that it has already been considered as coefficient of anisotropy parameter in CFD simulations. Thus 2 set of sensors (Figure 79: bottom left part) installed in two sensor boreholes that are parallel and perpendicular to bedding had to be taken into account to monitor anisotropy effect. Each sensor consists of 4 crystal (Figure 79: top part). In radiotracer injection borehole, liquid injection circulation object was implanted that inducted a head in front of injection borehole (Figure 79: bottom right part). All objects originates from CAD data were built via tetrahedral meshes (Figure 79: bottom right part). CFD data outcome a 3D radiotracer cartography (Figure 78), and anisotropy diffusion of radiotracer can be identified. Then CFD plus CAD data were studied (Figure 80).

In this paragraph, we exploited the results obtained from MCNP6 simulations, it allow us to calculate the signal receive from different crystals using tally F8 in MCNP data card (Chapter 2: 2.4.3.3). Our simulations were based on different CFD simulation results that gave us information about radiotracer distribution. Under reference CFD simulation condition (Table 13: S1) , the total signal received by the 4 crystals located in the horizontal plane (Y) increases during the first 6 years and then returns to its initial value (10 years) . Along the vertical plane (Z), however, the total signal received by the

detector remain almost constant, with a progressive decrease (Figure 86: Top part). The minimum count values (CPS) obtained with each crystal ranging between 1.78 and 2.09 CPS after 10 years are (Figure 86: Bottom part):

**Crystal 1: 1.78 CPS**

**Crystal 2: 2.09 CPS**

**Crystal 3: 2.04 CPS**

**Crystal 4: 1.82 CPS**

These values are higher than the detection limit determined at 1cps with 1h of accumulation time (Hautefeuille, 2014). Thus, we can expect a significant signal on all the crystals continuously during 10 years observations.

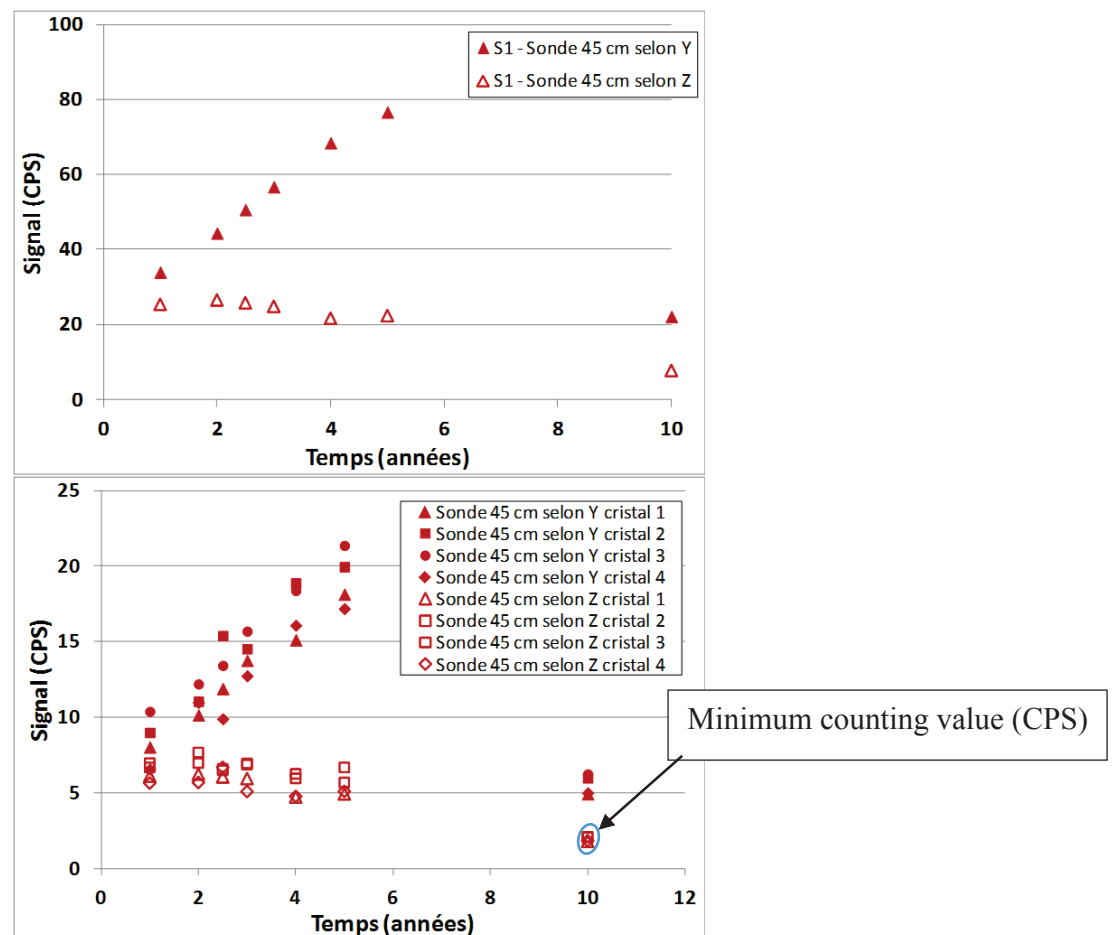


Figure 86 : Sum of 4 crystals count rate on each axis (Top part), each crystal count rate on each axis (Bottom part) (S1: Reference simulation)

Based on different parameter setting results in Table 13, S2 starting from the variation in water volume in injection circuit, it changed from 5L to 3L that can induce around 20% higher values of the total received signal by the crystals located in the horizontal plane (Y) compared to the reference simulation, but it does not significantly change the values received by the crystals located in the vertical plane (Z) (Figure 87).

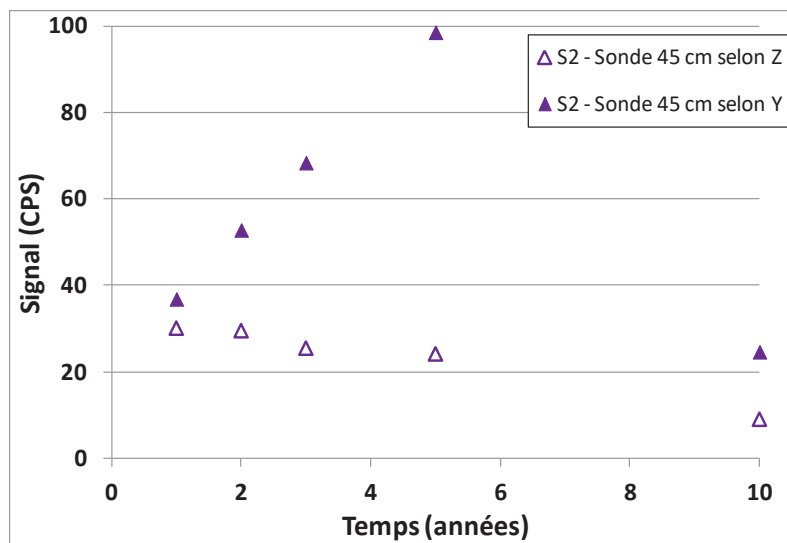


Figure 87: Sum of 4 crystals count rate on each axis (Simulation S2)

An increase of the diffusion coefficient (by a factor of 3) dramatically enhanced the total signal level, especially on the Y-axis between 3 and 4 years that presents around (500CPS) 5 times higher than the reference simulation (S1: 80 CPS Y-axis). On the other hand, the crystals positioned along the Z axis reached a maximum count rate (about 100 CPS) toward the 5th year (Figure 88).

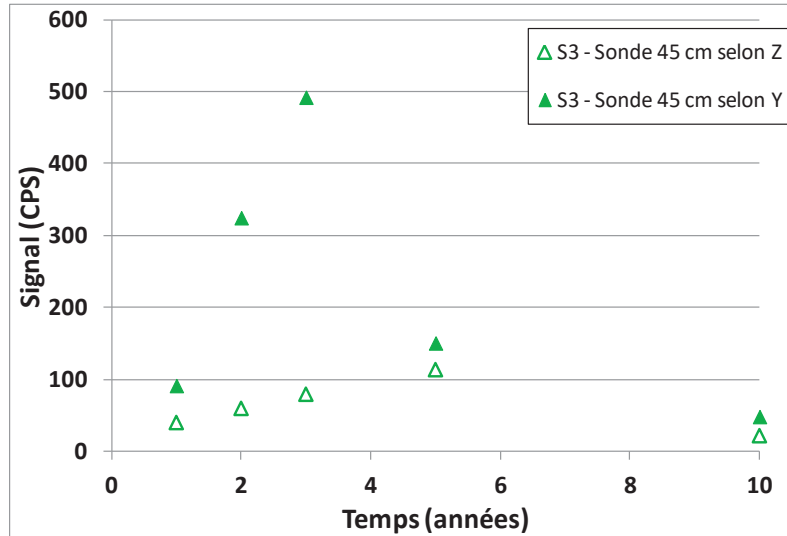


Figure 88: Each crystal count rate on each axis (Simulation S3)

The research on influence of anisotropy factor has been simulated (Figure 89). The maximum count rate along one axe (Y) is found at around 6 years, meanwhile some more results after 6 years' diffusion had to be analyzed. Compared with reference simulation (S1: CPS 80, anisotropy=2), the maximum in simulation S4 (CPS 120, anisotropy=3) is higher as well.

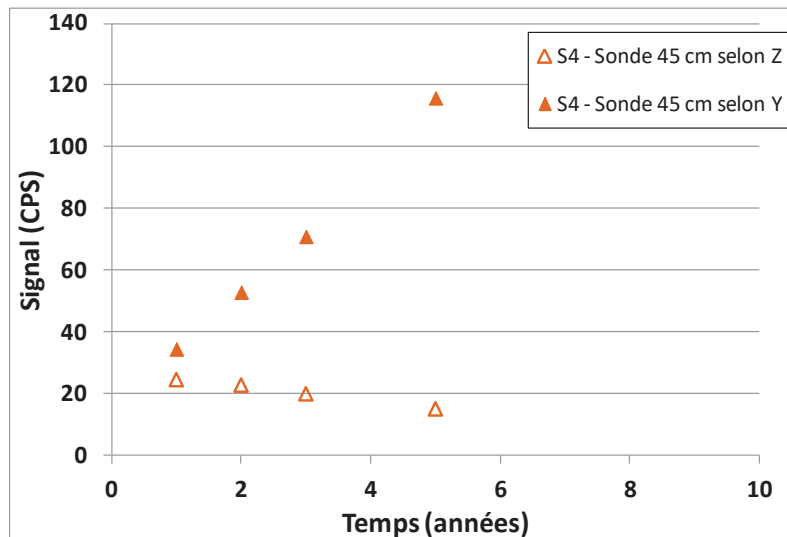


Figure 89: Sum of 4 crystals count rate on each axis (Simulation S4)

The simulation S5 have reduced the internal length of injection solution around 2.7 times compared to reference, passing from to 40cm to 15cm. We have marked that the significant decrease of count rate ranging from 80 CPS (S1) to 47 CPS (S5) (Figure 90).

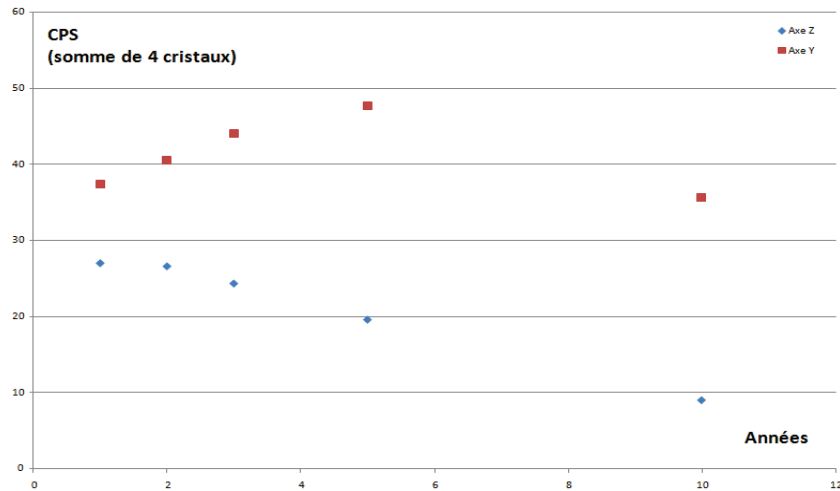


Figure 90: Sum of 4 crystals count rate on each axis (Simulation S5)

We complete the simulation part with the study of diffusion coefficient. The diffusion coefficient increased by a factor of 2 (S6) compared reference simulation (S1) shift the instant of detection of radiotracers with earlier appearance of maximum count rate at around 3 years instead of 5 years calculated in reference simulation (Figure 91) and also give a dramatic increase of count rate (S6:250CPS, S1: 80CPS) .

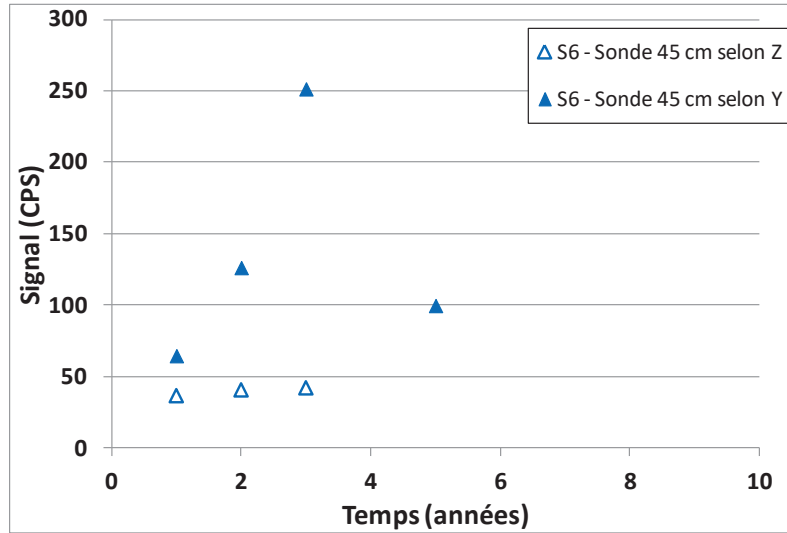


Figure 91: Sum of 4 crystals count rate on each axis (Simulation S6)

For a better understanding about MCNP simulations we compared the results coming from S3, S6 and S1 as showed in Figure 92. We reported the changes in diffusion coefficients (by a factor of 3 (S3) and by a factor of 2 (S6)). On the Y axis, it is still observed an important increase of the signal on the early 3 years, while the maximum signal is found around 5 years for the reference simulation. To be noted that no earlier detection of radiotracers are appeared between S3 and S6, although a difference of diffusion coefficient are existed. From this observation, we can consider that a high factor of diffusion coefficients give more variations in sensor detection signals rather than shifting time in detection of radiotracer.

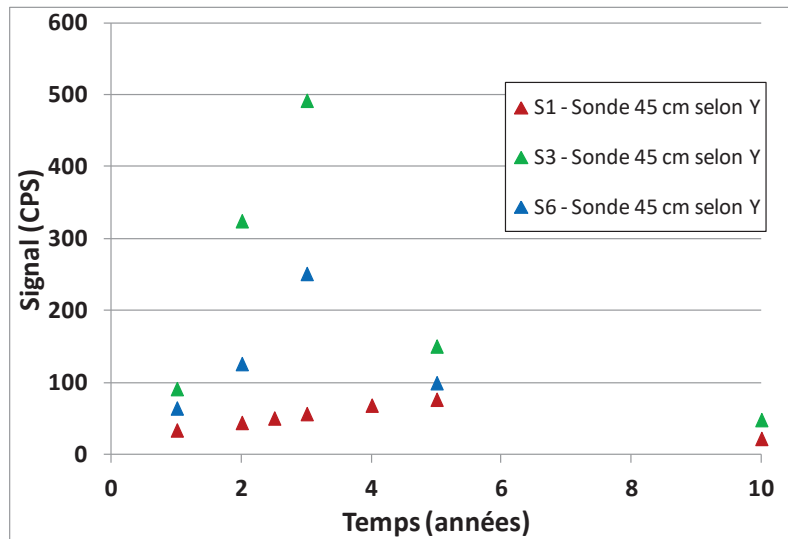


Figure 92: Evolution of the count rate according to the axis Y with different diffusion coefficient

Concerning the anisotropy simulations (S4 anisotropy @4 and reference @3), the signals vary a lot (superior to LD @ 1 CPS) on crystals oriented along the Y axis in the early years, whereas the trend is reversed along the axis Z (Figure 93). This simulation therefore shows that the system is actually sensitive to the anisotropy of host rock.

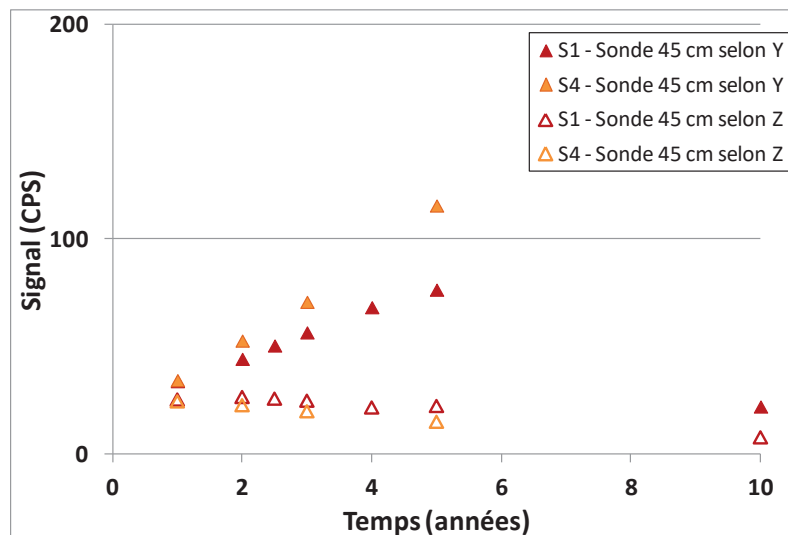


Figure 93: Evolution of the count rate according to different axis Y and Z with different anisotropy

### 3.2.4 Conclusion

We had studied a set of simulation results in varying different parameters setting under geometrical condition that the sensor borehole is placed 45 cm away from injection borehole. We can extract useful information as follows:

- One sensor composed of 4 crystals can expect to detect the diffusion of radiotracer  $^{22}\text{Na}$  continuously during 10 years monitoring;
- Our sensors are possible to discriminate between the different diffusion coefficient that is multiplied by a factor of 2 or 3 for example;
- Our sensors are sensitive to the anisotropy of host rock as well;
- The requirements in placing the sensor close near the injection drilling is favorite. This would guarantee the detection of tracer's diffusion in various directions as early as possible;

Lastly, these modelling results (CFD+MCNP) led us to propose the final geometrical design of in situ Gamma and beta monitoring system as illustrated in Table 14 and Figure 94.

Design element	Selection reference	Argument
Drilling length	$\leq 10$ m	The pressure measured at the depth of 9.20 m in the DRN1221 drilling is greater than 47 bar
Interaxial distance between the injection chamber and the two detectors S1 and S2 located along the horizontal axis (Y) and along the vertical axis (Z)	The nearest < 0,40 m (Y) < 0,35 m (Z)	The need to place the detector close to injection drilling to detect the tracers as early as possible
Volume of water for the injection circuit	3 L	Satisfactory compromise on intensity signal received by the detectors, followed by the fluid and radiation protection
Length of the test interval	40 cm	Satisfactory compromise on detection count received by the detectors and radiation protection 4 crystal receive similar count rate: redundancy and accumulation possible

Table 14: Proposition for  $^{22}\text{Na}$  and  $^{36}\text{Cl}$  dimensional design

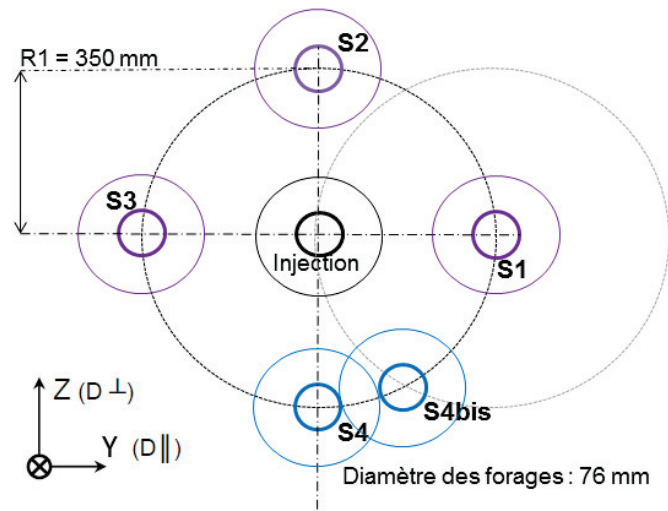


Figure 94: Considered geometries for the injection of  $^{22}\text{Na}$  and  $^{36}\text{Cl}$  in situ test

### 3.3 Validation of high sensitivity gamma and beta sensors for the tracers injection of $^{22}\text{Na}$ , $^{241}\text{Am}$ and $^{36}\text{Cl}$

As stated before, our in situ Diffusion RadioNuclides (DRN) experiments consists of the detection of different tracer's diffusion in situ by means of sensors located in peripheral boreholes. To this aim, in this section, we evaluated the performance of both beta and gamma sensor system. This included optimization of the design, characterization of sensitivity, limits of detection (L.D). To be detailed, this will be presented as follows:

- Design of in situ beta detection system;
- Calibration of beta sensor from  $^{36}\text{Cl}$  solution;
- Determination of beta sensor sensitivity and L.D from  $^{36}\text{Cl}$  solution;
- Design of in situ gamma monitoring system;
- Calibration of 4 gamma sensors at 511Kev prepared for  $^{22}\text{Na}$  tracer injections;
- Validation of the  $^{241}\text{Am}$  at low energies (principal at 60Kev) and determination of the stopping power in case of host rock at energy range of  $^{241}\text{Am}$  and  $^{22}\text{Na}$ ;

Secondly, we evaluated our Monte Carlo approach (MCNP) to simulate radiation transport that help us to

- The beta design decision
- The review of host rock compositions that cited in E.Gaucher article (Gaucher, 2004)
- The determination of the gamma attenuation coefficient in Callovo-Oxfordian milieu for different radioelements

### 3.3.1 In situ Beta detection sensor system

#### 3.3.1.1 Beta sensors design and performance

##### 3.3.1.1.1 The design of in situ beta sensor system:

In terms of beta particles detection sensor system (system inside the sensor borehole), the well-known beta detection methodology is liquid scintillation counting which is an indirect fluorescence counting system used to quantify the activity of samples emitting beta and alpha particles (Staff., 2004). Such a method cannot be applied for direct continuous and in-situ detection, as required for this project. The traditional in situ beta monitoring methodology is to use scintillation sensors in order to investigate in a fast and simple way to measure beta activity (Miramonti, 2002). Fiber-optic sensors (FOSs), consisting of a scintillator, optical fiber and light-measuring device, have been applied widely for radiation measurements (Beddar, 2001). FOSs cannot be used for our application because one key point of the project is to limit the detection volume (Figure 95: liquid chamber @ 1.4mL ( $\varnothing \times L = 30 \times 2 \text{mm}^2$ )), to avoid any perturbation of the  $^{36}\text{Cl}$  diffusion. In order to detect the diffusion plume as soon as possible, YSO scintillator ( $\text{Y}_2\text{SiO}_5: \text{Ce}$ ) has been selected instead of plastic scintillator for both its high scintillation efficiency better than plastic scintillator with a light yield about 25-30% of NaI(Tl) and its better mechanical ruggedness regarding the experiment conditions (the experiment taking place at -490m, pressure applied on the detector face is  $\approx 40\text{atm}$ ).

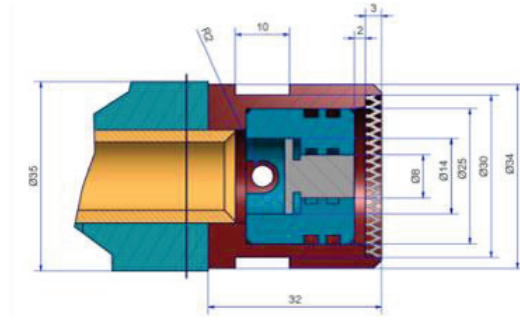


Figure 95: Main component of the beta sensor (top) and the complete design of the beta sensor with its mechanical part (bottom)

The mainly objective of Beta experiments is to determine the sensitivity of sensors and its detection limits. The sensitivity depends on the ratio of beta detection signals to the noise detection signals (SNR). The detection limits are related to the acquisition time. Once the interaxial distance between monitoring and injection boreholes is fixed, two options are available to optimize the detection of diffusing species. One is to increase initial concentration of  $^{36}\text{Cl}$ , and the other is to improve the sensitivity of the sensor. In this thesis, we have focused on the latter, i.e. by optimizing the size of the YSO crystal and liquid chamber volume. Figure 96 illustrates two designs of beta detection crystal. Both designs display a cylindrical crystal and a photo detector made from SiPM (Sensl UFC 60035) glued on one side of YSO crystal. On the other side, the crystal is in contact with 2 mm of the solution sample ( $^{36}\text{Cl}$ ) to analyze. The difference originates from the size of detection crystal YSO. Figure 96 right part shows the YSO design (10 mm thickness) for the first series of beta measurements and in the left part represents the

small size YSO crystal with 0.5mm thickness with the rest of detector length replaced by Boro Silicate.

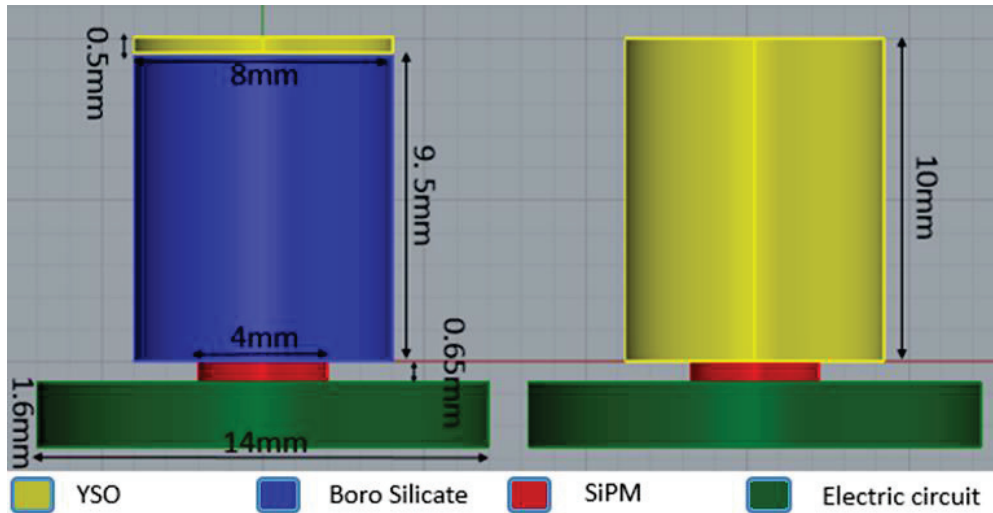


Figure 96: Crystal design for Beta sensors (Beta 2 left, Beta 1 right)

### 3.3.1.1.2 The measurements of two beta sensors sensitivities

The whole measurement setup is pictured in Figure 97 including beta sensor, flow chamber and calibration set up. The  $^{36}\text{Cl}$  standard solutions at 2.08, 22.5, 243, 1596 Bq/ml are circulated using a pump through the flow chamber containing the sensor. The electronic acquisition consists of a set of amplifiers & signal processors and communication system (CAN Bus).

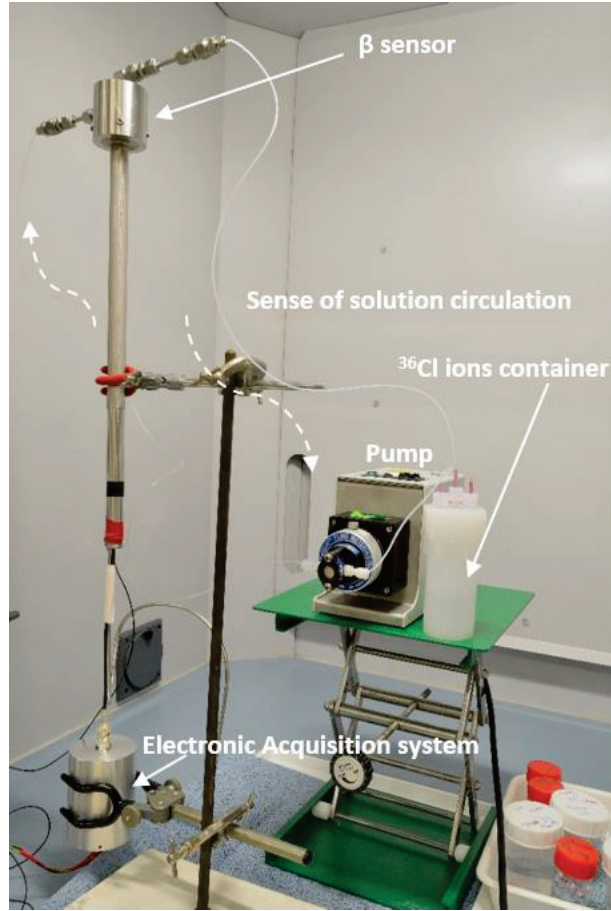


Figure 97: Experimental measurement setup for calibration of  $^{36}\text{Cl}$  solution

The following two sensors measurements are expressed in counts per minute (CPM) for the total counts and net counts (Total counts- noise counts) in Table 15. The statistics are elaborated in Poisson approximation (Chapter 2: Statistics for data analysis) and calculated at 2 sigma (confidence level at 95%). Sigma has been minimized by increasing the number of equal counting times (every minute). The calculation process is introduced in chapter 2: Equation 15 with a improve factor of  $\sqrt{N}$  . The net CPM that only related to the activity sources is calculated by a subtraction of measurements counts to the noise counts.

At first, it is obvious that the massive YSO crystal detector (Beta 1) records higher dark counts than a thinner one (Beta 2). (8.94 CPM compared to 1.21 CPM) This observation is again in good agreement with previous MCNP simulation estimation.

<b>Activity of solution <sup>36</sup>Cl (Bq/mL)</b>		<b>0(Water)</b>	<b>2.08±0.2</b>	<b>22.5±0.2</b>	<b>243±2</b>	<b>1596±16</b>
<b>Number of measurements of one minute (N)</b>	Beta 1	98	19	36	37	36
	Beta 2	678	41	73	31	25
<b>Mean value of CPM Measurements (N<sub>D</sub>)</b>	Beta 1	8.94 (Noise count: N <sub>B</sub> )	8.47	11.6	30.5	143
	Beta 2	1.21	1.51	5.64	52.4	334
<b>±2σ<sub>N<sub>D</sub></sub> (CPM)</b>  <b>(σ<sub>N<sub>D</sub></sub> = √N<sub>D</sub> / √N)</b>	Beta 1	±0.60	±1.34	±1.13	±1.82	±4.0
	Beta 2	±0.085	±0.38	±0.56	±2.6	±7.3
<b>Mean value of net CPM (N<sub>D</sub>-N<sub>B</sub>)</b>	Beta 1	0	0	2.86	21.6	134
	Beta 2	0	0.3	4.43	51.19	332.79

<b><math>\pm 2\sigma</math> (CPM net)</b>	Beta 1	$\pm 0.60$	$\pm 1.47$	$\pm 1.28$	$\pm 1.92$	$\pm 4.04$
$(\sigma = \sqrt{\sigma_{N_B}^2 + \sigma_{N_D}^2})$	Beta 2	$\pm 0.085$	$\pm 0.39$	$\pm 0.57$	$\pm 2.6$	$\pm 7.3$

Table 15: Measurements using beta 1 with standard solution

The performance of the beta monitoring sensors were calibrated using 4 standard solutions. Then, two unknown solutions were studied. Both sensor designs presented previously were tested. Results of the measurements are plotted in Figure 98 as direct curves with slope corresponding to sensitivity, plus a constant term corresponding to noise level. In Figure 99, curves plotted after subtracting noise value for each measurement, correspond to a constant term close to zero with nearly the same sensitivity (slope) as in direct calibration curves.

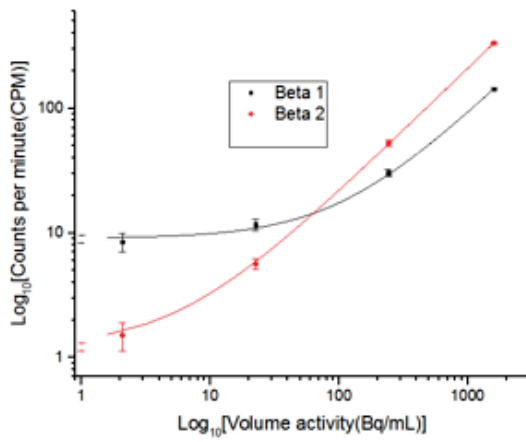
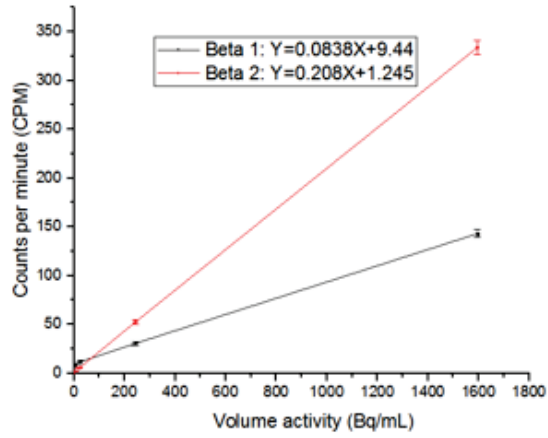


Figure 98: Calibration curves of beta detection sensors including background noise counts

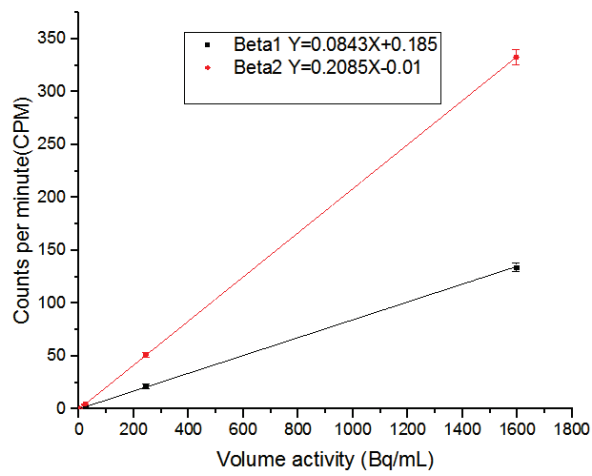


Figure 99 : Calibration curves of beta detection sensors after subtraction of background counts

Meanwhile, contrary to MCNP simulation results (Figure 105), it can be seen that beta 1 sensor has a lower sensitivity than beta 2 sensor. The main explanations are as following: Firstly, our parameters adjustments for beta sensors were based on getting the optimal SNR. As a result, in order to reduce the noise counts, beta 1 sensor had to be adjusted to a higher energy trigger level than beta 2 sensor to compensate the effect of increasing crystal thickness which would introduce higher energy dark counts, typically gamma dark counts. These different parameters setting for beta sensors gave the principal reason that we loss sensibility from Beta 1. Secondly, due to limited time of access to the liquid beta tracer solution, both beta sensor parameters had to be adjusted using a  $^{133}\text{Ba}$  sealed gamma source. Meanwhile, it has been proved in Figure 100 that beta 2 exhibited a much better SNR compared to beta sensor 1 what allowed us to validate our geometry crystal design. Our results also confirmed the MCNP simulation results about the influence of crystal thickness on the SNR value (Figure 105).

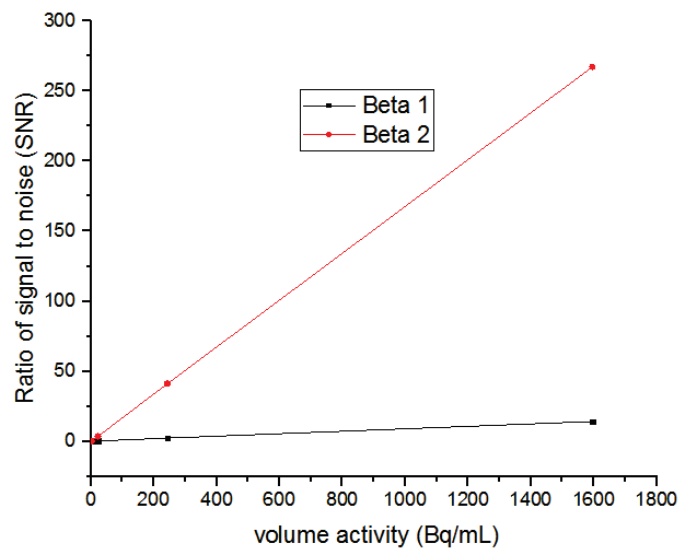


Figure 100: Comparisons of SNR for beta sensors in response of standard  $^{36}\text{Cl}$  solution

Concerning unknown solutions, the results obtained with Beta 2 sensor and listed in Table 16.

	S1	S2
CPM total	12.3	49.4
Number of equal counting time intervals	20	20
Variance: $\pm 2\sigma$	$\pm 1.65$	$\pm 3.22$
Determination of unknown activity(Bq/mL)	$53.15 \pm 7.93$	$231.5 \pm 15.5$
Activity measured by liquid scintillation (Bq/mL)	48.6	225.7

Table 16 : The determination of two unknown solutions

Activities measured by liquid scintillation are given within less than 1 % error. The agreement between two set of activity values validate the calibration equation for beta sensor, while it is evident that increasing the statistical measurement time will reduce incertitude on value of activity.

Up to now, all the measurements were performed in laboratory, while the real final tracers' injections are conducted at around 490 meters underground. Since the noise level would not be the same, the Callovo-Oxfordian argillite noise counts have been conducted (Figure 101).

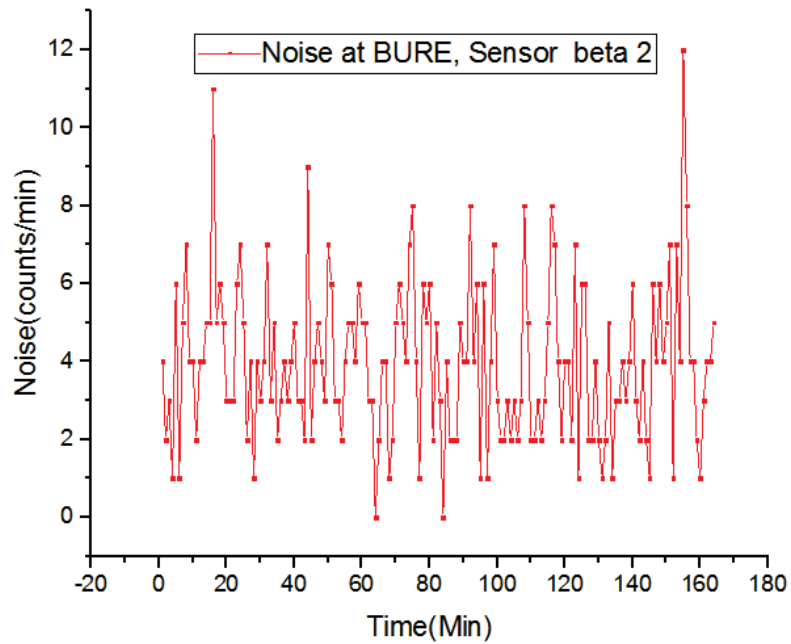


Figure 101 : Noise measurements using beta 2 sensor in the argillite milieu

The average of noise count is around 4.04 CPM. The noise level at Andra Callovo-Oxfordian milieu is larger than ambience measurement due to the large presence of  $^{40}\text{K}$  in Callovo-Oxfordian argillite (E. Gaucher a, 2004). The sensor beta 2 has been installed in a prototype borehole at the site of the final experiment. At this stage, the sensor was not equipped with fluid circulation.

In combination of sensor sensitivity determined in laboratory and noise level measured in situ, the final calibration function for beta 2 sensor was expressed as follows:

$$\text{Beta 2 sensor: } Y = 0.208X + 4.04$$

### 3.3.1.1.3 Limits of detection

As previously cited, another objective of beta experience is to study the limits of detection. The limits of detection evaluates the minimum detectable amount of a source that can be reliably differentiated from the background counts. Some theoretical equations have been developed to determine the minimum detectable activity (MDA). One is in a traditional way by using Currie equation (F.KNOLL) (presented previously in chapter 2 section 2.3)

We considered a range of low activity solutions (0(Water), 2.08Bq/ml, 22.05Bq/ml) at real conditions (Figure 102).The value collected cannot differ for both of sensors  $^{36}\text{Cl}$  at 2.08Bq/mL from the background within 2 sigma (95% confidence). Whereas, at 22.5 Bq/mL, the sensor beta 2 gave a significant value, while it was not the case for beta sensor 1.

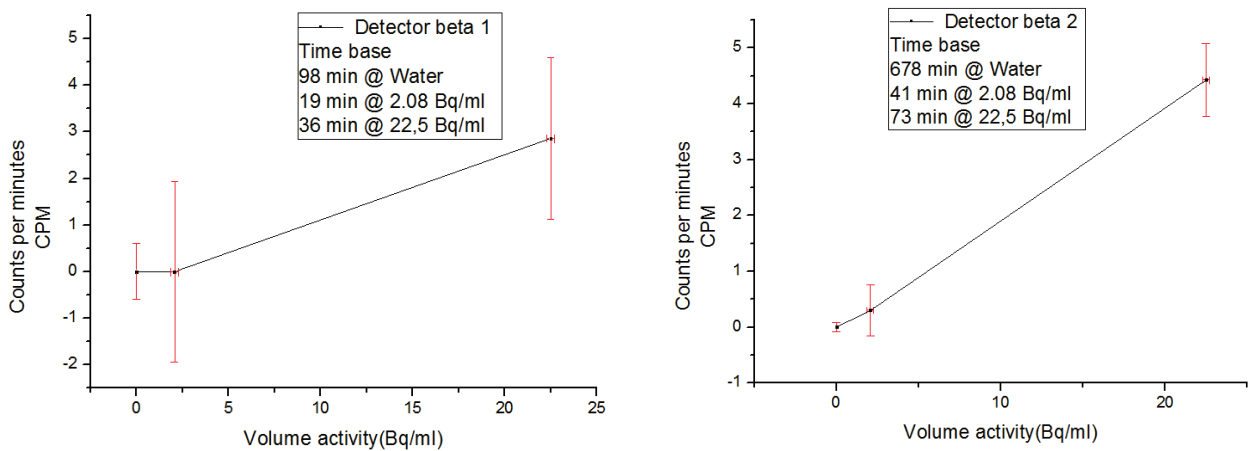


Figure 102 : Comparison of net counts CPM as a function of volume activity for beta sensors

Estimation of minimum detection limits has been perforated by (i) Currie equation (ii) 20 sigma protocol. From Table 17, beta 2 sensor give a better minimum detection limits level (3.101 in Currie theory and 0.85 in 20 sigma method) compared

beta 1 sensor (5.496 in Currie theory and 6 in 20 sigma method). This difference from Currie theory to real measurements is mainly due to the constant factor (2.706) in the equation. The value is deducted by the assumption that the net count is relatively inferior to the background counts ( $N_D \ll N_B$ ): in our case, because of 3.101 ( $N_D$ ) is not inferior to 1.21 ( $N_B$ ), the Currie equation is not adapted. To use this equation properly, more accumulation time has to be considered.

	Noise CPM ( $N_B$ )	Number of measurement of one minute (N)	$\sigma_{N_B}$ ( $\sqrt{N_B} / \sqrt{N}$ )	Currie theory	20 sigma
<b>Beta 1</b>	8.94	98	0.30	5.496	3.101
<b>Beat 2</b>	1.21	678	0.0425	6	0.85

Table 17: Calculation of sigma and detection limits in 2 methodologies

Table 18 summarize the detection limits via 2 approximation theoretical ways for different accumulation times (1h and 24h). Supposing the measurements are taken every minute, we are able to decrease the sigma value by a factor of  $\sqrt{N}$ . The sigma values are calculated by  $\sigma = \sqrt{N_D} / \sqrt{N}$ . ( $N_D$  represents the mean value of noise and N is times of measurements for each minutes (For 1H:  $N=60$  and 24H:  $N=24*60=1440$ ). We can conclude that at a certain low accumulation time, the limits of detection with  $20\sigma$  method display give higher significant count value than using Currie equation: this can guarantee a large margin upon the background noise. For longer time acquisitions (@ 24h), the values obtained from the two methodology converges. Finally, we can summarize that for a short time measurement, it is preferred to use 20 sigma method, to be sure that the detection count comes from radiation source. Then for a long time measurements, the standard Currie equation could be implanted.

	Sensitivity of solution $^{36}\text{Cl}$ (CPM/Bq/ml)	Noise ANDRA in CPM	$\sigma_{N_B}$ ( $\sqrt{N_B} / \sqrt{N}$ ) @1h	$\sigma_{N_B}$ ( $\sqrt{N_B} / \sqrt{N}$ ) @24h	DL (CPM @1h)	DL (CPM @24h)
<b>Beta 1</b>	0.0838	53.77	0.95	0.193	60.8	57.36
<b>Beta 2</b>	0.208	4.04	0.26	0.053	7.93	6.99

Table 18: Determination of noise sigma and D.L @1h and @24h

### 3.3.1.2 Beta simulation studies

#### 3.3.1.2.1 Design of beta detection via simulation

The principal criteria in the design of beta sensor are the volume in the liquid chamber that optimize detection efficiency and the size of crystal that offers the better signal to noise ratio (SNR) (Abmed, 2007) . These two criteria have been simulated using Monte Carlo N-Particle transport code (MCNP). The geometry profile data for MCNP code as showed in Figure 103 includes only two objects, the detection crystal and the solution. The variables for the simulations are the thickness of the YSO crystal and the volume of  $^{36}\text{Cl}$  solution. The diameter of YSO crystal and of solution are fixed at 8 mm and 30 mm respectively regarding to chamber mechanical constraint.

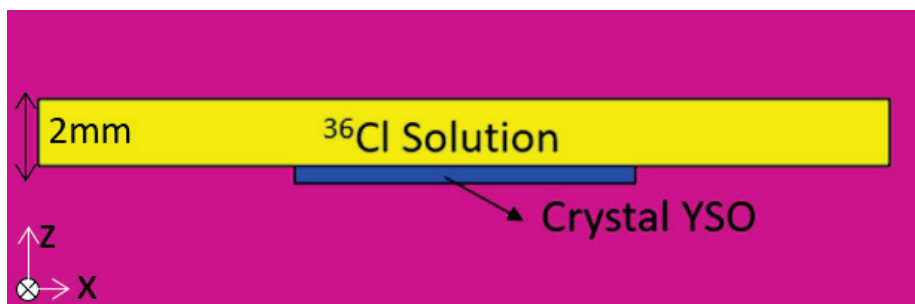


Figure 103: Scheme of geometry used for MCNP simulation

Base on this geometry, we studied the influence of different thickness (x) of solution  $^{36}\text{Cl}$  in response to detection efficiency. This detection efficiency has been simulate as the percent probability of beta particles that can be absorbed (or detected) by YSO crystal; the solution volume is modeled as a cylinder volume with a fixed diameter.

Simulations state that the path of  $^{36}\text{Cl}$  in water is limited at approximate 2mm (Figure 104). In other words, it means that given a concentration of  $^{36}\text{Cl}$ , the detections of beta radiations is revealed with optimal efficiency at 2 mm thickness path of  $^{36}\text{Cl}$ .

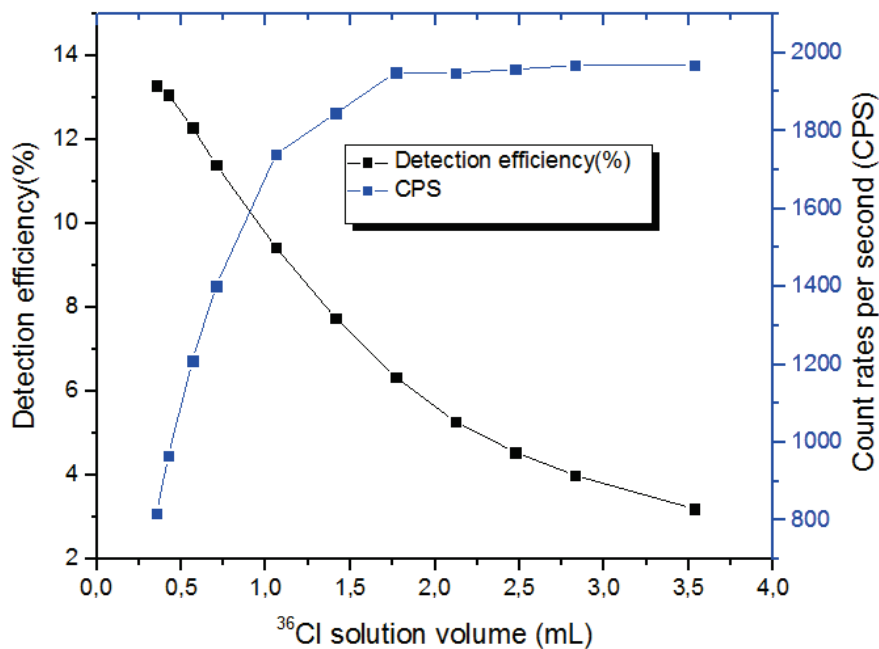


Figure 104 : Variations of detected activity (in count per second) and of detection efficiency in response to different volume of  $^{36}\text{Cl}$  solution

As reported in the introduction part, it is known that the bigger the crystal is, the more signal the detector will receive, although it can take more noise too, typically will be more sensitive to gamma radiation from nature. So it is important to find a compromise where the radiation sensor can achieve a optimize factor of signal to noise (SNR). In the Table 19, total detection (counts per second) is obtained from simulation

results; the noise level is supposed directly proportion to the thickness of crystal by a factor 10 (0.1mm to 1CPS for example). The signal counts increase much slowly compared to the noise: the thinner the crystal, the better the ratio signal to noise. Figure 105 illustrates that the increase in detection efficiency leads to the decrease in SNR with the crystal size. It is assumed that the noise is directly proportional to the size of crystal. The net signal count increases slowly compared to the noise count. The main conclusion is that a better SNR will be obtained using a crystal as thin as possible.

<b>Z(Crystal) ( mm)</b>	<b>Total detection (CPS)</b>	<b>Noise detection (CPS)</b>	<b>Ratio Signal/Noise)</b>
<b>0.1</b>	3.12	1	3.12
<b>0.3</b>	3.25	3	1.08
<b>0.4</b>	3.32	4	0.83
<b>0.5</b>	3.39	5	0.68
<b>1</b>	3.69	10	0.369
<b>3</b>	4.77	30	0.16
<b>5</b>	5.51	50	0.11
<b>7</b>	5.97	70	0.085
<b>10</b>	6.46	100	0.065

Table 19 : The variations in CPS of signal to noise ratio under different crystal length

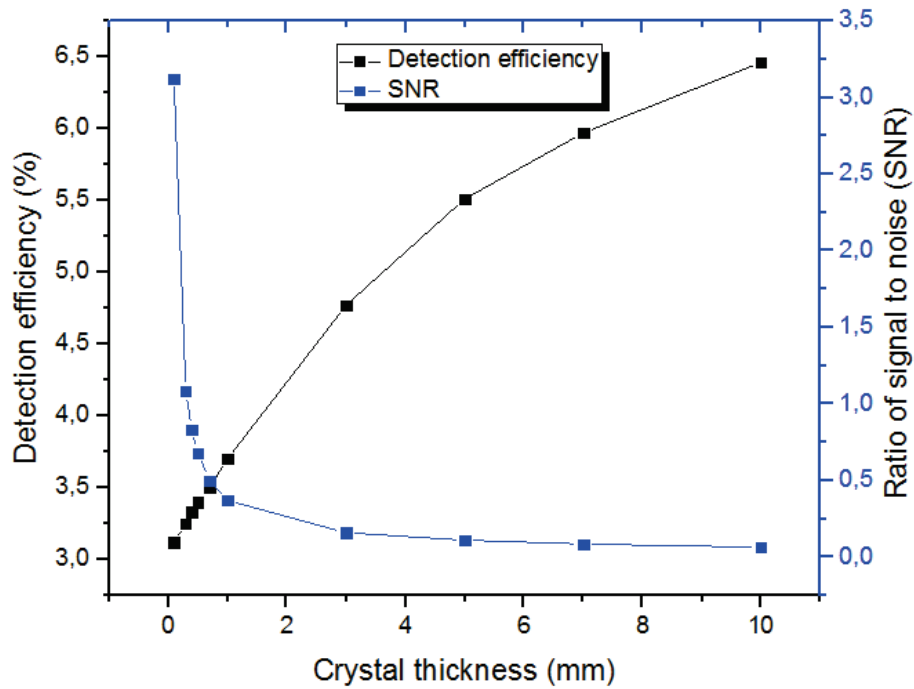


Figure 105: Variations of signal to noise ratio (SNR) and detection efficiency depending on crystal thickness

Finally, the optimization parameters via simulations are proposed to be around 1.4mL of  $^{36}\text{Cl}$  solution and a thickness of crystal as small as possible. These simulation results are consistent with the design of Beta 2 sensor which has  $25.13\text{mm}^3$  ( $\text{Ø}\times\text{L}=8\times 0.5\text{mm}^2$ ) of crystal and 1.4mL ( $\text{Ø}\times\text{L}=30\times 2\text{mm}^2$ ) solution. Thus for the experimental measurements, it is confirmed that the Beta 2 sensor would give the optimum detection sensitivity and detection limits.

### 3.3.2 In situ Gamma detection sensor system

#### 3.3.2.1 : Gamma sensor design and performance

##### 3.3.2.1.1 Specific design of Gamma detectors

In gamma-ray measurements, use of semi-conductor such as (Ge(Li)) give rise to an excellent energy resolution and good detection efficiency (P. N. Luke). Meanwhile for some constraint using of semi-conductor (laboratory large scale and cooling system), it is not allowed to be adapted in our situ detection system. Instead, use of scintillation sensors give a simple and efficient monitoring system, with an energy resolution of 29 keV for  $^{137}\text{Cs}$  in NaI (3x3 inches) compared to 0.8KeV for  $^{137}\text{Cs}$  in HPGe (NSSEP, 2017). Normally, it is expected to set-up a large size of scintillator to obtain a better energy resolution performance, nevertheless the scintillator is designed to be at 1x1 inch (2.54 x 2.54 cm<sup>3</sup>) in cylinder form due to the size of sensor borehole ( $\text{Ø}=76\text{cm}$ ). The following figure (Figure 106) compares the energy resolution between scintillation detector (NaI: 3x3 inches) and Ge(Li) semiconductor. The superior energy resolution of the germanium semiconductor detector is evident from the much narrower peak, allowing separation of gamma-ray energies that are unresolved in the scintillator histogram.

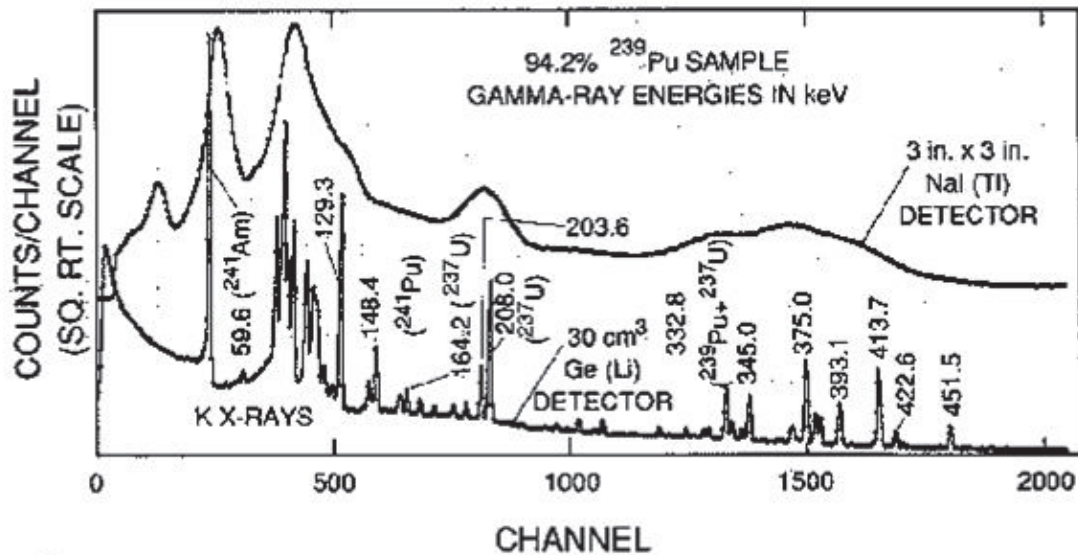


Figure 106: Comparison of energy resolution obtained from  $^{239}\text{Pu}$  sample

(NSSEP, 2017)

The energy resolution of AXINT gamma detection system (BGO: 1 x 1 inch in cylinder form) is measured at 21% for  $^{22}\text{Na}$  (Figure 112). The standard energy resolution using BGO is at around 9.5% for  $^{137}\text{Cs}$  in a scintillation volume of  $10 \times 10 \times 10 \text{ cm}^3$  (V.V. Avdeichikov, 1994). This reference allows us to validate our BGO gamma detection system in a small scintillation volume (2 times less than the reference volume) situation.

Two set of sensors prepared to be installed in parallel and perpendicular direction to host rock bedding have been designed for  $\gamma$  experiments. The main geometry constraint in the design of gamma sensors were the diameters of sensor boreholes for real time monitoring. Thus, a specific design of gamma sensor were illustrated in Figure 107. Four crystals are separated with an equivalent interval of 10.16 cm (the interval distance between 2 canters of cylinder crystal; crystals are in cylinder form (Diameter 2.54cm; length 2.54cm). On one hand, BGO was used to detect  $^{22}\text{Na}$  at high  $\gamma$  energy absorption. On the other hand, YSO was selected to detect low  $\gamma$  energy such as  $^{241}\text{Am}$  (Chapter 1: 1.4.5.2).

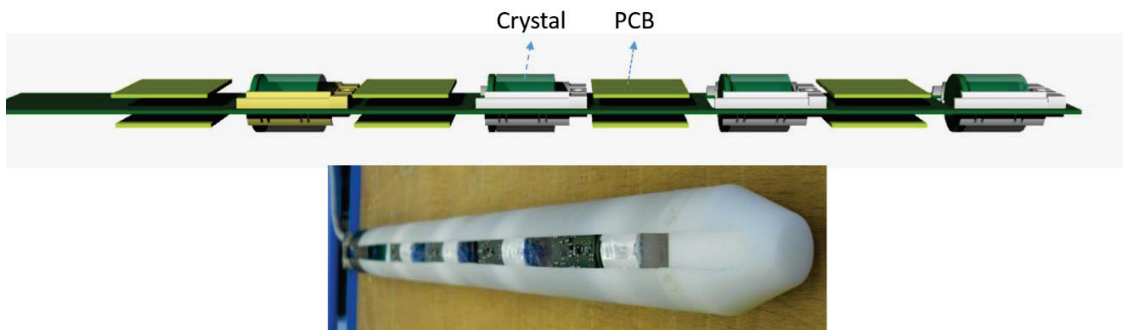


Figure 107: 3D view of gamma sensor design (Top part), view of experimental sensors design (Bottom part)

### 3.3.2.1.2 Detection of $^{241}\text{Am}$ at low energy

The aim of our experiments was to determine the limit path of host rock clay of  $^{241}\text{Am}$ . This limit path depends on the attenuation coefficient ( $\mu$ ) of host rock of  $^{241}\text{Am}$ . The  $\mu$  is defined as the energy loss of particles in per unit path length. The experimental

measurements are performed at CEA L3MR laboratory with their specific supports for  $^{241}\text{Am}$  sources at 1MBq and Callovo-Oxfordian clay rock samples. The  $^{241}\text{Am}$  source is gamma emitter at mainly low energy range ( $<60\text{keV}$ ) with a half-life of 432.6 years (Chapter1: The selection of injected radiotracers and its properties).

The sample (host rock) has been tested in cylinder form (diameter of 8cm), and the thickness varies from 0 cm to 3.22 cm (Figure 108). The top side of host rock is fixed at 15cm above the central of crystal. Thus the bottom side of host rock varies related to the thickness of host rock. The  $^{241}\text{Am}$  is mixed with water in a cylinder vial (Diameter 4cm, length of cylinder around 6 cm). To minimize the incertitude in the position of source  $^{241}\text{Am}$  in the vial solution, the crystal YSO is placed as far as possible (around 15cm) to the source since the detection efficiency vary with the inverse square of the distance (M.C.Lucas, February 1985)

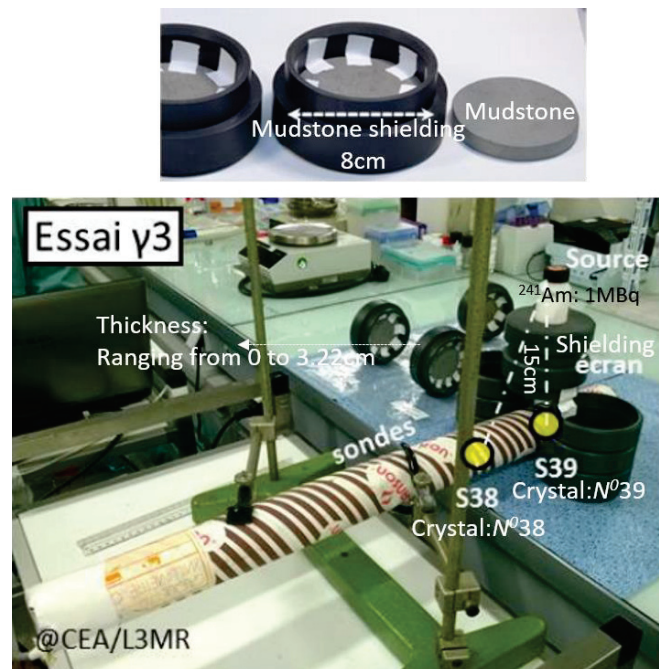


Figure 108: View of different host rock sample thickness and of gamma experimental setup with  $^{241}\text{Am}$  @ 1MBq

In Table 20, 5 series of measurements are listed. The measurements are acquired with a fixed delay of one minute and the LLD of sensors are regulated to be low to consider the photons at low energy ( $^{241}\text{Am}$ ). The net count represents the count subtracted from the background count; the transmission column represents the percent absorption of gamma radiations e.g. absence of host rock conditions, we suppose that the transmission is at 100 percent.

<b>Host rock thickness</b>	<b>Counts per minute total</b>	<b>Counts per minute net</b>	<b>Transmission <math>T=I/I_{\text{MAX}}</math></b>
<b>Without source</b>	4593 (Noise count)		
<b>0cm</b>	97101.9	92509.9	1
<b>1.06cm</b>	55752	51160	0.55
<b>2.16cm</b>	29774	25182	0.27
<b>3.22cm</b>	17075	12483	0.13

Table 20: Study of host rock stopping power property of  $^{241}\text{Am}$

To determine the linear stopping power curve, the variation of  $\log(1/T)$  in relation to different host rock thickness have been plotted as showed in Figure 109.

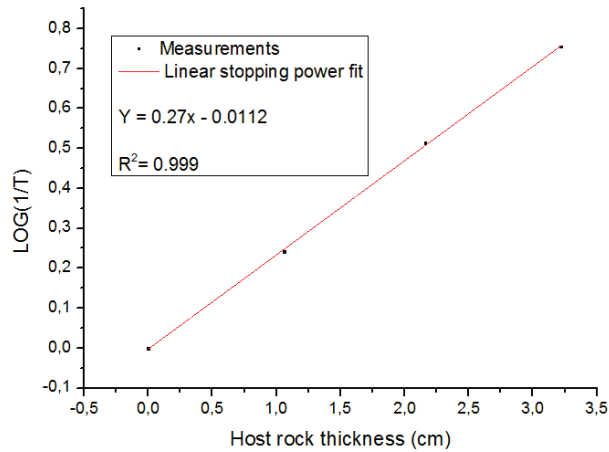


Figure 109: Linear transmission curve of measurements

The slope of fit curve found at 0.27 give a  $\mu$  value equal to  $0.623 \text{ cm}^{-1}$ .

### 3.3.2.1.3 The channels determination for the photo peak at 511keV

#### ***Calibration of Gamma crystals in detection of $^{22}\text{Na}$ at its photo peak***

The experimental setup is made with  $^{22}\text{Na}$  sources placed as showed in Figure 110, a certain distance away from the BGO scintillator (Chapter 2: 2.2.2). The  $^{22}\text{Na}$  source was characterized with its gamma emissions at 511Kev as well as at 1.275 Mev (Chapter 1: 1.4.5.2). As described in previous chapter (Chapter 2: 2.2.5), 2 counting mode are available (SCA and MCA). In our case, MCA mode is selected to use the interval channel (lower channel and upper channel) that should include the energy channel of photo peak at 511KeV. Firstly, 4 energy histograms on one probe with 4 crystals have been plotted as illustrated in Figure 111. The energy emissions of  $^{22}\text{Na}$  are distributed along 4095 channels. All crystals should be adjusted to present photo peak (511KeV) centered at around channel 1500. Finally, Gaussian fitting has to be required to obtain corresponding gaussian parameters such as peak, sigma, and energy resolution value and so on. As one

probe composed of 4 sensors and 4 source holder (Figure 107), four repeated operations stated before are required.

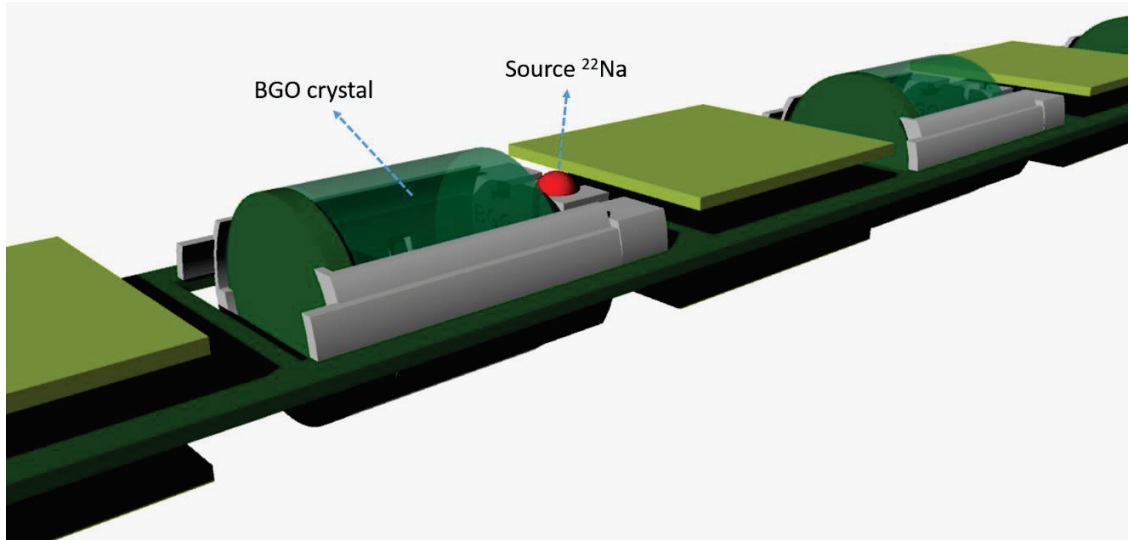


Figure 110: Source position in calibration of gamma crystal

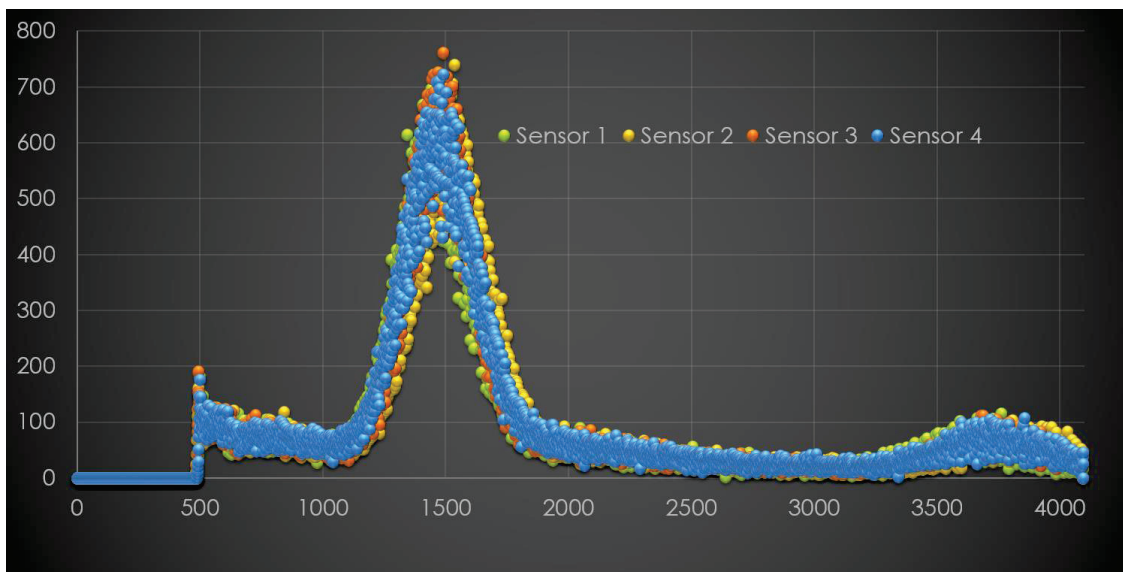


Figure 111 : Energy histogram for 4 gamma crystals

Figure 112 illustrates a Gaussian fitting results of measurements data including peak, sigma, offset, amplitude, energy resolution and 2.5 counts sigma values, in this

figure, the results identified the median point centered at channel 1483 with a sigma ( $\sigma$ ) of 127.3 for example.

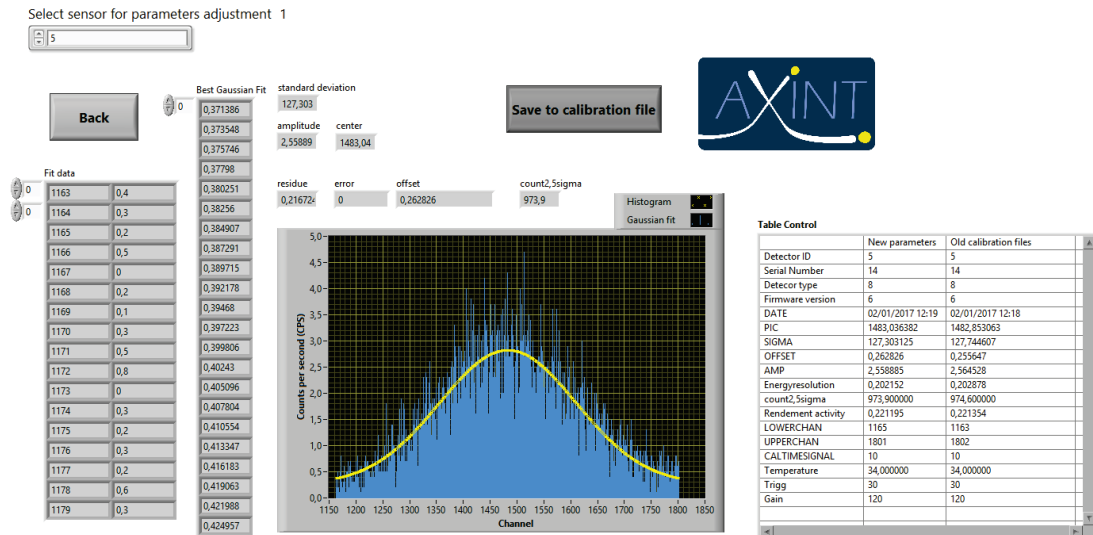


Figure 112 : Energy histogram Gaussian fit for crystal ID51

The following table (Table 21) summarised Gaussian fitting parameters related to one probe with 4 integrated crystals. This table confirmed the uniform response of MCA counts (sum of 2.5 sigma at 511KeV photo peak) that allow us to validate our sensors calibrations in presence of radioactivity  $^{22}\text{Na}$  source.

	ID1	ID2	ID3	ID4
$\sigma$	135.7	127	128	126
Gaussian center	1510	1483	1506	1468
Interval channel (2.5 sigma)	(1170,1849)	(1166,1801)	(1187,1826)	(1153,1783)
Sum +/-2.5 sigma	2092	2121	2200	1989
Percent deviation compare to ID51	0	+1.3%	+5.16%	-4.9%

Table 21 : Calibrations of 4 gamma crystals

The sensors under these configurations are pre-monitored during a certain time and give a uniform response (Figure 113) for the background count level.

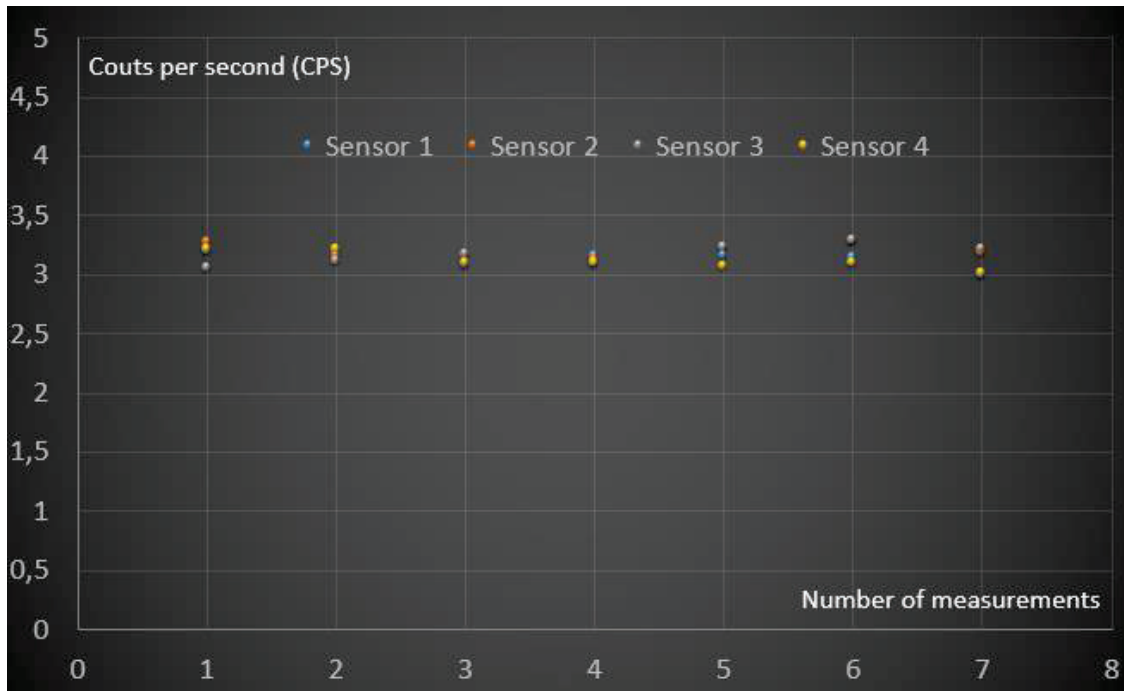


Figure 113: Calibrated sensors'background counts

To be better regulate Gaussian center or photo peak of all crystals at a value approximated to channel 1500, I developed a new powerful AXINT calibration software. It consists of following operation process:

1. Detect sensors and choose sensor and source to be used. (Figure 114)
2. An approximation manual sensor adjustment to keep Gaussian center at around channel 1500. (Figure 115)
3. An automatic refined gain labview program to be executed to fix the Gaussian center at around 1500. (Figure 116)
4. Noise measurements and possible up to 4 crystals measurements at the same time.

5. Subtraction of signals to noise measurements and Gaussian fitting to find corresponding parameters. (Figure 117)

The interface shows the AXINT logo at the top right. Below it, there are two main sections for configuration:

**Sensor Configuration:**

- Select sensor for parameters adjustment: 18
- Detect sensors button
- Files location: C:/sensor files/ID/calibration.txt

ID	Trigg	Gain	Firmware version	Sensor type	Serial number	Temperature
18	30	128	8	8	27	33.250000
25	30	128	8	8	34	36.000000
27	30		8	8	36	33.500000
28	30	128	8	8	37	33.500000

**Source Configuration:**

- Select source for calculation: AXINT 22Na
- Files location: C:/ANDRACALIB/SOURCEXXX.TXT

Isotope	Numéro de la source	Date du certificat de la source	Activité d'étalonnage de la source Bq	Période de la source	Nom de la source
22Na	1	2008.11.10	38600	950	AXINT 22Na
22Na	2	2011.08.01	20100	950	ANDRA2
22Na	7	2011.08.01	78000	950	ANDRA7

At the bottom, there are three buttons: "Go to noise calibration", "Next step", and "Exit".

Figure 114: Interface to detect on line sensors and select the radioactivity source to be calibrated

The interface shows a grid background with various controls and a plot window:

- Select sensor for parameters adjustment: 5
- Photoelectric peak: 1448
- Reset energy histogramme button
- Canal de begin: 1748, Canal de fin: 1148
- Waiting second: 20
- Trigger: 30
- Gain adjust: 120
- Write Trigger and Gain button
- Get energy histogram button
- Refine Gain button
- Go to noise calibration button
- Back button
- Enregistrement trames window showing a plot of Count(CPS) vs Channel. The plot shows a sharp peak at approximately 1596 channels. A cursor is positioned at 1596 on the x-axis and 290.72 on the y-axis.
- Time Used: 22
- Cursor/Cursor Position/Cursor Y: 3284.09
- Cursor 0: 1596, -290.72

Below the plot, there is a text box with instructions in French: "on charge 1 histogramme, et on peut changer les paramètres pour positionner le pic vers le channel 800. Ensuite, le bouton refine gain permet de tester les valeurs de gain de gain -10 à gain +10. Quand on appuie next step, affiche un warning si on a pas fait Refine gain."

Figure 115: Interface to get sensor energy histograms

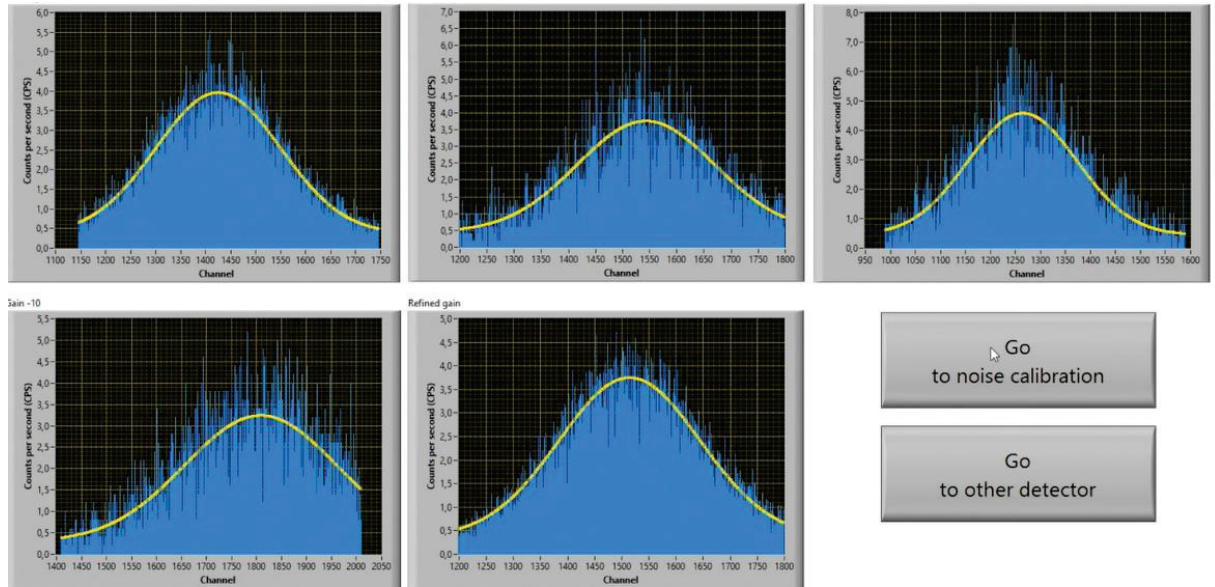


Figure 116: Interface refined gain to adjust Gaussian center at channel 1500

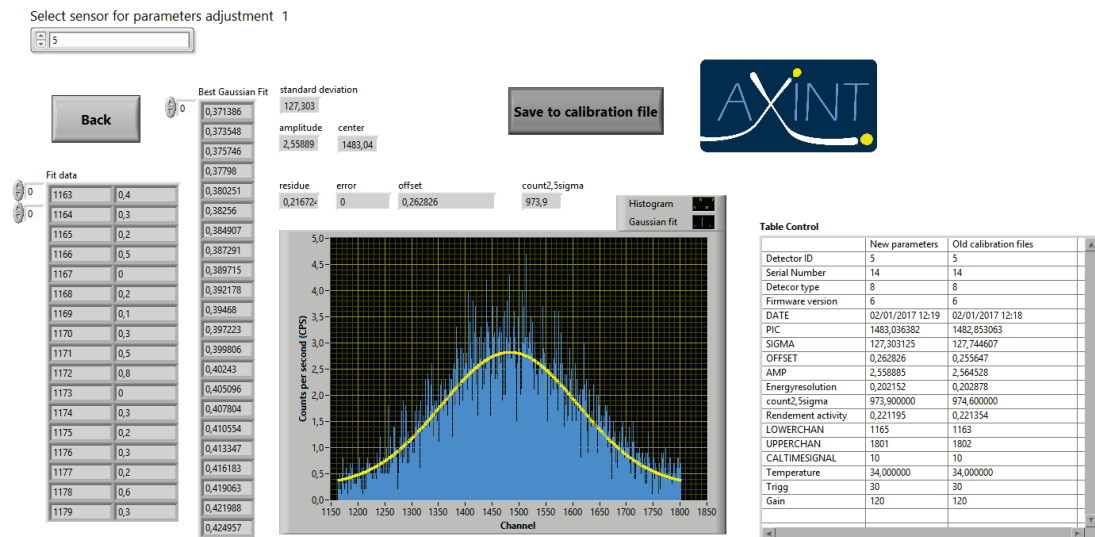


Figure 117: Interface to show the Gaussian fitting parameters and calibration results

After our sensor systems have been calibrated or adjusted, a real time on-line monitoring system has to be used for at least 10 years. Thus, our AXINT acquisition system should be robust and reliable, it is based on National instrument solutions. As showed in Figure 118, it can support 12 probes, the core system is CompactRIO

Controller (cRIO-9064) which is an embedded controller ideal for advanced control and monitoring applications. It features an FPGA and a real-time processor running the NI Linux Real-Time OS, which gives access to the Linux community.

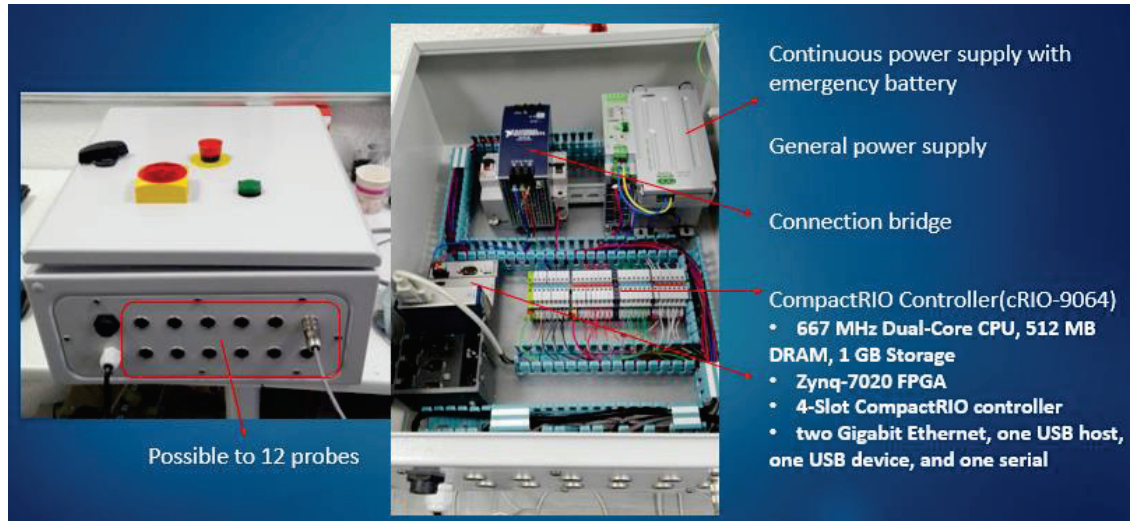


Figure 118: AXINT real-time monitoring system

Recently, AXINT team has installed 4 gamma probes definitively and it is under monitoring (Figure 119). Some more results will be exploited in the future and new articles will be prepared to be submitted.

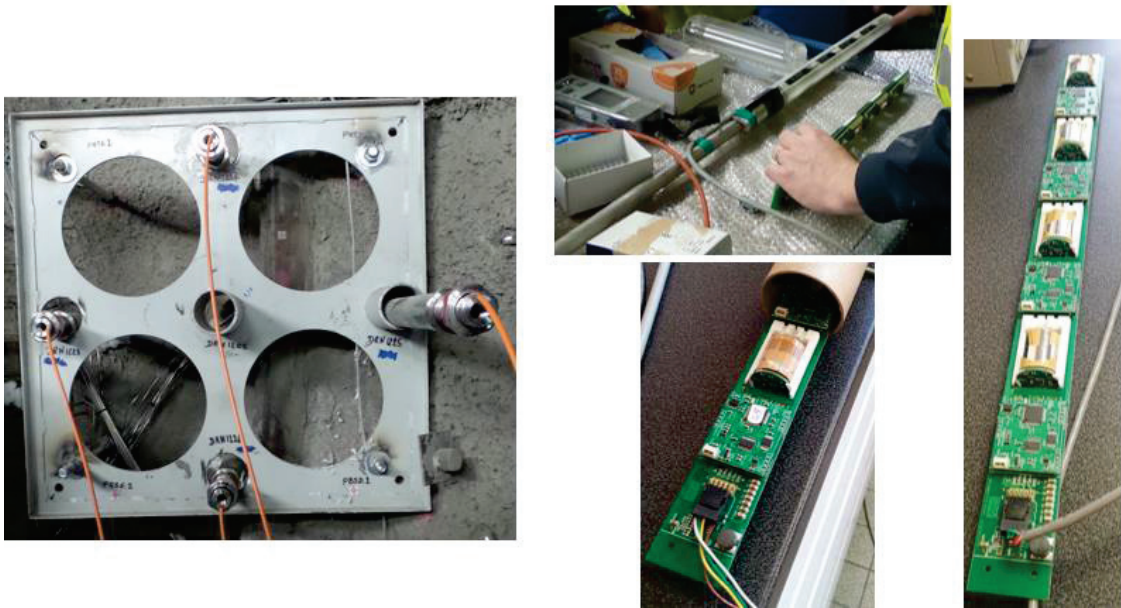


Figure 119: DRN1203: In situ experimental setup

#### 3.3.2.1.4 Verification of the response linearity

##### **Photo peak counts validations:**

To verify the selection of manual interval channels, two different activity sources have been measured (2.26 and 24.31KBq). It is almost for all channels that the value increase significantly related to source activity (Figure 120). In Table 22, the calculations using the count window (Determined in Table 21) revealed a satisfied linear fit at  $R^2=0.999$  (Figure 121) compared to two source activity.

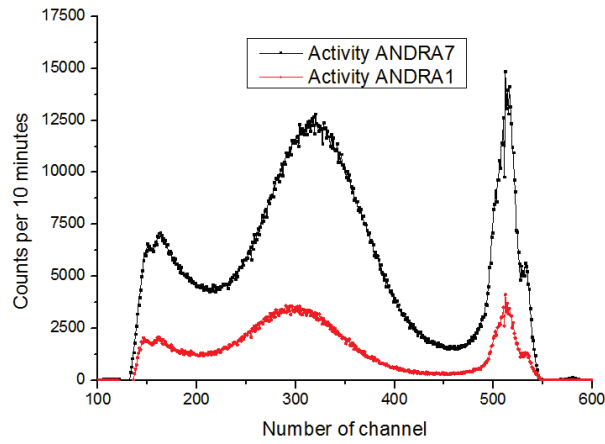


Figure 120 : Energy histogram for crystal ID51 with 2 different activities

	Activity(KBq)	Noise per 10 minutes	Net counts per 10 minutes
<b>ANDRA1</b>	6.26	3082±55	265429±574
<b>ANDRA7</b>	24.31	3082±55	965156±1035

Table 22 : Counts response to 2 different activities

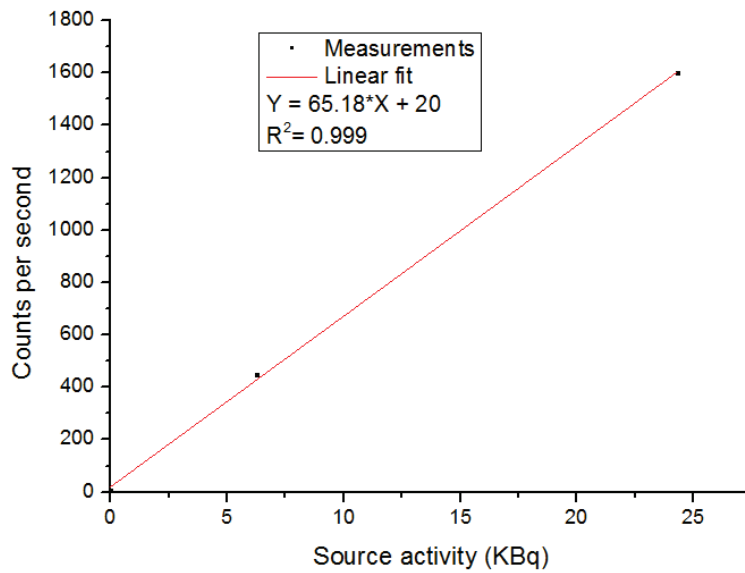


Figure 121 : Linear fit of different source activities to validate the calibration of  $^{22}\text{Na}$

Although all crystals were set to give the same counting level to characterize photo peak of  $^{22}\text{Na}$  in presence of source, it should be noted that this sensor calibration does not give the same background level, it varies from 4 to 8 CPS. As for difficult access of sensor installed at URL, further more investigations will be conducted on this point. Meanwhile, it gave rise to a good linearity response (Figure 121), perhaps we can conclude that this calibration are only available for  $^{22}\text{Na}$  at its characteristic emissions at 511KeV.

### 3.3.2.2 Gamma simulation studies:

#### 3.3.2.2.1 Calculation via simulation of the stopping power of Callovo-Oxfordian clay rocks at 60KeV

The attenuation coefficient of host rock determined by direct previous measurements are complexes and time consuming. We have tested this parameter via MCNP simulations (Figure 122).

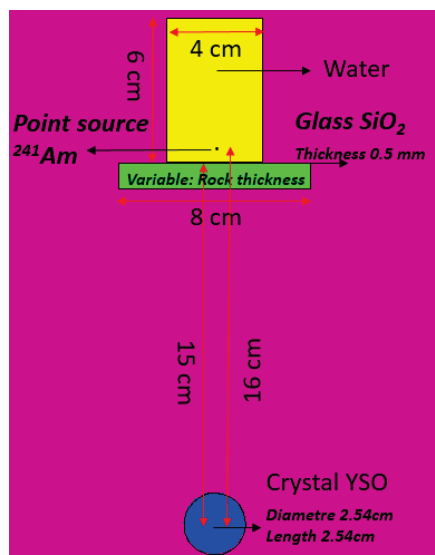


Figure 122: Simulation geometry view at px=0 in study of the stopping power of host rock at low energy for <sup>241</sup>Am

In MCNP simulations, some elements are necessary, and in particular the radiation interaction matter (Host rock). The composition of Callovo-Oxfordian, fundamental to study the trajectories of radiations, were studied by E.Gaucher (Gaucher, 2004). Shifting from chemical to MCNP model, the material is decomposed as a set of elements in forms of ZZZAAA where ZZZ is the atomic number and AAA is the atomic mass number and illustrates the simple transformation from chemical composition to element composition is necessary and the conversion results are illustrated in Table 23.

	<b>Mass fraction(E.Gaucher)</b>	<b>Element</b>	<b>Atom fraction</b>
<b>Al<sub>2</sub>O<sub>3</sub></b>	12.8	Al	0.04
<b>Fe<sub>2</sub>O<sub>3</sub></b>	4.4	Fe	0.009
<b>CaO</b>	12.1	Ca	0.034
<b>MgO</b>	2.6	Mg	0.01
<b>MnO</b>	0.03	Mn	6.72E-5
<b>K<sub>2</sub>O</b>	3.1	K	0.01
<b>Na<sub>2</sub>O</b>	0	Na	0
<b>TiO<sub>2</sub></b>	0.7	Ti	0.0014
<b>P<sub>2</sub>O<sub>5</sub></b>	15.6	P	0.00018
<b>SiO<sub>2</sub></b>	48.7	Si	0.129
<b>S</b>	0.83	S	0.0041
<b>C</b>	0.8	C	0.010
<b>H<sub>2</sub>O</b>	13.86	H	0.24
		O	0.5068

Table 23: List of MCNP host rock elements

Second difficulty found on simulation is related to the accuracy of geometry description compared to the real experimental conditions, typically for the source position in the solution and the thickness of glass in the solution vial which are invisible and unmeasurable. The uncertainty of vial glass is considered not negligible because of the absorption efficiency for low gamma radiations for low gamma energy emission. Although these uncertainties exist, the gamma attenuation coefficient of host rock is supposed with its inherent property. A series of simulations have been taken into account the effects of small geometry variation in order to determine the stopping power property of host rock.

We took the sources placed 1 cm above the top of the host rock sample as reference and additional spaces of 1 and 2 cm (2 and 3 cm above the top of the host rock). The simulation results are shown in Table 24. The simulations are made with 1.06, 2.16 and 3.22 cm rock thickness as in real measurements. In the first column, we reported uncertainty on the source position. The intensity detection efficiency represents the probability to detect for one gamma emission; it is obvious that the closer the radiation source to the crystal, the higher the detection efficiency. The term transmission gives a normalisation of detection efficiency related to the one without host rock present.

<b>Source position</b>	<b>I detected after 0cm rock</b>	<b>I detected after 1.06 cm rock</b>	<b>I detected after 2.16 cm rock</b>	<b>I detected after 3.22 cm rock</b>
<b>Ref (I) (1 cm)</b>	11.5E-4	6.30E-4	3.13E-4	1.56E-4
<b>2 cm</b>	9E-4	4.73E-4	2.37E-4	1.16E-4
<b>3 cm</b>	5.83E-4	3.02E-4	1.51E-4	0.73E-4
<b>Transmission <math>T=I/I_{0\text{ cm}}</math></b>				
<b>1 cm</b>	1	0.547	0.272	0.136
<b>2 cm</b>	1	0.53	0.263	0.13

<b>3 cm</b>	1	0.52	0.259	0.12
-------------	---	------	-------	------

Table 24 : Influence of source position incertitude to the study of rocks attenuation coefficient

The Figure 123 summarises the changes in linear response of host rock attenuation coefficient as function of position source. Calculations have been done (Table 25) using fit curve in Figure 109.

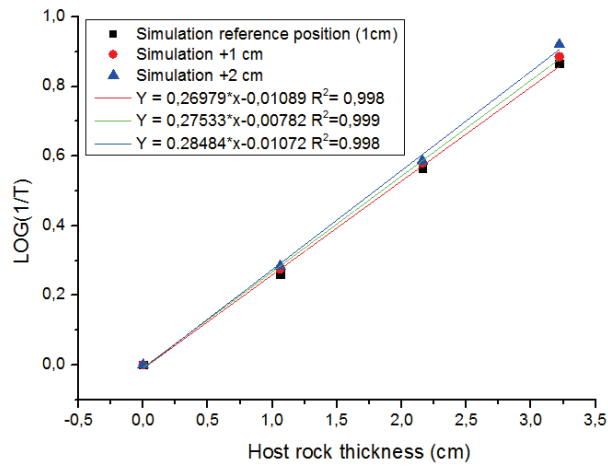


Figure 123 : Linear fit of simulation MCNP results with small variations of source position

An incertitude tolerance of 2 cm gives a 0.0347 variation of gamma attenuation coefficient of Callovo-Oxfordian rocks ranging from 0.6210 to 0.6557 (Table 25).

<b>Source position</b>	<b><math>\mu(\text{cm}^{-1})</math></b>
<b>Ref ( 1cm )</b>	0.6210
<b>2cm</b>	0.6339
<b>3cm</b>	0.6557

Table 25 : Influence of incertitude of source position in determination of host rock attenuation coefficient property

In contrast, varying the via glass (SiO<sub>2</sub>) thickness but keeping the source fixed at 1cm above the top of host rock (Figure 124). We obtained less important variation in the determination of host rock attenuation coefficient property as showed in Table 26.

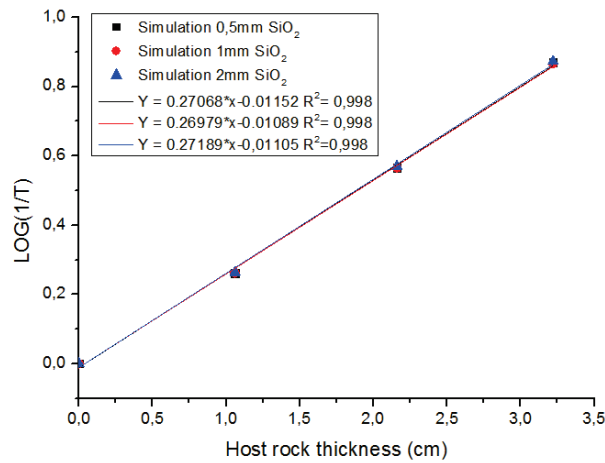


Figure 124 : Linear fit of simulation MCNP results with small variations of SiO<sub>2</sub> thickness

<b>SiO<sub>2</sub> thickness (mm)</b>	<b>μ(cm<sup>-1</sup>)</b>
<b>Ref ( 0.5mm )</b>	0.6233
<b>1mm</b>	0.6214
<b>2mm</b>	0.6260

Table 26: The influence of SiO<sub>2</sub> thickness for determination of host rock attenuation coefficient property

Then we have estimated that the simulations with radioactive source position 1cm above the top of the host rock and 0.5mm thickness of SiO<sub>2</sub> are approach to our real situation. Finally, the comparison between simulations and real measurements presented a neglected difference of 0.0020 (Table 27).

	$\mu(\text{cm}^{-1})$
<b>Simulation</b>	0.6210
<b>Measurements</b>	0.6230

Table 27: Comparison of host rock attenuation coefficient property via simulation and measurements

### 3.3.2.2 Estimation and simulation of the stopping power of Callovo-Oxfordian clay rocks at 511Kev

Another installation was designed to detect <sup>22</sup>Na. Two boreholes are reserved. One borehole was used to place source activity <sup>22</sup>Na (Figure 125: 26.8cm, 6.74cm) at 24.31 KBq, another borehole was considered to detect the source using a gamma sensor including 4 crystals (Figure 125: separated by 10.16cm one by one)

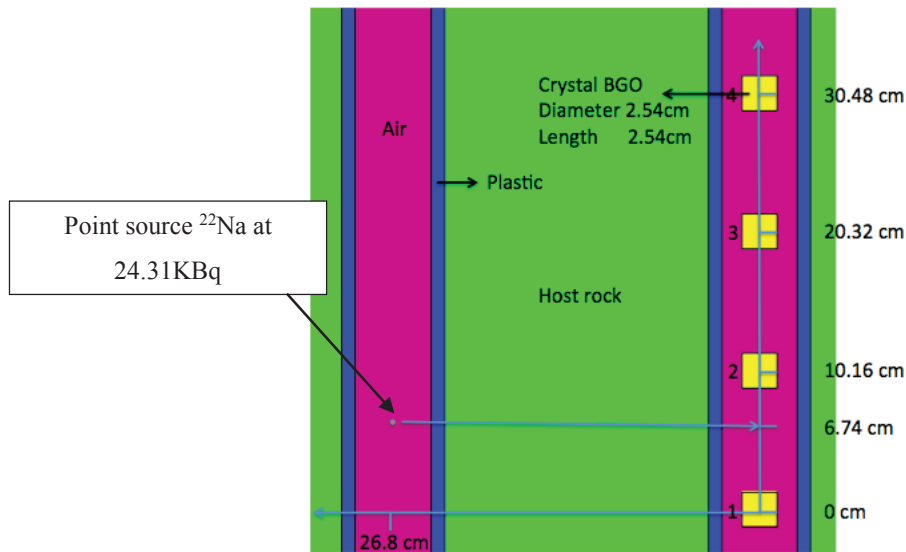


Figure 125: Detection of  $^{22}\text{Na}$  in host rock milieu

The measurements accumulated during 150 minutes were considered within a confidence level at 95% ( $\pm 2$  sigma). The limit of detection has been calculated using 20 sigma method. The MCNP simulation gave directly the detection efficiency of gamma counts. The simulation CPS was calculated by multiply source activity to detection efficiency (Table 28).

cm	Noise (cps)	Net Measurement cps	Limit of detection	MCNP simulation efficiency (%)	Simulation cps
0	5.45 $\pm$ 0.05	0.92 $\pm$ 0.07	0.5	0.00431	1.05
10.16	6.63 $\pm$ 0.054	1.036 $\pm$ 0.08	0.54	0.00477	1.16
20.32	8.08 $\pm$ 0.06	0.383 $\pm$ 0.09	0.60	0.00315	0.765
30.48	4.37 $\pm$ 0.044	0.303 $\pm$ 0.06	0.44	0.00125	0.305

Table 28: Simulation and measurement results in study of  $^{22}\text{Na}$

In Figure 126, the position of first crystal (Crystal 1) is a reference position (Figure 126: 0 cm); all the other ones are related to the reference. The activity source were close to the first and the second crystal that gave a higher count rate compared to crystal 3 and 4. Nevertheless the count rates of last two crystals (3 and 4) are under the limit of detection (0.6 CPS). This confirms that crystal 3 and 4 are no reliable both in measurements and simulation cases.

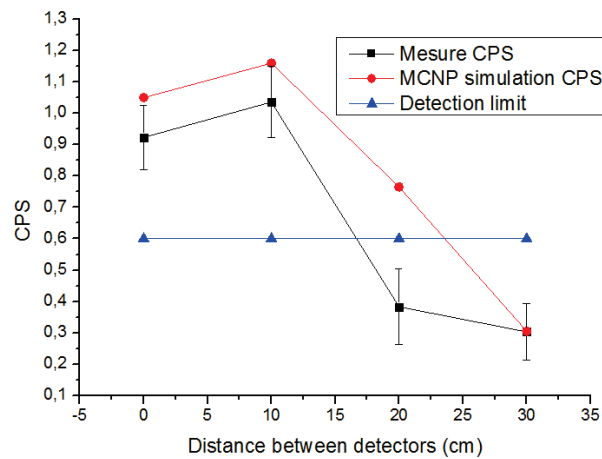


Figure 126: Detection of  $^{22}\text{Na}$  via measurements and simulations and with its detection limits after 150 minutes accumulation

### 3.3.3 Conclusion

In this chapter, a mixed simulation and experimental experience have been presented. This would possible give a confusion or for the readers. The volume of liquid chamber was optimised by MCNP simulations to 1.4mL ( $\text{Ø} \times L = 30 \times 2 \text{mm}^2$ ). This small

sensible detection volume limited the use of FOSs. Two designs of beta sensors have been developed and compared. The beta with the minimum crystal thickness presented a better SNR and a low noise count level (1.25CPM). The sensor SNR value was given by the MCNP simulations as well (Figure 105). This beta sensor was found to be adapted for in situ experimentation using  $^{36}\text{Cl}$  injection for long time diffusion experiments. The limits of detection of the beta sensor had been quantified for 1h and 24h using Currie equation at 18 and 14.18Bq/mL respectively.

For gamma sensors, crystals have been regulated with  $^{241}\text{Am}$  and  $^{22}\text{Na}$  radiotracers. The first set of 4 gamma crystals for  $^{241}\text{Am}$  was set for very low energy (superior to 30KeV) of gamma emission in SCA counting mode. The stopping power of host rock of  $^{241}\text{Am}$  was determined at  $0.623\text{cm}^{-1}$ . The same results have been proved via MCNP simulations. Another sensor of 4 gamma crystals are used to characterize the photo peak detection of  $^{22}\text{Na}$  at 511KeV. With manual regulation of count window, all crystals gave the same range of count rate with less than one percent of deviation considering ID51 as reference. A good linear response compared different activities that confirmed our calibration process. Meanwhile, the background was not the same regarding 4 crystals. This made us consider that our calibrations were only validated to detect  $^{22}\text{Na}$  at 511KeV.

In the future work, we will focus on optimizations of radiation instruments such as electronic system design and software; our new protocols were fabricated and will be tested, measured in situ and more articles will be submitted in the future. More simulation scenarios are preferred to evaluate the count rate detection in response of the tracers' diffusion in interaction with Callovian-Oxfordian host rock milieu. And a robust algorithm for the determination of the radiotracers diffusion form will be developed. At long term, it can be applied to other in situ experiments, such as effluent management, radioactive waste leaching...

## General Conclusion

My work has been focus on radiation fields. It has enormous potential of benefiting. For example, use of radiation tracer allowing the determination of the position or the distribution of a process such as diffusion process in our case, and medical diagnostics in the form of CT and nuclear scans (PET/CT, SPECT/CT). To achieve the objective of in situ diffusion tests with a large scale of distance (hundreds of mm) and long time (larger than 10 years) monitoring sensors system, my work required a large spectrum of scientific: physics, electronic, information, embedded system and radiation measurements. I simulated the physic compartment of radiation particles through MCNP6 to predict sensors response; first sensor protocol had been developed (electronic, embedded system, software) and tested (radiation measurements), and an article was prepared to be submitted. A new protocol was under development with optimizations of electronic system design and software of radiation sensors, and will be tested in the future.

This project as entitled “Development of high sensitivity gamma and beta sensors for in situ diffusion tests in the mudstone in France” composed of only one part of work. I developed different radio sensors used in quality control of radio pharmaceutical as well. I integrated a new powerful MCU and external 12 bit ADC instead of previous 10 bit ADC in MCU module, confirmed effects that 2 SiPM in series can increase the sensitive area, thus achieve better time resolution. Now these optimizations are regarded as our reference protocol of radio sensors and are considered the base of new protocol using in situ diffusion tests.

Lastly, I developed the MCU programing of the Time-Resolved Fluorescence (TRF) spectroscopy instrument. This instrument allows us to collect the photon emission signal that used to dose the inhibitors of oil. The first protocol have been developed and commanded by TOTAL Company.

## Bibliography

- A. Lavagno, G. S. (2012). Study of linearity and internal background for LaBr.
- Abmed, S. N. (2007). Physics and Engineering of Radiation Detection. Elsevier.
- Andra-ASN-CEA-IRSN. (2016). *Radioactive waste management programmes in OCED/NEA Member countries*. France.
- AXINT. (2007). *AXINT technical*. Récupéré sur <http://www.axint.org/?Qu-est-ce-qu-un-SiPM&lang=en>
- Barral, J. (2004). *Study of Silicon Photomultipliers*. Paris.
- Beddar, S. K. (2001). A miniature scintillatorfiber opticPMT detector system for the dosimetry of small fields in stereotactic radiosurgery. *IEEE Transactions on Nuclear Science*, 48(3), 924 - 928 .
- Byun, S. H. (chapter 4). Med Phys 4R06/6R03 Radioisotopes and Radiation Methodology. Dans S. H. Byun, *chapter 4*. Ontario.
- C.Fréchou, J.-P. (2004). Measurement of <sup>36</sup>Cl in nuclear waste and effluents. *Radioanalytical and Nuclear chemistry*, 263(2), 333-339.
- Chelsea A. D'Angelo, S. S. (2012). Modeling Radiation Transport Using MCNP6 and Abaqus/CAE .
- Cook, N. D. (2010). *Models of the Atomic*. Japan: Springer.
- Corrigan, S. (2008). *Introduction to the Controller Area Network (CAN)*. Texas instruments.
- Crank, J. (1975). *The Mathematics of Diffusion, Second Edition*. London: Clarendon.
- Delay, J. A. (2006). Making of the underground scientific experimental programme. *Physics and chemistry of the earth*, 32(2-18).

- Dewonck et al. (2009). Long term in situ tracer diffusion tests in the Callovo-Oxfordian clay: results and modeling. *12th International Conference Migration*. Washington, USA.
- Dewonck, S, D. M. (2007). In situ diffusion tests performed in the callovo-oxfordian mudstone in the Bure URL., (pp. 465-466). Lille.
- Dinu, N. (2013). *Instrumentation on Silicon Detectors: from properties characterization to applications*. Paris.
- E. Gaucher a, C. R. (2004). ANDRA underground research laboratory: interpretation of the mineralogical and geochemical data acquired in the Callovian–Oxfordian formation by investigative drilling. *Physics and Chemistry of the Earth* , 29, 55-77.
- Éric C. Gaucher, P. B. (2006). Modelling the porewater chemistry of the Callovian–Oxfordian formation at a regional scale. *Geochemistry*, 338, 917-930.
- F. Goutelard, N. D. (2007). Modélisation du transport dans les roches argileuses - Apport de la description à l'échelle nanométrique. Avignon.
- F.C.L. Crespi, F. C. (s.d.). Alpha-Gamma discrimination by Pulse Shape in LaBr<sub>3</sub>:Ce and LaCl<sub>3</sub>:Ce.
- F.C.L. Crespi, F. N. (2009). Alpha–gamma discrimination by pulse shape in LaBr<sub>3</sub>:Ce and LaCl<sub>3</sub>:Ce. *Nuclear Instruments and Methods in Physics Research A*, 602, 520-524.
- F.KNOLL. (s.d.). *Radiation Detection and Measurement Fourth Version*.
- Gaucher, E. e. (2004). Interpretation of the mineralogical and geochemical data acquired in the Callovo-Oxfordian formation by investigative drilling. *Physics and Chemistry of the Earth A/B/C29*, 55-77.
- Gerard, P. I. (2016). *Détection de traceurs particuliers au sein d'argilites*. Lyon.

- Gimmi, T. L. (2014). Anisotropic diffusion at the field scale in a 4-year multi-tracer diffusion and retention experiment – I: Insights from the experimental data. *Geochimica et Cosmochimica Acta*, pp. 125(0), 373-393.
- H. Tsige-Tamirat, , U. (2008). Use of McCad for the conversion of ITER CAD data to MCNP geometry. *Fusion Engineering and Design*, 83 (10-12), 1771-1773.
- H.Preud'homme, C.-P. (2012). Water tracers in oilfield applications: Guidelines.
- Hautefeuille, B. (2014). *Rapport dimensionnement ANDRA*.
- IAEA. (2001). Radiotracer technology as applied to industry.
- Instruments, N. (2013). *LabVIEW: Getting started with Labview*.
- Instruments, T. (2008). *Introduction to the Controller Area Network (CAN)*.
- J. Delay, P. H. (2010). Meuse/Haute-Marne centre: next steps towards a deep disposal facility. *Journal of Rock Mechanics and Geotechnical Engineering*, 2(1),52-70.
- J.M.Matray, E. C. (s.d.). ANDRA underground research laboratory : interpretation of the mineralogical and geochemical data acquired in the Callovian-Oxfordian formation by investigative drilling . *Physics and chemistry of earth*.
- Jacques Pocachard, P. B. (2005). In situ measurement of diffusivity. *NUKLEONIKA*, 50(1),3–7.
- Jain, R. (2009). BIOPHYSICS. VK(India) Entreprise.
- John C. WAGNER, D. E. (2011). Review of Hybrid (Deterministic/MonteCarlo) Radiation Transport Methods, Codes, and Applications at. *Progress in NUCLEAR SCIENCE and TECHNOLOGY*, 2, 808-814.
- Luc R. Van Loon, M. A. (2007). Anion exclusion effects in compacted bentonites: Towards a better understanding of anion diffusion. *Applied Geochemistry*, 2536-2552.

- M. García-Gutiérrez, U. A. (2009). Diffusion Experiments with Opalinus and Callovo-Oxfordian Clays: Laboratory, Large-Scale Experiments and Microscale Analysis by RBS. Ciemat.
- M.C.Lucas, H. (February 1985). IEEE Transactions on Nuclear Science . *A semiempirical method for calculating detector efficiency as a function of distance*, NS-32.
- Michael H. Bradbury, B. B. (2005). Modelling the sorption of Mn(II), Co(II), Ni(II), Zn(II), Cd(II), Eu(III), Am(III), Sn(IV),Th(IV), Np(V) and U(VI) on montmorillonite: Linear free energy relationships and estimates of surface binding constants for some selected heavy metals and actinides. *Geochimica et Cosmochimica Acta*, 69(4), 875-892.
- Microchip. (2012). *dsPIC33EPXXX(GP/MC/MU)806/810/814*.
- microchip. (web). *MPLAB® X Integrated Development Environment (IDE)*. Récupéré sur <http://www.microchip.com/mplab/mplab-x-ide>
- Miramonti, L. (2002). A plastic scintillator detector for beta particles. *Radiation measurements*, 35(4), 347-354.
- Mitch Heynick, I. S. ( LAPA Digital Technology Seminar ). *3D CAD, CAM and Rapid Prototyping*.
- Montarnal, P. M. (2007). Presentation and use of a reactive transport code in porous media. *Physics and Chemistry of the Earth*, 32, 507-517.
- Moreland, K. (Version 3.12). *The ParaView Tutorial Version 3.12*.
- N.L.Hassing. (1990). The effect of count time on reliability detectable activity when assessing contamination monitor performance. *Contamination monitor performance*.

- News, W. N. (2012, 8 6). *France details nuclear waste inventory*. Récupéré sur World nuclear news: [http://www.world-nuclear-news.org/WR-France\\_details\\_nuclear\\_waste\\_inventory-0608124.html](http://www.world-nuclear-news.org/WR-France_details_nuclear_waste_inventory-0608124.html)
- Norris, S. (2014). *Clays in Natural and Engineered Barriers for Radioactive Waste Confinement: an introduction*. London: The Geological Society of London .
- Norris, S. (2014). Clays in Natural and Engineered Barriers for Radioactive Waste Confinement: an introduction. *Geological Society*, pp. 400(1) 1-5.
- NSSEP. (2017). *Nuclear security& safeguards Education Portal*. Récupéré sur <http://nsspi.tamu.edu/nssep/courses/basic-radiation-detection/semiconductor-detectors/detector-comparisons/detector-comparisons-page-three>
- Nucléide-Lara. (s.d.). *Library for gamma and alpha emissions*. Récupéré sur <http://www.nucleide.org/Laraweb/>.
- P. Jacquier, D. H. (2013). The influence of mineral variability of Callovo-Oxfordian clay rocks on radionuclide transfer properties. *Applied Clay Science*, 83-84, 129-126.
- P. N. Luke, M. A. (s.d.). *Recent developments in semiconductor gamma-ray detectors*. Berkeley: Lawrence Berkeley National Laboratory.
- P.De Cannière, H. P. (1996). *Laboratory and in situ migration experiments in the Boom clay*. European Commission.
- Palut, J. M. (2003). Characterisation of HTO diffusion properties by an in situ tracer experiment in Opalinus clay at Mont Terri. *Journal of Contaminant Hydrology*,, pp. 61(1-4) 203-218.
- Paolo W, C. M. (2014). Development of High Precision Timing Counter: Based on Plastic Scintillator with SiPM Readout. *IEEE TRANSACTIONS ON NUCLEAR SCIENCE*.
- R.Taylor, J. (Second Edition). *An introduction to error analysis*.

- Radioactifs, A. n. (2006). *Radioactive waste and recoverable material in France (Summary of the National Inventory)*. Paris.
- Robert, G. (2012). La découverte de la matière radioactive par Marie Curie.
- Runde, W. (2000). *The Chemical Interactions of Actinides in the Environment*. Los Alamos Science.
- S. Dewonck, M. D. (2007). In situ diffusion tests performed in the Callovo-Oxfordian mudstone in the Bure URL: Experimental Data and numerical interpretation., (pp. 465-466). Lille.
- Santin, G. (Chapter II). *Radiation Interaction Physics and Simulation*.
- Shultis, J. (2004-2011). *AN MCNP PRIMER*. Manhattan.
- Si, H. (2013). *TetGen: A Quality Tetrahedral Mesh Generator and 3D Delaunay Triangulator*.
- SITE, A. (2009). *Texts describing Andra's missions*. Récupéré sur ANDRA: <https://www.Andra.fr/international/pages/en/menu21/Andra/regulatory-texts/texts-describing-Andra-s-missions-1586.html>
- Sposito, G. (2008). *The chemistry of soils*. Oxford university press.
- Staff., N. D. (2004). *Principles and Applications of Liquid Scintillation Counting*. National diagnostics.
- Team, X.-5. M. (2003). MCNP — A General Monte Carlo N-Particle Transport Code, Version 5.
- Tor Bjørnstad, o. T. (2015). *Scientific Forum 2015:Tracer Technology and the Search for Oil*.
- V.V. Avdeichikov, L. B. (1994). Light output and energy resolution of CsI, YAG, GSO, BGO and LSO. *Nuclear Instruments and Methods in Physics Research A*, 216-224.

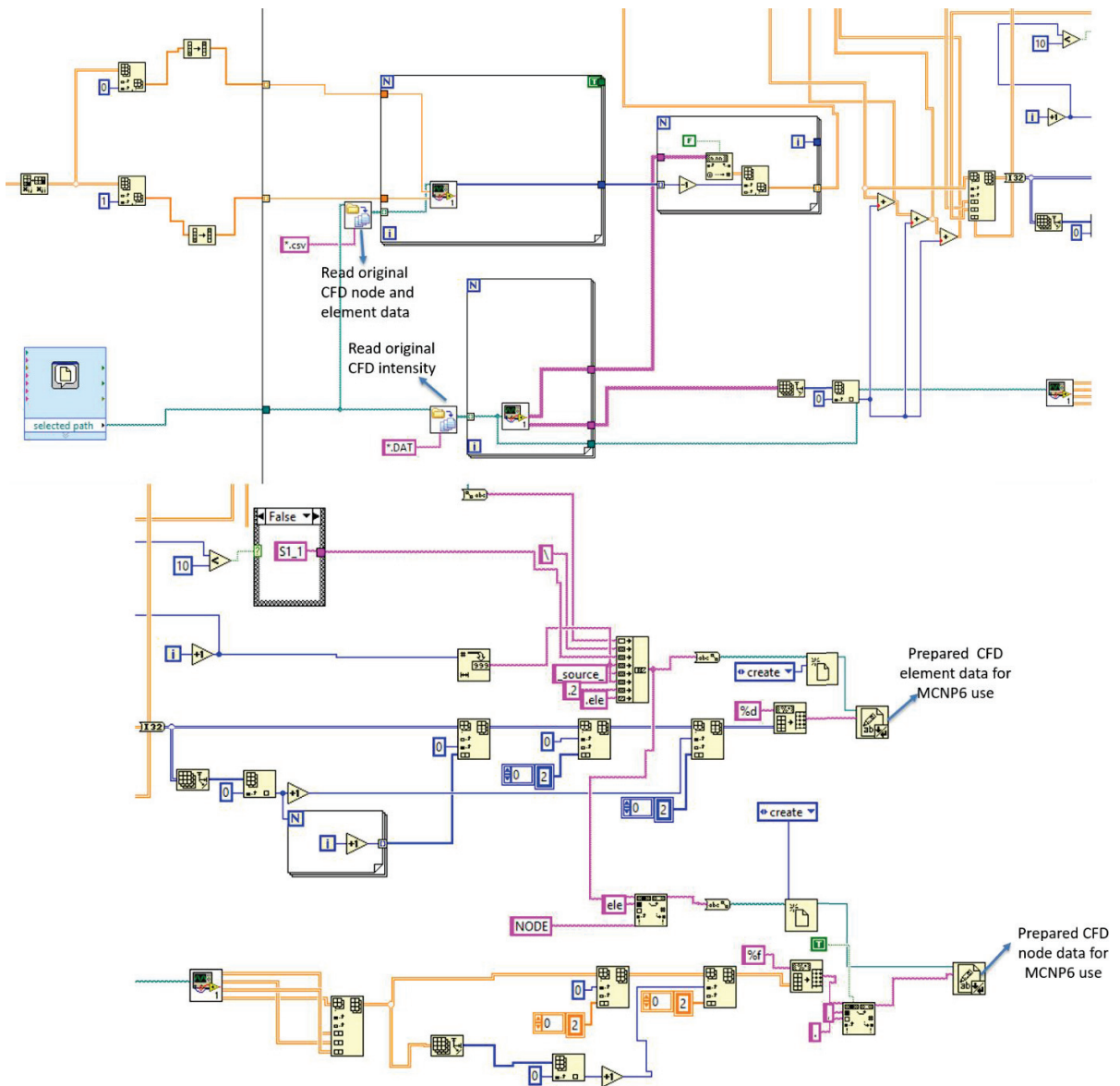
- varian medical systems. (2014). *The Attila Software Suite*. Las Vegas.
- Vinsot, A. (2015). *Specification de l'experimentation DRN (Diffusion de RadioNuclides)*. Document technique interne ANDRA.
- WANG Guozhong, J. X. (2011). Progress and Applications of MCAM: Monte Carlo Automatic Modeling Program for Particle Transport Simulation. *Progress in NUCLEAR SCIENCE and TECHNOLOGY*, 2(821-825).
- Wei, Q. (2014). Intrinsic Radiation in Lutetium Based PET Detector: Advantages and Disadvantages. *Chinese Physics C*.
- Wersin, P. S. (2008). Diffusion of HTO, Br<sup>-</sup>, I<sup>-</sup>, Cs<sup>+</sup>, <sup>85</sup>Sr<sup>2+</sup> and <sup>60</sup>Co<sup>2+</sup> in a clay formation: Results and modelling from an in situ experiment in Opalinus Clay. *Applied Geochemistry*. pp. 23(4), 678-691.
- Wersin., P. (2004). Long term diffusion experiment at Mont Terri: first results from field and laboratory data. *Applied clay science*.
- XCOM, N. (s.d.). *Photon cross sections database*. Récupéré sur <http://physics.nist.gov/PhysRefData/Xcom/html/xcom1.html>
- Yi, S. S. (2012). Identifiability of diffusion and retention parameters of anionic tracers from the diffusion and retention (DR) experiment. *Journal of Hydrology*,. pp. 446–447(0), 70-76.

# ANNEX

## Script plugin developed for creation of STL files

```
1 Option Explicit
2 'Script written by <insert name>
3 'Script copyrighted by <insert company name>
4 'Script version jeudi 13 février 2014 16:34:44
5
6 Call ExportLayerObjectsSTL()
7 Sub ExportLayerObjectsSTL
8
9     ' Declare local variables
10    Dim strPath, strFile
11    Dim arrLayers, strLayer
12    Dim arrSelected
13
14    ' Get the path to and name of the current document.
15    ' Surround with double-quotes in case path includes spaces.
16    strPath = Chr(34) & Rhino.DocumentPath & Rhino.DocumentName & Chr(34)
17
18    ' Get names of all layers
19    arrLayers = Rhino.LayerNames
20
21    ' Disable redrawing
22    Rhino.EnableRedraw False
23
24    ' Process each layer
25    For Each strLayer In arrLayers
26
27        ' Unselect all
28        Rhino.Command "_-SelNone", 0
29
30        ' Select all objects on layer. Surround layer name
31        ' with double-quotes in case it includes spaces.
32        Rhino.Command "_-SelLayer " & Chr(34) & strLayer & Chr(34), 0
33
34        ' Make sure some objects were selected
35        arrSelected = Rhino.SelectedObjects
36        If IsArray(arrSelected) Then
37
38            ' Generate a modified path string
39            ' that includes the layer name
40            strFile = strPath
41            strFile = Replace(strFile, ".3dm", "_" & strLayer & ".stl")
42
43            ' Export the selected objects
44            Rhino.Command "_-Export " & strFile, 0
45
46        End If
47    Next
48
49    ' Unselect all
50    Rhino.Command "_-SelNone", 0
51
52    ' Enable redrawing
53    Rhino.EnableRedraw True
54
55 End Sub
```

## A general Labview source code view of CFD data to MCNP6 code



## Example of MCNP6 code and INP files

```

1 ANDRA diffusion test
2 101 19 -2.53 0 u=1 imp:n=1
3 201 2 -1.293e-3 0 u=1 imp:n=1
4 202 2 -1.293e-3 0 u=1 imp:n=1
5 203 2 -1.293e-3 0 u=1 imp:n=1
6 204 2 -1.293e-3 0 u=1 imp:n=1
7 205 2 -1.293e-3 0 u=1 imp:n=1
8 301 6 -5.2 0 u=1 imp:n=1
9 401 7 -1.38 0 u=1 imp:n=1
10 402 7 -1.38 0 u=1 imp:n=1
11 501 9 -7.3 0 u=1 imp:n=1
12 502 9 -7.3 0 u=1 imp:n=1
13 503 9 -7.3 0 u=1 imp:n=1
14 504 9 -7.3 0 u=1 imp:n=1
15 505 9 -7.3 0 u=1 imp:n=1
16 506 9 -7.3 0 u=1 imp:n=1
17 507 9 -7.3 0 u=1 imp:n=1
18 508 9 -7.3 0 u=1 imp:n=1
19 601 17 -8 0 u=1 imp:n=1
20 701 18 -1 0 u=1 imp:n=1
21 80 19 -2.53 0 u=1 imp:n=1 $Background Cell
22 40 0 -99 fill=1 imp:n=1 $Fill Cell
23 51 0 99 -98 imp:n=1
24 C Univers
25 53 0 98 imp:n=0
26
27 C SURFACE CARDS
28 99 rpp -159 159 -99 99 -99 99 $Sphere surr. entire mesh geometry
29 C Le grand univers
30 98 rpp -160 160 -100 100 -100 100
31
32 C ABAQUS/CAE EMBEDDED MESH SECTION
33 embed1 meshgeo=abaqus &
34 mgeoinc=couche1.inp & $Input file generated by Abaqus/CAE
35 meeout=leadWall.ed3.ee000 & $Name of MCNP6 elemental output file
36 matcell= 1 101 2 201 3 202 4 203 &
37 5 204 6 205 7 301 &
38 8 401 9 402 &
39 10 501 11 502 12 503 &
40 13 504 14 505 15 506 16 507 &
41 17 508 18 601 19 701
42
43 background=30 $MCNP6 background cell
44 filetype=ascii

```

**MCNP Code using Unstructured mesh**

```

44 embee4:p embed=1 $Elemental tally
45 m1 7000 0.784 8000 0.211 18000 0.005 $ Air density -1.293e-3
46 m2 7000 0.784 8000 0.211 18000 0.005 $ Air density -1.293e-3
47 m3 7000 0.784 8000 0.211 18000 0.005 $ Air density -1.293e-3
48 m4 7000 0.784 8000 0.211 18000 0.005 $ Air density -1.293e-3
49 m5 7000 0.784 8000 0.211 18000 0.005 $ Air density -1.293e-3
50 m6 26000 -58 24000 -17 28000 -12 42000 -2 &
51 14000 -1 25000 -2 1000 -0.8 8000 -7 $Acier 316
52 m7 6000 2 1000 3 17000 1 $ PVC -1.38
53 m8 6000 2 1000 3 17000 1 $ PVC -1.38
54 m9 83000 4 32000 3 8000 12 $BGO
55 m10 83000 4 32000 3 8000 12 $BGO
56 m11 83000 4 32000 3 8000 12 $BGO
57 m12 83000 4 32000 3 8000 12 $BGO
58 m13 83000 4 32000 3 8000 12 $BGO
59 m14 83000 4 32000 3 8000 12 $BGO
60 m15 83000 4 32000 3 8000 12 $BGO
61 m16 83000 4 32000 3 8000 12 $BGO
62 m17 26000 -58 24000 -17 28000 -12 42000 -2 &
63 14000 -1 25000 -2 $Acier 316 L
64 m18 1000 2 8000 1 $ H2O
65 m19 13000 0.0199 26000 0.008737 20000 0.0343 12000 0.01032 &
66 25000 0.000067 19000 0.01048 22000 0.0014 15000 0.00018 &
67 14000 0.128945 16000 0.00412 6000 0.01059 1000 0.24465 &
68 8000 0.506316 $ Composition du roche
69
70 mode p
71 C PTRAC FILE=ASC CELL=101 WRITE=ALL MAX=1000000
72 SDEF ERG=D1 POS=volumer
73 S11 L 0.511 1.275
74 SP1 1.8 1
75 f18:p 501 502 503 504 505 506 507 508
76 E18 0 101 1
77 nps 5000000

```

```

1 *Heading
2 ** Job name: Job-9 Model name: Model-1
3 ** Generated by: Abaqus/CAE 6.10-1
4 *Preprint, echo=NO, model=NO, history=NO, contact=NO
5 **
6 ** PARTS
7 **
8 *Part, name="S1_101_source_1.2"
9 *Node
10 1, -93., 0., 0.
11 2, -93., 1.900000, 0.
12 3, -94., 1.900000, 0.
13 4, -94., 0., 0.
14 5, -92., 0., 0.
15 6, -92., 1.900000, 0.
16 7, -91., 0., 0.
17 8, -91., 1.900000, 0.
18 9, -90., 0., 0.
19 10, -90., 1.900000, 0.
20 11, -89., 0., 0.
21 12, -89., 1.900000, 0.
22 13, -88., 0., 0.311736, -95., -1.089795, -1.556389
23 311737, -95., -0.950000, -1.645448
24 311738, -95., -0.764655, -0.817346
25 311739, -95., -1.216943, -1.230216
26 311740, -95., -1.168131, -1.346697
27 .....
28 *Element, type=C3D8R
29 1, 1428, 75852, 32740, 2727, 1426, 75869, 33369, 2725
30 2, 1426, 75869, 33369, 2725, 1428, 75886, 33998, 2688
31 3, 75869, 75870, 33374, 33369, 75886, 75887, 34003, 33998
32 4, 75870, 75871, 33379, 33374, 75887, 75888, 34008, 34003
33 5, 1425, 75886, 33998, 2688, 1409, 75903, 34627, 2686
34 6, 75886, 75887, 34003, 33998, 75903, 75904, 34632, 34627
35 7, 75887, 75888, 34008, 34003, 75904, 75905, 34637, 34632
36 8, 75888, 75889, 34013, 34008, 75905, 75906, 34642, 34637
37 9, 1409, 75903, 34627, 2686, 1392, 75920, 35256, 2650
38 10, 75903, 75904, 34632, 34627, 75920, 75921, 35261, 35256
39 11, 75904, 75905, 34637, 34632, 75921, 75922, 35266, 35261
40 12, 75905, 75906, 34642, 34637, 75922, 75923, 35271, 35266
41 13, 75906, 75907, 34647, 34642, 75923, 75924, 35276, 35271
42 14, 1392, 75920, 35256, 2650, 1391, 75937, 35885, 2648
43 15, 75920, 75921, 35261, 35256, 75937, 75938, 35890, 35885

```

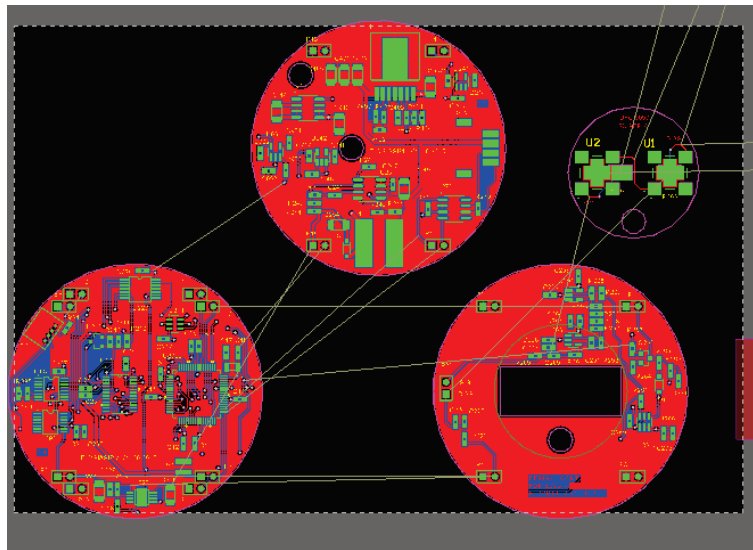
**couche1.inp file: Unstructured mesh description equivalent to Abaqus/CAE file**  
Here, I only extracted an example of INP file structure for one object. It required 529475 lines of codes

```

44 16, 75921, 75922, 35266, 35261, 75938, 75939, 35895, 35890
45 17, 75922, 75923, 35271, 35266, 75939, 75940, 35900, 35895
46 18, 75923, 75924, 35276, 35271, 75940, 75941, 35905, 35900
47 19, 1391, 75937, 35885, 2648, 1390, 75954, 36514, 2611
48 20, 75937, 75938, 35890, 35885, 75954, 75955, 36519, 36514
49 21, 75938, 75939, 35895, 35890, 75955, 75956, 36524, 36519
50 22, 75939, 75940, 35900, 35895, 75956, 75957, 36529, 36524
51 23, 75940, 75941, 35905, 35900, 75957, 75958, 36534, 36529
52 *Elset, elset=S1_101_source_1.2_material_1, generate
53 1, 4568, 1
54 *Elset, elset=S1_101_source_1.2_statistic_1, generate
55 1, 4568, 1
56 *Elset, elset=S1_101_source_1.2_source_1, generate
57 1, 4568, 1
58 *End Part
59 *Part, name="S1_201_air1.1"
60 *Node
61 1, -51.159999847412109, 43.099998474121094, -3.2537450488516313e-17
62 2, -54.659999847412109, 43.099998474121094, -4.364358436514639e-17
63 3, -61.659999847412109, 43.099998474121094, -6.5855845502066389e-17
64 4, -75.660003662109375, 43.099998474121094, -1.1028037439261479e-16
65 5, -110.66000366210938, 43.233402252197266, -0.6993793209594726e-16
66 .....
67 ** ASSEMBLY
68 **
69 *Assembly, name=Assembly
70 *Instance, name="S1_101_source_1.2", part="S1_101_source_1.2"
71 *End Instance
72 **
73 *Instance, name="S1_201_air1.1", part="S1_201_air1.1"
74 *End Instance
75 .....
76 **
77 *End Assembly
78 **
79 ** MATERIALS
80 **
81 *Material, names=BGO_material_001
82 *Density
83 -7.4
84 *Material, names=Air_material_002
85 *Density
86 -1.293e-3

```

### Beta ANDRA sensor electronic circuit design



### Gamma ANDRA sensor electronic circuit design

